Title
Driving Forces and Effects of Ligand Exchange in Nanocrystalline Systems

Permalink
https://escholarship.org/uc/item/3zb6p6j2

Author
O'Brien, Erin Arlene

Publication Date
2018

Peer reviewed|Thesis/dissertation

Driving Forces and Effects of Ligand Exchange in Nanocrystalline Systems

By

Erin Arlene O'Brien

A dissertation filed in partial satisfaction of the

requirements for the degree of

Doctor of Philosophy

in

Chemistry

in the

Graduate Division

of the

University of California, Berkeley

Committee in charge:

Professor A. Paul Alivisatos, Chair
Professor Peidong Yang
Professor James Analytis

Summer 2018

Abstract

Driving Forces and Effects of Ligand Exchange in Nanocrystalline Systems

by

Erin Arlene O'Brien

Doctor of Philosophy in Chemistry

University of California, Berkeley

Professor A. Paul Alivisatos, Chair

Nanocrystals as functional materials rely heavily on their ability to interface with their immediate environment. This is true across the breadth of material applications, from semiconductor quantum dots to plasmonic metal particles and oxides for catalysis. These interfacial interactions can be just as important in defining material properties as the self-contained particle structure. They may control biocompatibility, directed assembly, resistance to degradation and the can even influence electronic energy levels. Nanoscale interfaces are therefore of great interest in the push to make nanomaterials viable solutions for real-world problems. To understand nanoparticle surfaces and interfaces we must begin by characterizing them at the most fundamental level. Molecular species and bulk interfaces both have techniques that have been well-designed to uncover detailed reaction mechanisms and chemical structures, but the same suite of characterization tools has not been applicable to nanoscale materials.

This dissertation will delve into solution-phase and solvent-friendly techniques for characterizing nanocrystal surfaces, the specifics of surface reaction mechanisms and structure in a model system, and the application of surface analysis models to the nanoscale. Chapter 1 will introduce the effects of surface chemistry on nanocrystal functionality with a focus on semiconductor quantum dots. Quantum dot surface passivation and controlled ligand functionality will be discussed in relation to desired nanocrystal properties. We will go into the current state of the literature surrounding post-synthetic modification of nanoscale surfaces and lastly, we will touch upon the ways that ligand exchange reactions can give unique information about the surface of a nanomaterial.

Chapter 2 will address some of the previous work done in nanocrystal surface characterization and look further into the surface sensitivity of nanocrystal proton NMR. The basics of nuclear magnetic resonance will be addressed, as will the mechanisms by which nanocrystal binding affects the observed resonance signal. This binding sensitivity will then be explained in the context of directly tracking a surface modification reaction. Chapter 3 will then follow with an introduction to isothermal titration calorimetry and its adaptation from biochemistry to nanoscale organic-inorganic interfaces. We will build on preliminary studies to describe the utility of ITC for understanding the nanocrystal surface.

Chapter 4 will describe the design and synthesis of a model CdSe nanocrystal system for developing a better understanding of surface interactions and this system will be further explored in chapters 5 and 6 as the basis for two model classes of surface reaction. Both carboxylate-carboxylate and carboxylate-phosphonate ligand exchanges are thermodynamically characterized and we propose a model combined inter-ligand and ligand binding interactions as the underlying cause of the surface dynamics.

Chapter 7 looks deeper into classic analysis methods for surface reactions and their application to quantum dot ligand exchanges. We explore the benefits and limitations of adsorption isotherms and statistical mechanical simulations in corroboration of our surface model. Finally, we derive quantitative estimates of the thermodynamic contributions to ligand exchange driving force in our special case reactions. Chapters 8 and 9 look forward to future surface characterization studies with preliminary results from other surface sensitive measurements and modified nanoparticle systems. In conclusion, we discuss the implications and future directions for this work in the wider field of nanocrystal design and applications.

Dedicated to the family and friends who have supported me in my academic pursuits, and especially to my father who gave me my first introduction to the wonders of science.

Table of Contents

List of Figures

List of Tables

Acknowledgements

Chapter 1: Introduction

Nanoscale systems exhibit many exceptional size-dependent properties; from surface energy[1] to plasmonics[2] to band gap energy[3], the transition from a bulk material to a nanoscale pattern or particle drastically changes the way these materials interact with their environment and incoming stimuli. Over the past decades, a vast repertoire of synthetic techniques have been developed and a wide range of material systems have been characterized in nanocrystalline or nanoparticulate form. Top-down approaches have led to lithographed metamaterials[4–6] while substrate-based[7] and colloidal growth processes[8–11] can give controlled single-crystalline materials. Metal nanoparticles exhibit size and shape dependent plasmonic properties[12], metals and oxides have been studied as high surface area catalysts[13], and semiconductor materials form photoluminescent quantum dots[14]. At this point, nanomaterials have been and continue to be actively developed for use in devices and even medicine[15–19]. Through all of this study, a thorough understanding has been gained of the intrinsic material properties (optical, electronic, structural, and chemical) and some of the ways in which they are affected by their environment. However, systematic studies of the surfaces and interfaces of these materials and the direct implications for their utilization remain incomplete. This dissertation will focus on the ways in which surface chemistry impacts semiconductor quantum dots and how to manipulate surface properties, as quantum dot surfaces have the ability to impact optoelectronic properties, chemical compatibility, and particle assembly[20–25].

1.1 Quantum dot passivation

The surface of quantum dot nanocrystals is a major source of defects and trap states even in the most well controlled colloidal synthesis. Once the materials in question are truly nanoscale in nature, the surface area/volume ratio of the particle will be much larger than in the bulk since surface area scales with r^2 and volume scales with r^3. Additionally, with such small particles many surface atoms will be less fully coordinated to the crystal, leading to an increase in effects from atoms with corner/edge character[26]. Surface effects that are so small as to be insignificant on the bulk scale can completely change the material properties at the nanoscale. Some of the most significant effects seen in quantum dots are surface trap states resulting from under-coordinated surface atoms and dangling bonds[27], leaving pseudo-atomic electronic levels that are not fully pulled into the valence or conduction band (Figure 1.1A). Charge carriers that fall into these trap states may not be able to undergo radiative recombination directly from this energy level leading to long lived trap states. Trapped carriers will have greater opportunity to recombine non-radiatively and decrease the photoluminescence quantum yield of the nanomaterial[28,29]. On the other hand, if the trap state does allow for radiative emission an asymmetry will be seen in the fluorescence spectrum with a red tail, shoulder, or secondary emission peak corresponding to the lower energy fluorescence from the trap state[30]. In this way, the impact of the nanocrystal surface on the optoelectronic properties of quantum dots has hampered efficient utilization of their controlled photoluminescence, and much effort has gone into designing adequate passivation for surface sites on a variety of semiconductor materials[24,31,32].
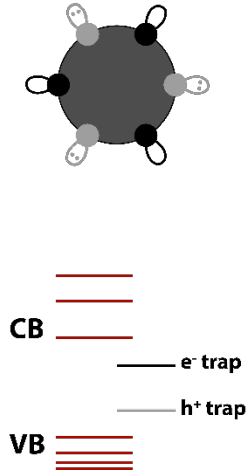
A) Bare Quantum Dot   **B) Core-Shell Passivation**   **C) Ligand Passivation**
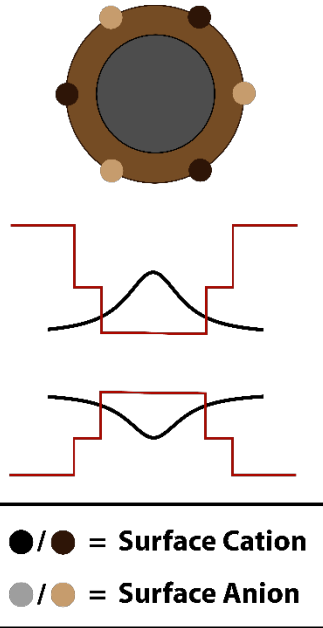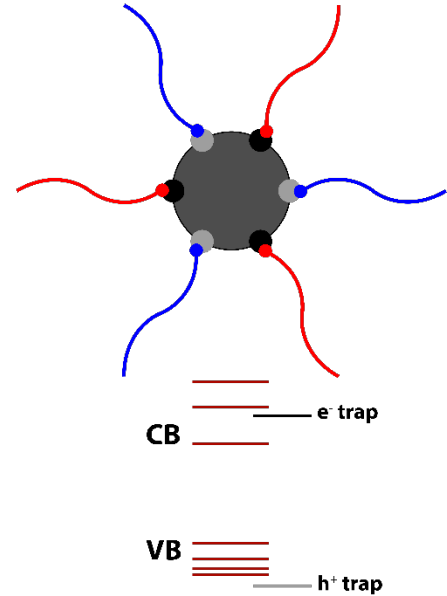
Figure 1.1: Quantum dot surface traps and passivation schemes. A) Electron and hole traps in a quantum dot resulting from surface atoms with incomplete coordination. Orbitals that still maintain some amount of atomic character may lead to empty states within the material band gap. B) Passivation of a quantum dot with a second semiconductor material. For optimal photoluminescence, a type I structure is used as shown to minimize carrier density near the surface where trap states may be detrimental. C) Passivation of a quantum dot with a small molecule ligand shell. Complete ligand binding to surface sites pulls the energy levels of the former trap states out of the band gap.

1.1.1 Core-shell quantum dots

In order to deal with the deleterious effects of incomplete surface passivation in as-synthesized quantum dot systems, core-shell particle syntheses have been developed[29,33]. A second semiconductor material with similar crystal structure and lattice parameters is grown with minimal interfacial defects. Shell quality is controlled synthetically, including the use of layer by layer precursor addition for atomically determined shell thickness[34,35]. One of the most common of these shell passivation designs is the growth of a shell with a wider band gap than the core material and a type I band alignment (Figure 1.1B). Although surface states still exist, much of the charge density is confined to the core particle and traps are less likely to affect the electronic properties. Lattice strain or dislocations at the core-shell interface can lead to additional trap states and Auger recombination, but this is generally minimized by appropriate choice of shell material or formation of a gradient shell[36,37].

While surface traps are best mitigated by type I shell structures, this technique effectively isolates the quantum dot and its excitonic states from the environment[38,39]. At times it is desirable to selectively extract charges from a quantum dot or otherwise manipulate the effective electronic states of the system, which is less favorable if there is no charge density localized at the surface. In these cases, other band alignment structures may allow for localization of electrons and/or holes near the surface (Figure 1.2) but any mitigation of surface trap states will be lost for the charge

carrier in question. In material systems with only shallow or short-lived traps affecting one of the carriers and deeper traps affecting the other, a passivating shell can be designed to confine only the more trap-prone carrier to the core particle and allow for extraction of one carrier type[40]. This scheme is often used for quantum dot photoconduction or photovoltaics, contact with an electrolyte or other carrier source is necessary to prevent particle charging and maintain continuous carrier extraction over time[41,42]. The second carrier remains confined to the core and can only be extracted *via* less efficient carrier tunneling[39]. Thus, although shelling generally accomplishes the most complete passivation of any method, for material flexibility and specific applications a more tunable passivation scheme is desirable.

A) Type I   B) Quasi-Type II   C) Type II
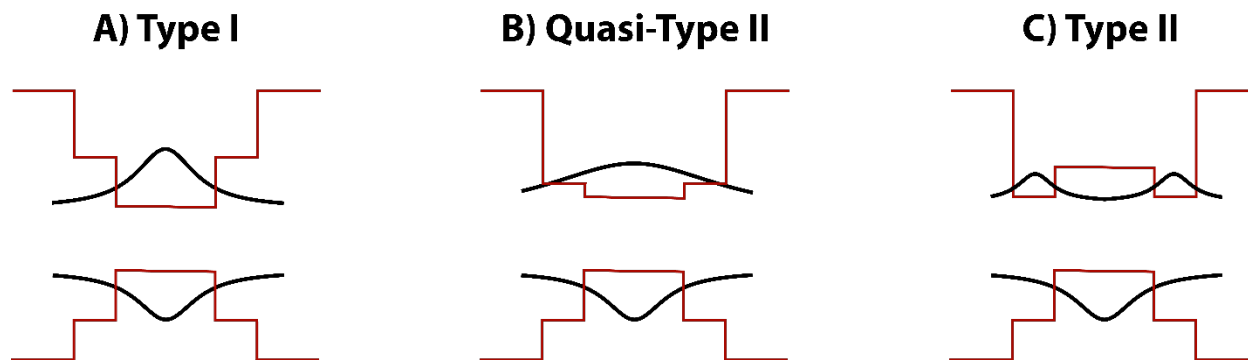
Figure 1.2: Band alignments and carrier localization in core-shell quantum dots. A) Type I band alignment confines both carriers to the core and minimizes the effect of surface traps, B) a quasi-type II alignment confines one carrier to the core but the second carrier maintains some density in the shell due to a very small difference in said band energies, and C) a type II band alignment confines one carrier to the core and the other to the shell material.

1.1.2 Small molecule capping ligands

Molecular passivation is highly tunable by definition; in theory each individual surface site on a nanocrystal could be passivated with a different molecule, and surfactant systems can take many forms. Collectively the molecular surface species bound to a nanocrystal are referred to as the ligand shell. Small ions can be used in pre-formed nanocrystal films or if combined with another ligand to provide the solvent interactions necessary for colloidal stability. Examples of this include chloride capped quantum dots[43–45]. Small differences in molecular sterics and functional groups affect the preferential binding of ligands to different surface sites and the degree to which quasi-atomic energy levels are modulated by the ligand shell[46,47]. Complete surface binding in these cases often requires a mixture of surface ligands to adequately minimize trap states.

Ligands, and especially mixed ligand shells, also increase our ability to tune optoelectronic states. Binding groups such as primary amines passivate surface sites and pull quasi-atomic trap states out of the band gap, resulting in fluorescence enhancement[48]. Meanwhile, thiol ligands quench fluorescence by creating or deepening surface traps[49,50]. Surface species also have profound effects on quantum dot blinking and photobleaching[51]. Ligands with aromatic character or metal centers have been used to facilitate charge extraction and may be bound as a small, controllable percentage of the total surface coverage[39,52–54]. True precision in the formation of mixed ligand shells and optimization of passivation requires an understanding of ligand binding mechanisms and side reactions.

Recent study of quantum dot surfaces has taken a page from the inorganic chemistry of metal ligand complexes. A number of familiar ligand binding motifs have been observed at

semiconductor nanocrystal surfaces, including the characterization of X, L, and Z type binding (Figure 1.3)[55,56]. X-type ligands, which contribute one electron to the bond formed with the surface atom, are common as metal-coordinating ligands in precursors to colloidal synthesis. They are often discussed as ions balancing the surface charge of a non-stoichiometric crystal. Some nanomaterials with stoichiometric surfaces also exhibit a modified form of X-type ligand binding in which both an anion and cation will bind to different surface sites in ion pairs, known as X2-type binding[57,58]. L-type ligands donate both electrons to a dative bond with a charge-balanced surface while Z-type ligands (most commonly MX_2 complexes) bind datively by accepting two electrons from a surface atom. The exact ligand-shell composition of an as-synthesized nanoparticle is heavily dependent on the synthetic method and precursors used. Steric factors and the intrinsic site selectivity of different ligand binding types prevent perfect passivation with a single surfactant and some syntheses use multiple ligands as part of the reaction mixture to improve native optoelectronic properties. Common ligand/precursor molecules across many nanoparticle syntheses include carboxylic acids, phosphonic acids, phosphines, and amines[14,59–62]. We aim to further characterize the overall structure and function of these common ligands in quantum dot colloids.
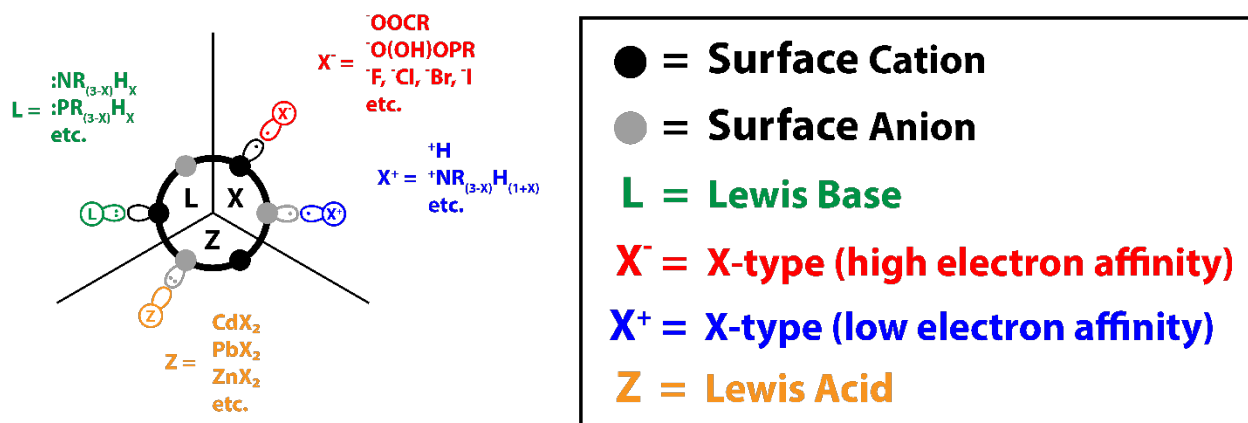
Figure 1.3: Different kinds of ligand binding motif: L-type ligands donate an electron pair to the bond with the surface while Z-type ligands accept an electron pair from a surface anion to form a bond. Both of these ligands bond datively and can passivate a stoichiometric nanocrystal surface. X-type ligands donate one electron to a covalent bond with the surface and depending on the material may exist as ions coordinated to a surface enriched in one of the constituent elements (X) or attach to a stoichiometric surface in pairs (X2).

1.2 Design of functional ligands

Semiconductor quantum dot fluorescence has been proposed as a solution for achieving tunable emission with narrow linewidths in a number of fields from LEDs[63,64] and solar concentrators[15] to bio-imaging[65], and their use as absorbers in solar cells[41,42] and photodetectors[16] has been investigated. Although the effects of nanocrystal ligands on the electronic structure of quantum dots have been well documented, the passivated quantum dots currently in use fall short of their optimized properties *in situ*. This is partly the result of imperfect control of ligand binding, but is exacerbated by incompatibilities between the ligand shell and environmental medium. Ligands are of utmost importance in controlling the functionality of nanoparticles for targeted binding and dispersion in specific material environments. Short ligands with a polar functional group on each end are often used to obtain colloidal stability in polar solvents, including water. Mercapto compounds, phosphines, and amino acids have been used in this capacity, but they also do not fully protect quantum dots from water-based photoluminescence quenching processes[65–67]. Other

surfactants with multiple binding groups may be flexible enough to bind in a bidentate fashion, stabilizing the ligand-particle bond and slowing the process of ligand stripping[68]. Multiple binding groups or a mixture of surfactants in colloidal systems have been shown to displace or even strip desirable ligands from the surface[55]. Ligands with accessible electronic states in a quantum dot band gap have been used for charge extraction and fluorescence quenching, but further mobility of these charges is often limited[39]. Unsaturation and other ligand chain functionalities can facilitate nanoparticle crosslinking to polymers[69]. Simple non-polar surfactants with long alkyl chains in non-polar solvents have been the gold standard for the optimization of quantum dot passivation and surface chemistry to this point, but in order to move forward with property control across a range of experimental conditions we must gain a better understanding of the ways more complex ligands interact with the quantum dot, the environment, and each other.

1.3 Ligand exchange and post-synthetic surface modification

The functionality of native quantum dot ligand shells is necessarily determined by the choice of synthetic precursors. This in turn is limited by precursor reactivity and solubility as syntheses are optimized to produce high quality particles, minimizing polydispersity and defect density. Given the binding and interaction implications for choosing a particular ligand shell, post-synthetic modification of nanoparticles plays a vital role in their potential utility. Ligand addition, ligand stripping, and ligand exchange all provide methods of post-synthetic surface control. In systems lacking native L-type ligands, primary amines can bind to previously un-passivated sites[48]. Pyridine and TMEDA stripping are highly effective for ligand removal[25,55], but most coordinating polar molecules are capable of stripping Z-type ligands from cation-terminated surfaces[70]. By far the most varied method of post-synthetic surface modification is ligand exchange, with many procedures and surfactants used in the literature. Ligand exchange may be done in a biphasic solution[23], in a single-phase colloid with subsequent removal of excess ligand[71], on columns[72], or in quantum dot films[43]. Many of these methods make use of a large excess of the desired ligand to push the exchange to completion, with the caveat that harsh or strongly-binding surfactants may degrade the particle quality[73]. This makes precise control of complex ligand exchanges difficult and severely limits functional nanoscale surface design.
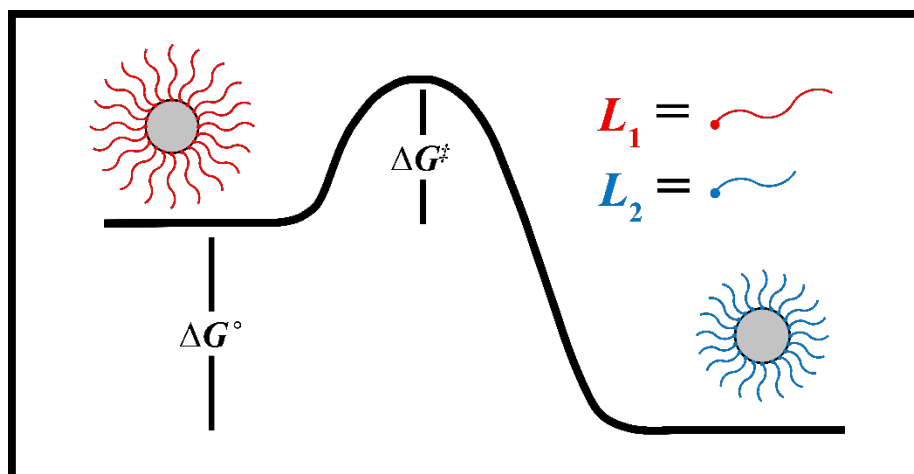
Figure 1.4: Reaction coordinate diagram for a spontaneous ligand exchange reaction from ligand 1 (L_1) to ligand 2 (L_2). Gibb's free energy of reaction ($\Delta G°$) and activation energy ($\Delta G^{\ddagger}$) are shown.

Historically, quantitative measurements of quantum dot surface chemistry have been very difficult to achieve, so surface modification has been characterized in a phenomenological way[46,74]. An improvement is seen in optoelectronic properties or colloidal stability and the procedure is optimized to achieve the greatest benefit. This poses serious problems for the further design of functional nanocrystal surfaces since this kind of optimization doesn't explore causal relationships that are vital for the development of design rules. In the past decade, some efforts have been made to characterize the initial and final states of ligand exchange reactions in ways that directly or indirectly probe preferential binding[45,55,75–81], but true design rules are still lacking and the field remains under-researched. Our study details further characterization of nanocrystal surface modification reactions and the implications of the resulting reaction mechanisms for future ligand shell design and control.

Chapter 2: Nuclear magnetic resonance spectroscopy for surface studies

Nuclear magnetic resonance spectroscopy has been utilized to great effect in characterizing the steady state surface coverage of nanoparticle surfactants[47,82–85]. A wide range of 2D and heteronuclear techniques are available to determine what species are in the colloidal system and the identity of a surfactant bound to a nanocrystal surface[86]. In order to track the progress of a surface reaction *in situ*, a time-efficient and relatively high resolution measurement is needed. Proton NMR is the highest resolution measurement available and enables relatively short acquisition times as a result.

2.1 The NMR experiment

In brief, nuclear magnetic resonance spectroscopy requires the creation of a splitting of spin energy levels for a given nucleus (a two-level system for a proton or other nucleus with spin ½) using a static magnetic field (Figure 2.1A)[87]. The energy of this splitting is determined by the strength of the magnetic field:

$$\Delta E = \gamma \hbar B_0$$

where γ is the gyromagnetic ratio of the nucleus, $\hbar$ is Planck's constant, and B_0 is the magnetic field. The net magnetization of the nuclei is aligned with the magnetic field because the majority of the spins will have ground state energy and align with the field instead of against it. Each individual magnetic moment is not aligned directly with the field at any given time and precesses around the field axis with a frequency determined by the field strength, called the Larmor frequency

$$\omega_0 = \gamma B_0$$

but due to the random distribution of magnetic moment components in the transverse plane the overall magnetization is aligned. While a given nucleus has an empirically-determined gyromagnetic ratio, the immediate chemical environment, including distribution of electron density and neighboring nuclear spins, will slightly increase or decrease the effective magnetic field at a given nucleus and results in a narrow band of Larmor frequencies for different nuclei in a molecule. It is this phenomenon which enables molecular structure determination *via* the determination of a nucleus' chemical shift relative to a standard[88].

$$\delta = \sigma_{ref} - \sigma_i$$

where σ_{ref} and σ_i are the shielding constants of the standard and of nucleus i, respectively. Shielding constants are in units of Hz/MHz (ppm). In order to measure the spectrum of a sample in a Fourier pulse spectrometer, the system is excited using a radiofrequency pulse perpendicular to the static magnetic field B0, inducing a strong secondary magnetic field B1 and causing the net magnetic moment of the ensemble of nuclei to tip off axis from B0. This involves both the absorption of the RF energy to excite a ground or low energy state spin to a higher energy level and the temporary precession of the spins around the pulse axis (Figure 2.1B). The pulse is an approximated square wave tuned to the Larmor frequency of the nucleus of interest given the static magnetic field. In reality, this pulse contains a range of frequencies the sum of which produces the square wave, enabling the simultaneous excitation of any nuclei with a chemical shift within the frequency band[89]. The extent of resonant absorption observed is directly proportional to the number of nuclei with the given resonant frequency in the measurement volume. With the addition of an internal standard in the system, molecular concentrations may be measured quantitatively.
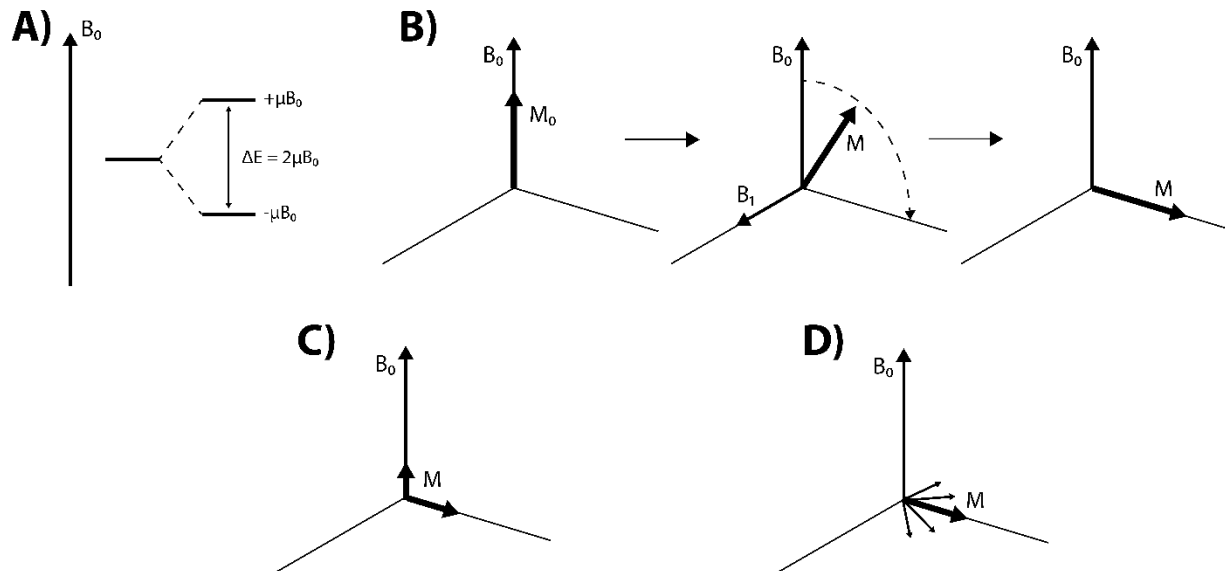
Figure 2.1: Excitation and relaxation of nuclear magnetic resonance. A) Zeeman splitting of a spin ½ nucleus by static magnetic field B₀, B) excitation of nuclei with a radio-frequency pulse B₁ at the Larmor frequency, perpendicular to B₀, C) the effects of longitudinal relaxation mechanisms on the net magnetic moment of the sample nuclei, note that a decrease in transverse magnetic moment also results, and D) decoherence of magnetic moments by fluctuating magnetic fields as a mechanism of transverse relaxation.

2.2 Nanocrystal surface reaction tracking

Proton NMR is particularly useful in the characterization of nanocrystal-bound ligand, even in the presence of free-floating ligand of the same molecular structure, because ligand binding to nanocrystals induces a shift and broadening of the signal linewidth in the NMR spectrum. The change in the chemical shift of the signal is easily explained by the change in the nucleus' neighboring chemical environment as a result of surface attachment, while the linewidth broadening is due to a decrease in the nuclear relaxation time of the nuclei in a bound molecule[84].

NMR linewidths are limited by the relaxation time of the excitation as formalized by the Heisenberg uncertainty principle[90].

$$\Delta v = {1}/{\pi T_{relax}}$$

In this case, Δv is the full-width half-maximum of the resonant signal in units of frequency. There are two different kinds of nuclear relaxation at work in these systems, longitudinal and transverse relaxation. Longitudinal relaxation refers to the recovery of the net magnetization component along the axis of the magnetic field B0 and is characterized by relaxation time T1 (Figure 2.1C). Dipole-dipole interactions, spin rotation, and chemical shift anisotropy all contribute to this process. Some contributing factors to longitudinal relaxation are most effective when the frequency of molecular motion approaches the Larmor frequency and enables more efficient energy transfer, so T1 has a minimum when the molecular tumbling rate matches the nuclear resonance. As a result, the longitudinal relaxation rate initially increases with increasing molecular size but decreases again in the solid state[91]. Transverse relaxation is the process of loss of the magnetization component in the xy-plane with a relaxation time T2. Because longitudinal relaxation is directly coupled to a decrease in transverse magnetization, the T2 time for a given nucleus will be less than or equal to T1 for standard systems, with a theoretical limit of T2 = 2*T1[92]. Usually the observed T2 is shorter than T1 as additional processes can contribute to transverse relaxation that do not directly affect longitudinal relaxation. Spatial variations in the magnetic field strength mean that nuclei with a certain chemical shift will still experience slightly different fields and precess at different frequencies, causing decoherence of the magnetic moments in the xy-plane (Figure 2.1D). This process is enhanced when large molecules or particles tumble slowly in solution and the effective magnetic field felt by the nuclei undergoes less spatial averaging. This means that the determining relaxation time for nanocrystal NMR linewidths is T2 (Figure 2.2). We can take advantage of this phenomenon to distinguish bound and free ligand *in situ* during ligand exchange reactions without disrupting the equilibrium with nanocrystal isolation processes[93].

A) Solution　　　　**B) Colloid**　　　　**C) Solid**

Increase Correlation Time

Increase T_2

Increase T_1　　　　　　Increase T_1

$T_{corr} = 0.62/\omega_H$
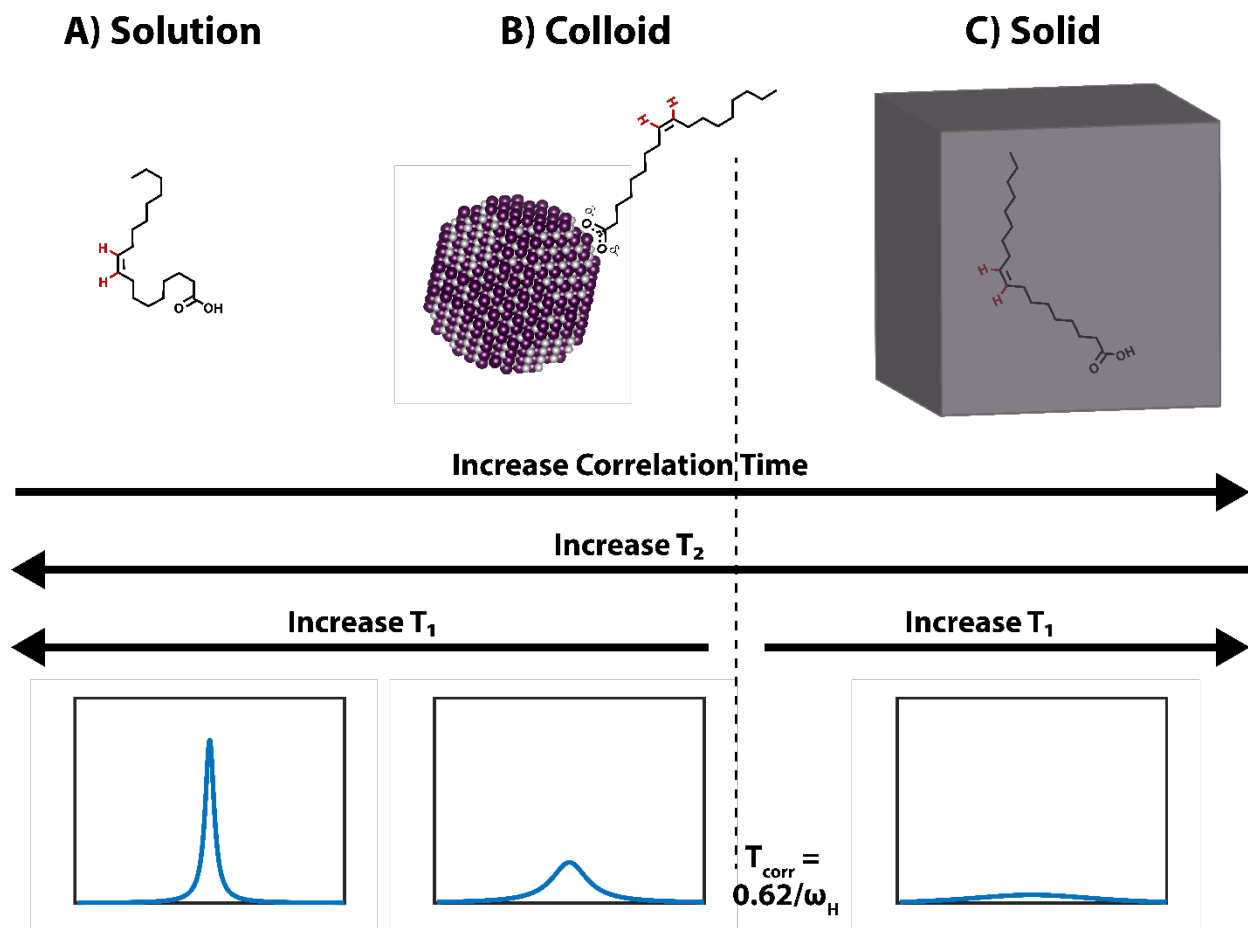
Figure 2.2: Nanocrystal ligand binding and the effects of molecular mobility on NMR linewidths. A) A free surfactant molecule in solution tumbles and reorients quickly on the NMR time-scale (short correlation time), averaging out inhomogeneities in the magnetic field and moving too quickly for efficient resonant energy transfer from nuclear spin to rotational motion. Thus both T_1 and T_2 relaxation are slow and the characteristic narrow signal linewidth is observed. B) A nanocrystal-bound surfactant in a colloid has slowed molecular reorientation, improving rotational energy transfer and decreasing magnetic averaging. Relaxation times shorten and NMR signal broadens. C) The surfactant molecule in the solid state will undergo minimal motion in situ. Rotational energy transfer is once again inefficient but field inhomogeneities lead to very quick T_2 relaxation and a very broad signal is observed.

Surfactant molecules containing long alkyl chains have many nuclei with similar chemical shift, so the NMR signal from the bound ligand in the alkyl region is often difficult to characterize. Even with multiple peak fitting, the overlap of peaks from different bound and free ligand protons is often indistinguishable. Ligands with aromatic moieties, unsaturation, or halide functionalization provide sufficiently distinct chemical shifts for bound and free proton signals to be fit with a Gaussian/Lorentzian distribution and integrated (Figure 2.3). It is important to note that bound and free populations can only be distinguished when the frequency of exchange, or ligand on-off rate in our case, is lower than the Larmor frequency difference between the two states[94]. When the molecular exchange is fast compared to this NMR time scale the chemical shift and linewidth will show only a single averaged signal. This effect can be highly detrimental to quantitative binding characterization, but is not observed in many cases of nanocrystal ligand exchange. The risk of characterization-bias can be minimized by working with a system that has relatively covalent

ligand-nanocrystal bonding and only small exchange-induced differences in the chemical environment at the nuclei of interest.

NMR solvent choice changes the chemical and solvation environment of all protons in the system and the chemical shifts and observed linewidths vary accordingly. At high resolution it is also possible to see slight shift differences between mostly equivalent protons in free ligands. This, and the existence of free/bound overlap, necessitates careful peak fitting.
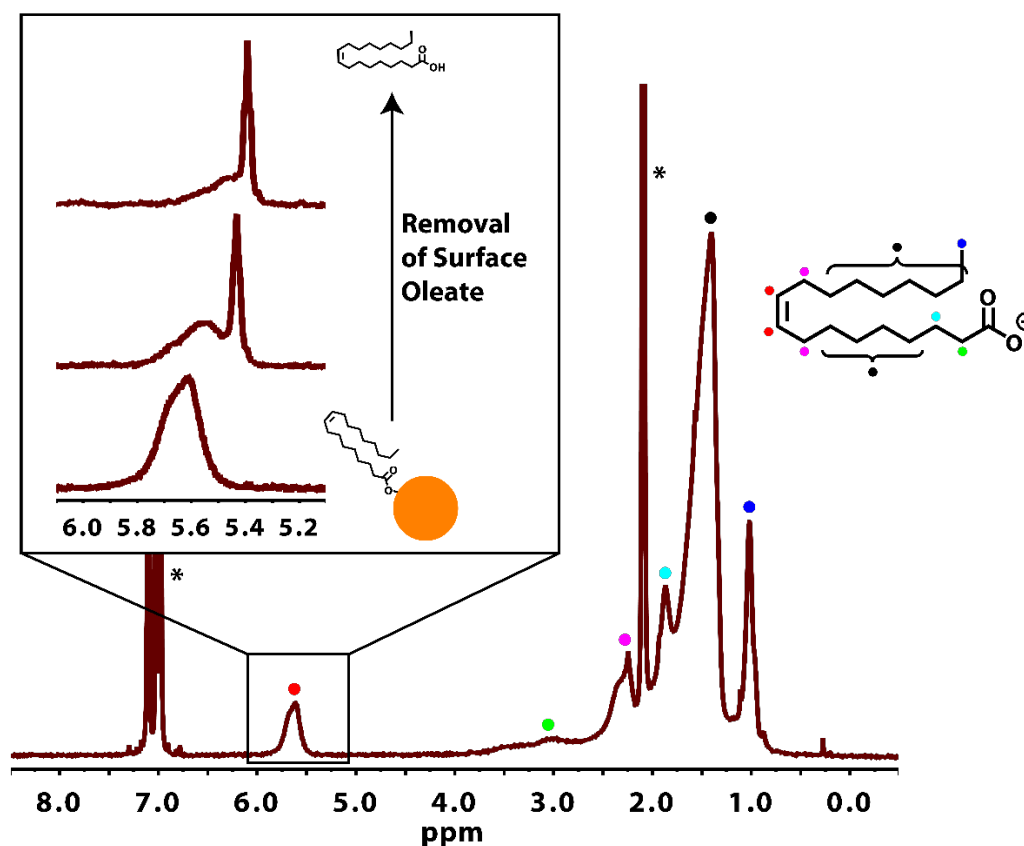
Figure 2.3: Nanocrystal-bound oleate ligand. Vinyl protons are easily tracked and the bound and free signals may be deconvoluted during ligand displacement. The bound protons are broadened and shifted downfield from the free ones. Between 0.8 and 2.5 ppm the majority of the alkyl protons have overlapping bound and free signals, making it more complicated for analysis.

Chapter 3: Isothermal titration calorimetry as a technique for characterizing surface reactions

Isothermal titration calorimetry is a powerful technique for determining the thermodynamic properties of chemical reactions under isothermal and isobaric conditions[95]. It is a particularly popular method in the characterization of molecular binding to biological macromolecules[96–98], but its applications can be significantly more widespread. ITC can be adapted to any of a number of reaction types in which the reaction conditions involve moderate temperatures and mono-phasic solubility of precursors and products, and it has been used to investigate both the thermodynamics and kinetics of reactions[99–101]. With the increased study of nanocrystal formation and

functionalization in recent years, ITC has been tested as a method to gain phenomenological understanding of these transformations. Catechol binding on ZnO nanocrystals was studied using ITC by Lin et. al., and a number of ligand exchange reactions have been tested to determine the sign of the enthalpy of reaction[102–105]. Studies thus far have not shown the strong quantitative or mechanistic insights in nanocrystal systems that have come to be expected in biological ITC. In this work, we show that isothermal titration calorimetry can be used in a controlled and quantitative fashion to improve the current understanding of surface reaction mechanisms.

3.1 The ITC experiment

Isothermal titration calorimetry is a solution-phase technique, making it ideal for the kind of ligand exchange reactions of interest in colloidal nanocrystal modification. A solution of known native quantum dot concentration is titrated with a solution of known ligand concentration and the raw data is collected as a heat rate of reaction (Figure 3.1B). The technique relies on a thermally-controlled cell block to maintain isothermal conditions. The cell block contains both sample and reference cell which are maintained at a set temperature using the Peltier effect (Figure 3.1A). The sample cell can be maintained at a slightly lower temperature than the reference cell, the difference being made up by a separately controlled resistive heating unit on a temperature-sensing feedback loop. When a reaction takes place in the sample cell, the power supplied to the resistive heating unit is increased or decreased for an endothermic or exothermic reaction, respectively. In this way, reactions can be probed at a range of temperatures with an internally consistent reference. Calibration of the isothermal titration calorimeter is necessary to get accurate quantitative data and standard reactions can be used to confirm active cell volume, while injection volume can be checked by mass[106].

Information about the reaction progression and equilibrium constant of a reaction can be determined directly from a well-designed ITC experiment. Reaction titrations may be performed step-wise or by monitoring a continuous injection. Step-wise injections often increase experimental time due to the necessity of allowing equilibration of all reagents before the subsequent injection, but this kind of experiment is in many instances easier to interpret. After equilibration at the set temperature and an initial baseline collection, a small titrant injection (on the order of microliters) is added to the analyte in the sample cell. Maintaining a minimum injection volume with an appropriately-scaled titrant concentration minimizes the effects of dilution on the chemical equilibrium. An injection delay time is set to allow for reaction equilibration and a return to baseline before a new injection is added. Raw signal is measured in μJ/sec of power supplied to maintain the set temperature of the sample cell, which is then integrated peak by peak to determine the enthalpy of the injection in question (Figure 3.1C).
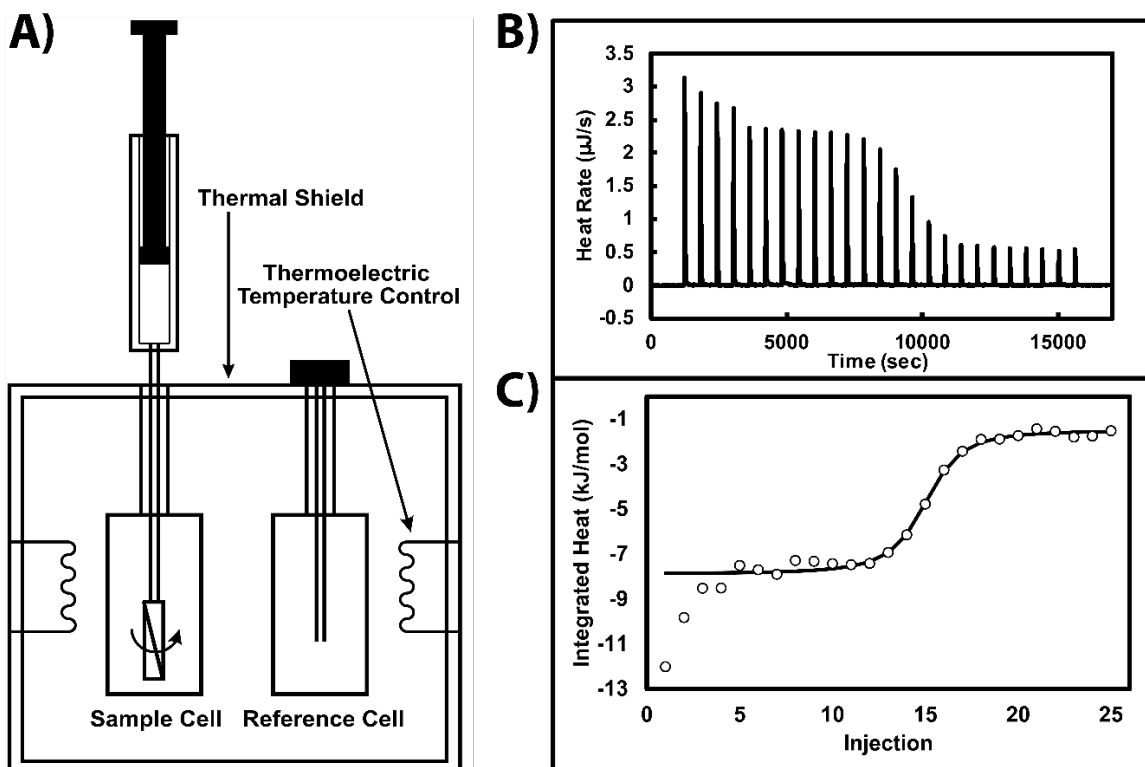
Figure 3.1: Isothermal titration calorimetry. A) Schematic of the ITC apparatus, B) raw data of isothermal heat rate from a stepwise titration, and C) integrated enthalpy per injection fit to an independent reaction isotherm

Interpretation of ITC results requires adjusting reaction isotherms for solution-phase titrations[107]. For a given model, a nonlinear least squares optimization may be performed, adjusting for the slight volume increase with each titrant injection. Given known concentrations and volumes as inputs, the unknown thermodynamic parameters may be determined. These include the number of binding sites per molecule or particle, the equilibrium constant of reaction, and the molar enthalpy of reaction. Standard binding isotherms (non-interacting, cooperative, etc.) often must be modified to account for the additional complexities of an exchange reaction on an imperfect substrate with many binding sites. Careful experimental design and analysis of the system parameters and potential variables is imperative for an accurate fit, since the equilibrium information obtained is only as good as the model used to determine it.

3.2 How ITC can shed light on ligand binding

The benefits of isothermal titration calorimetry as an analytical thermodynamic technique are multi-fold. Unlike many other methods for tracking the progression of a reaction and understanding its equilibria, ITC gives a direct enthalpy measurement with high resolution. This improves the ability to determine the factors affecting the equilibrium by enabling fitting to both enthalpy and equilibrium constant. This in turn shows the entropic contributions to the equilibrium. Other techniques, such as quantitative NMR, while useful lead to larger uncertainties as compared to the potential variation in the model fit from significant parameter fluctuations. Additionally, the small sample size necessary (1 mL or less) and ability to tune titrant and analyte concentrations

independently over multiple orders of magnitude enables concentration-dependent study and the optimization of parameters.

Chapter 4: Control of nanocrystal syntheses and reactions

Although ligand exchange is now a common procedure for the post-synthetic modification of nanocrystals, well-defined surface chemistry is needed to perform a careful study of these reaction mechanisms. Surface reactions may be influenced by any and all native surface species, and surface inhomogeneity plays a significant role. In nanocrystal colloids, this means that high quality, monodisperse particles with a single-surfactant, well-characterized native ligand shell are required for reproducible ligand exchange. Additionally, at least one of the ligands involved must have an easily distinguishable NMR peak for reaction tracking. To this end, we chose to study a nanocrystal system that has been well-characterized and has a significant history in the literature: cadmium selenide quantum dots.

4.1 Quantum dot design and synthesis

CdSe quantum dots were synthesized by adaptation of a previous literature synthesis[108]. A cadmium oleate precursor was used with no additional stabilizing ligands to obtain a final product with a single-component oleate ligand shell. A high precursor loading enabled synthesis of large batches of quantum dots. Most Cd-oleate based CdSe syntheses use an amine or other secondary ligand to aid particle stabilization and passivation during growth and improve the optical properties, and pure oleate syntheses were found to produce greater polydispersity. To minimize the possible effects of varying surface curvature on the thermodynamics of nanocrystal surface reactions, size-selective precipitation was performed and the disappearance of a blue tail in the emission spectrum confirmed the effect. The final sample was characterized by TEM, XRD, and optical spectrometry (Figure 4.1).

Designing the synthesis to ensure a pure oleate ligand shell served multiple purposes. An excess of ligand must be used for precursor complexation and ligand binding, and the liquid room-temperature phase of oleic acid makes it ideal for post-synthetic cleaning and processing. Additionally, the cis-unsaturation in the alkyl chain not only provides an NMR handle for characterization, but gives the surfactant a distinctive steric and functional constraint to compare with other ligands. Carboxylic acids are X-type ligands for which the binding properties have been thoroughly studied and which is known to be stable on the surface but easily displaced by other surfactants in a number of experimental conditions. Lastly, preventing a mixed ligand shell ensures that any thermodynamic contributions to a ligand exchange equilibrium will be well defined in a binary ligand system.
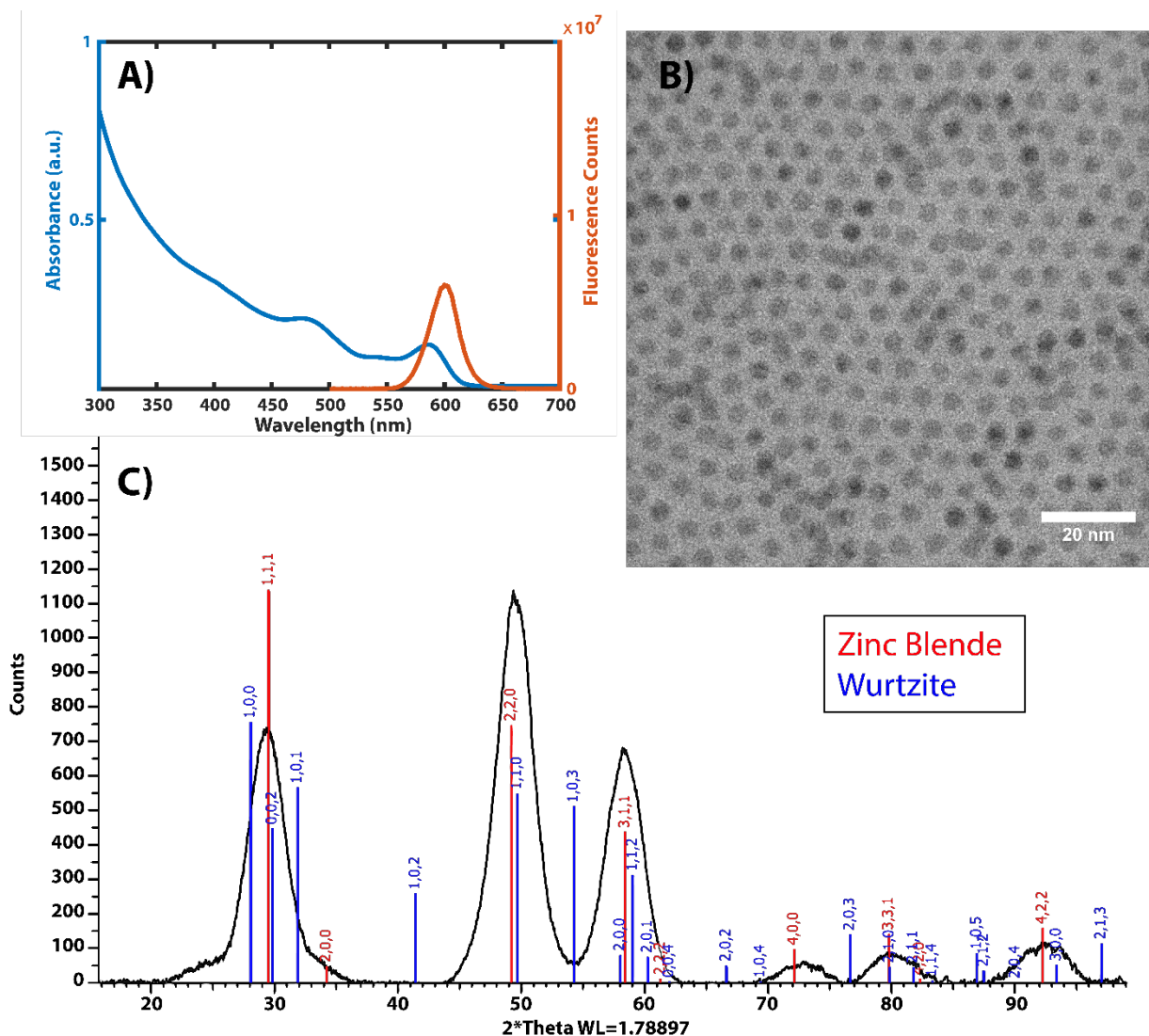
Figure 4.1: Characterization of optimized CdSe quantum dots. A) Absorbance and fluorescence spectra of CdSe quantum dots, B) TEM of quantum dot sample, and C) quantum dot XRD showing the zinc blende crystal structure of the particles

4.2 Ligand exchange optimization

Nanocrystal surface modification can take many forms, but ligand choice and reaction design are key for controlled ligand exchange studies. Standard surfactant ligands have two main components as they relate to the particle surface: the binding group (also known as the head group) and any additional alkyl chains or functional groups that interact with the nanocrystal environment (called the ligand tail) (Figure 4.2). During ligand design, head groups are generally optimized for stronger vs. weaker coordination and orbital overlap for dangling bond passivation or fluorescence quenching[48,49]. Tail groups on the other hand play a significant role in determining targeted attachment of small molecules or biomolecules to the nanocrystal[109], or in turn nanocrystal attachment to other nanomaterials and substrates[110–112]. Ligand tails also modulate particle solubility and electronic accessibility in varying environments including particle monolayers at interfaces, polymer films, and colloidal solutions[113–115].

14
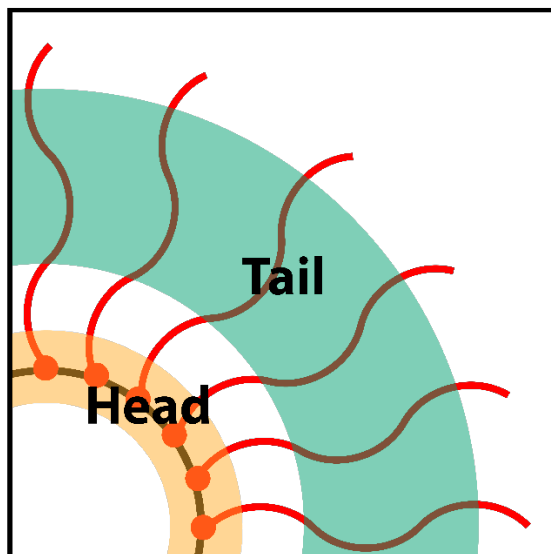
Figure 4.2: Illustration of the two design components of a small molecule ligand shell, the head groups that bind to and passivate surface sites and the tail groups that interact with the quantum dot environment

A number of common binding groups are prevalent in quantum dot synthesis and make interesting targets for study. In this research, we investigated X-type ligand exchange as one of the mechanistically simplest surface modification reactions. In these exchanges, the total number of passivated surface sites remains constant and is determined by charge balance, and we use organic acid ligands that are expected to exchange *via* simple proton exchange (Figure 4.3). Phosphonic acid ligands are common in the synthesis of wurtzite phase CdSe quantum dots and have been shown to displace carboxylic acids in a nearly irreversible stoichiometric fashion[93,116]. Exchanges with both carboxylic and phosphonic acid binding groups can shed light on the ways in which head groups affect surface structure and dynamics.

There has been significant variety in ligand tails for functional nanomaterials, with a wide range in steric bulk and functional groups, and there has been relatively little work done to understand how these functionalizing components affect reaction mechanisms. Given the vast scope of the ligand pool and the potential thermodynamic complications posed by surfactants with many functional groups or complex structure, we chose to probe the effects of a simple alkyl chain length dependence of the tail group on the exchange reaction. By comparing and contrasting the effects of head and tail group dynamics during ligand exchange reactions, we are able to show the interplay of these two factors in nanocrystal surface structure determination.
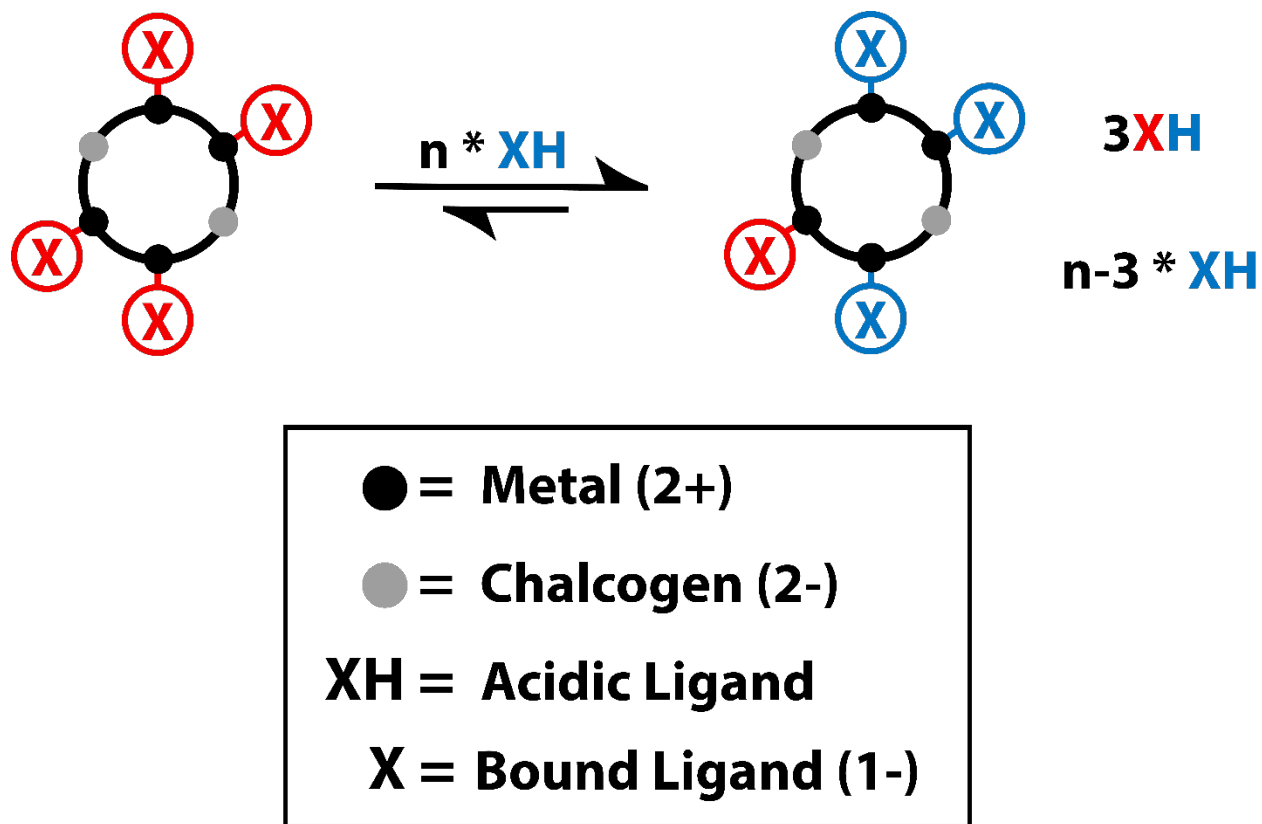
Figure 4.3: An X-type ligand exchange via proton transfer. Anionic ligands serve as charge balance for semiconductor nanocrystals with a metal-terminated, cation-rich surface.

4.3 Hard Soft Acid Base (HSAB) theory and head group effects

Hard Soft Acid Base theory was developed as an aid to understanding the role of molecular, atomic, and ionic polarizability in the determination of chemical equilibria[117]. An absolute hardness value[118] may be assigned based on the ionization potential I and electron affinity A of the entity in question

$$\eta = \frac{I - A}{2}$$

but the theory is most often applied qualitatively. An ion (acid or base) is considered hard if it has a tightly-held electron shell with little polarizability. Soft ions tend to have more polarizable electron density and for single atomic ions, will often be larger. Application of the theory is relative; any given base will have better effective orbital overlap and stronger bonding with an acid of similar hardness or softness. In the case of organic acids, the observed pK_a of the acid may be affected by HSAB theory, as pK_a is a measure of the dissociative equilibrium of the acid and that equilibrium will be affected by relative polarizabilities. Protons are extremely hard acids and in both dissociation and exchange will tend to preferential bonding with hard bases. The theory is also a useful tool for understanding the proposed higher binding strength of phosphonate ligands to cadmium than carboxylate ligands to the same. A relatively soft acid such as a cadmium ion will form a more favorable bond with a base that allows for better electron delocalization such as phosphonate, as compared to the harder carboxylate base. A proton is harder than a cadmium ion,

and a phosphonate ion is softer than a carboxylate ion, so the favorable endpoint is to pair Cd-phosphonate and H-carboxylate. These factors affecting binding affinity inform our expectation of a strongly driven reaction for a carboxylate-phosphonate head group exchange.

Chapter 5: Thermodynamics of carboxylate-carboxylate ligand exchange

Using native oleate-capped CdSe quantum dots as a starting point, we first performed ligand exchange reactions with alkyl carboxylic acids, keeping the head group constant (Figure 5.1). The mono-unsaturated native ligand was replaced with ligands with un-branched, saturated alkyl chains as a tail group. This alkyl chain length was varied over a range from 9 methyl units to 17 methyl units as a further probe of ligand tail effects on the reaction. Chain length was chosen as a simple point of control to gain insight into tail group packing interactions and the possibility of surface entropy as a contribution to reaction driving force. Equivalent reactions were performed for calorimetry and surface coverage measurements under conditions detailed in appendix A-4.
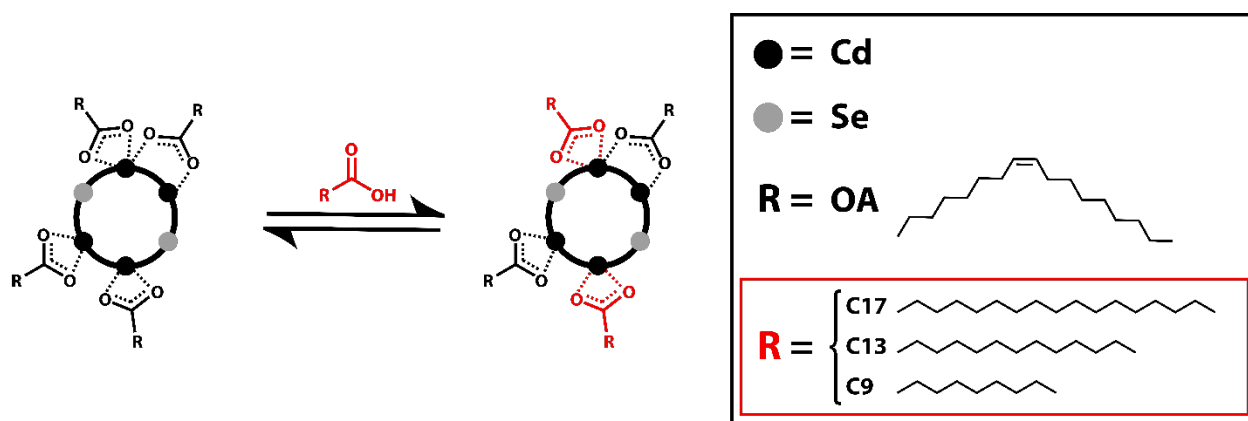
Figure 5.1: Ligand exchange with a maintained carboxylate binding group. Interaction effects are investigated using ligands with tails of different alkyl chain lengths, including decanoic, myristic, and stearic acids.

5.1 Surface coverage

We characterized nanocrystal ligand surface coverage using proton NMR of ligand exchange solutions after each ligand addition (Figure 5.2). Surface coverage of the native oleate ligands was determined by fitting the bound vinyl peak at 5.4 ppm and the free peak at 5.37 ppm, both of which values can be used to determine the ratio of native ligand remaining to total initial ligand bound. Assuming a one to one exchange reaction, exchanged surface coverage is plotted as a function of the mole ratio of ligand added to total binding sites (Figure 5.2C). Upon exchange with all carboxylic acid ligands, a gradual decrease in the native ligand surface coverage is observed. The reaction profile indicates an exchange driven mainly by mass action, and there is no significant difference observed in the reaction progress of exchange with C9 ligands or C17 ligands. Of note is the fact that the surface coverage measurement indicates a sub-unity equilibrium constant, as the average extent of exchange at stoichiometric ligand addition (mole ratio = 1) was only 40% and it required an approximate 1.4x excess of added ligand to achieve 50% oleate displacement. Direct calculations of the equilibrium constant showed a good deal of uncertainty, but average values were similar for long and short chain ligands. This deviation from a mass action displacement was surprising, as the pK$_a$s of these fatty acids, including the native oleic acid, should not have been

significantly different. There is some evidence that long chain fatty acids in micelles or interfacial monolayers display variable pK$_a$ due to collective stabilization[119], but we tuned our reaction to low ligand concentration in a good solvent to avoid these effects. The polarizability and overall charge stabilization of the carboxylate ion likewise remains the same throughout the exchange. Given these constraints on the head group exchange, inter-tail group interaction effects are likely determining factors in the non-spontaneity of the reaction.
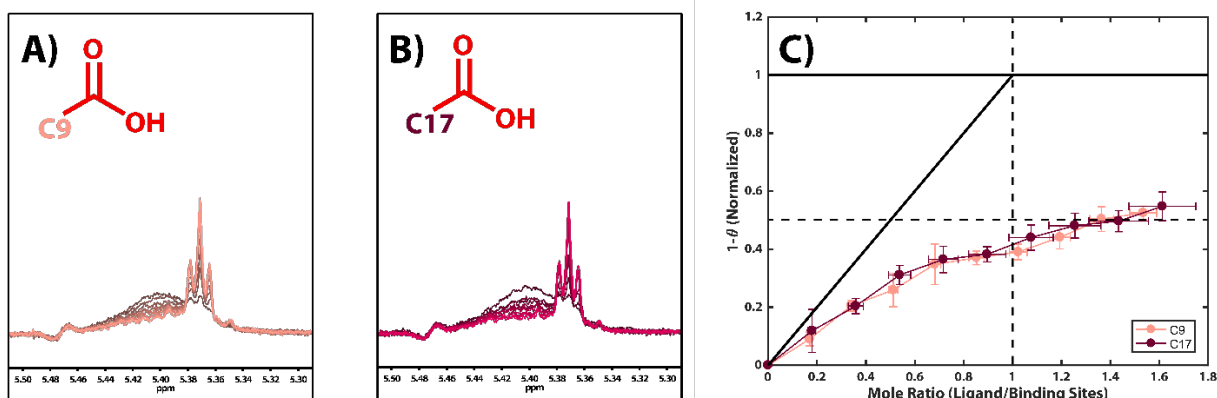
Figure 5.2: Quantitative NMR of carboxylic acid exchanges. A) Vinyl proton tracking of oleate displacement during exchange with decanoic acid, B) Vinyl proton tracking of oleate displacement during exchange with stearic acid, C) Normalized extent of ligand exchange as a function of the mole ratio of added surfactant to surface binding sites. Θ represents surface coverage of oleate ligand. At mole ratio 1, exchanged surface area is less than 50%.

5.2 Enthalpy of reaction

Calorimetry measurements provided a much more complete picture of the ligand exchange profile than can be surmised from surface coverage alone. Raw data plotted against titration time shows a sharp decrease in the power used to maintain the sample cell temperature with each injection, clearly demonstrating an exothermic ligand exchange reaction (Figure 5.3A). The integrated signal per injection for all carboxylic acid exchanges is presented in kJ per mole of new ligand added as a function of ligand/site mole ratio. All exchanges were slightly exothermic (Figure 5.3B), once again calling into question any assumption that the sub-unity equilibrium constant of the reaction is due to binding energy differences. There is also a notable enthalpy dependence on ligand tail length, with longer chain ligands contributing to a more exothermic exchange reaction than short chain ligands. This exothermic signal falls off quickly for all tail groups, well before surface coverage measurements indicate that the reaction would go to completion. Overall, in conjunction with the sub-unity equilibrium constant, these observations imply a decrease in the entropy of the system which is most prominent during the first portion of the reaction.
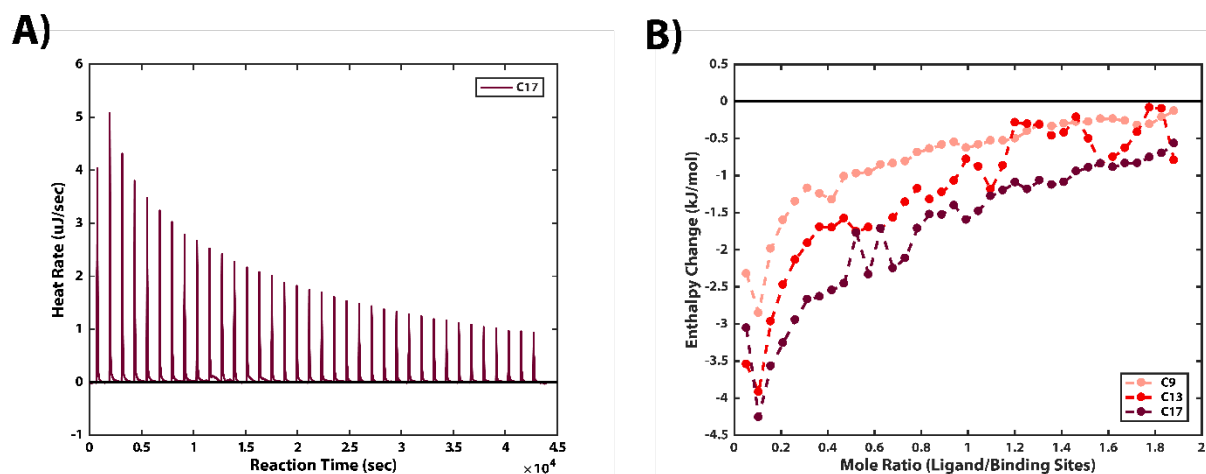
Figure 5.3: Isothermal titration calorimetry of carboxylic acid ligand exchanges. A) Raw heat rate signal measured during a representative ligand exchange with stearic acid, and B) enthalpy per mole ligand added, integrated for each ligand injection as a function of ligand mole ratio. Titrations with 3 different ligand tail groups show a mild dependence of reaction enthalpy on the alkyl chain length.
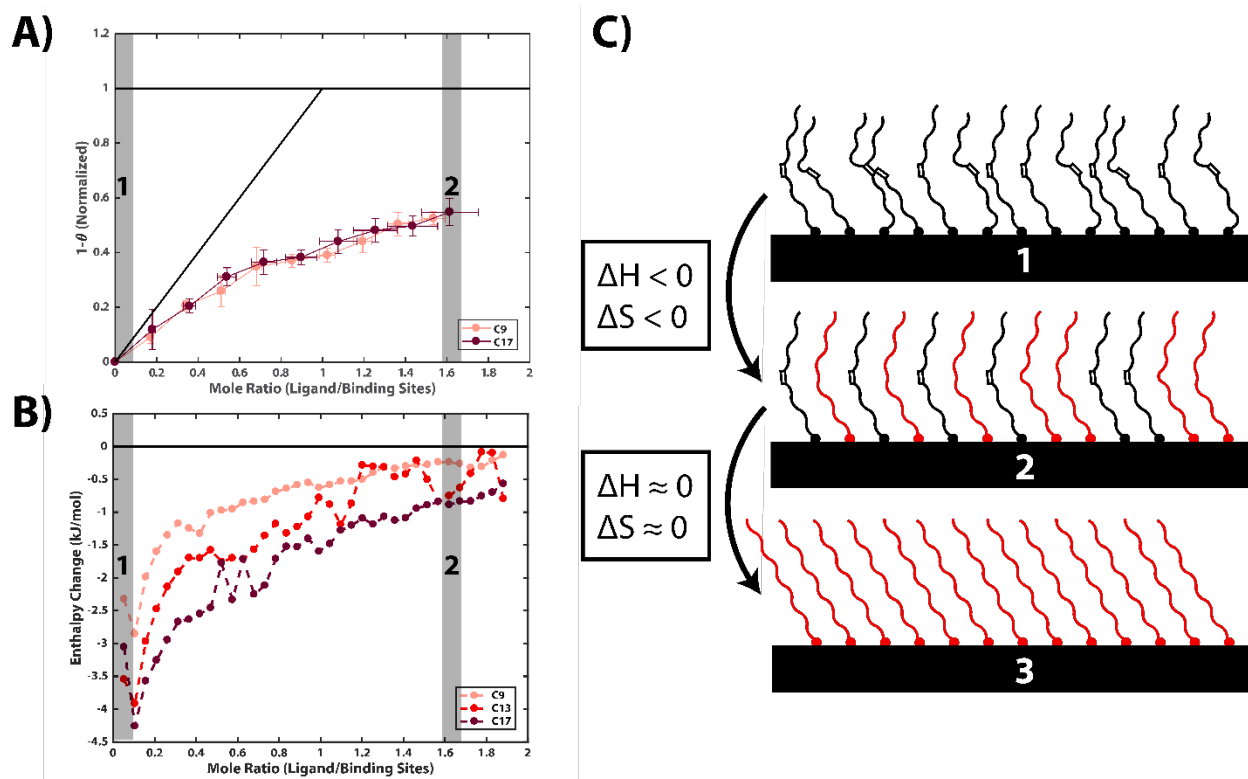
Figure 5.4: Contributing interactions in carboxylic acid exchanges. A) Ligand exchange surface coverage with carboxylic acids, marking surface snapshots 1 & 2, B) ligand exchange enthalpy per injection with carboxylic acids, marking surface snapshots 1 & 2, C) cartoon snapshots of native ligand shell (1), packing of saturated ligands in a mixed shell (2), and a fully saturated ligand shell (3).

19

5.3 Proposed mechanisms

In order to understand the rich phenomena occurring in what might at first be considered rather simple nanocrystal surface reactions, we considered the many possible contributions to the thermodynamic driving force. In this case we do not expect differences in head group binding enthalpy to account for the observations made during reaction characterization. Solution and surface entropy must therefore contribute significantly to the end state of the surface, and inter-ligand interactions, which are commonly not considered, may in fact be deterministic. A model that is consistent with our experimental results must include contributions from enthalpy and entropy changes of the ligand tail.

In carboxylic acid ligand exchanges, there will be minimal entropic contribution from the head group exchange either at the surface or in solution, as the number of free and bound species remains constant and the head group binding geometry at the surface should be equivalent. Both ligands have a small steric profile that is unlikely to significantly affect head group binding. However, as oleic acid has a lower freezing point and is therefore more disordered in its pure form than the saturated fatty acids in question, it is likely to also order less on the nanocrystal surface (Figure 5.4C-1). This is due to the cis-unsaturated bond between carbon atoms 9 and 10, which decreases the configurational degrees of freedom for the molecule and introduces the potential for unfavorable monolayer packing conditions. In the self-assembled monolayer (SAM) literature, it is common to characterize similar monolayers using metrics that relate to the surfactant ordering. A higher degree of ordering is generally correlated with a higher degree of Van der Waals or other inter-ligand interactions as defined by the molecular structure of the surfactants[120]. An increase in the degree of Van der Waals interactions is in this case consistent with a decrease in both the total enthalpy and entropy of the system. The enthalpy change from this transformation is determined by the energetic favorability of the final saturated chain conformations. Saturated alkyl chains are better able to maximize Van der Waals interactions by accommodating bond rotation than unsaturated ligands. Under experimental conditions, an exchange from an oleate ligand to a saturated chain carboxylic acid will increase the packing ability of the ligand shell and lead to an increase in effective Van der Waals interactions while decreasing the surface entropy (Figure 5.4C-2). We expect a decrease in the formation of new Van der Waals interactions with exchange as the surface and remaining oleate ligands become more ordered, which fits well with the gradually decreasing enthalpy of reaction. Longer alkyl chains in these exchanges have greater capacity to form Van der Waals interactions, consistent with a larger enthalpic signal from initial ligand injections, but the enthalpy difference between long and short chain ligand exchanges is smaller than we might expect given the average energy of Van der Waals interactions. To explain this observation we consider the particle morphology. Studies of SAMs on nano- and micro-particles of varying diameter have shown that increasing surface curvature leads to decreasing order in the monolayer[121,122]. Due to the high curvature of our nanocrystal surface, the maximum Van der Waals enthalpy will be significantly lower than that for a fully ordered monolayer, and this effect will increase for longer alkyl chains that extend further from the surface (Figure 5.5). Thus the enthalpy of a stearic acid exchange will be only marginally higher than that of a decanoic acid exchange, despite the theoretical ability of stearic acid to form eight more methylene-methylene interactions with the native oleate.
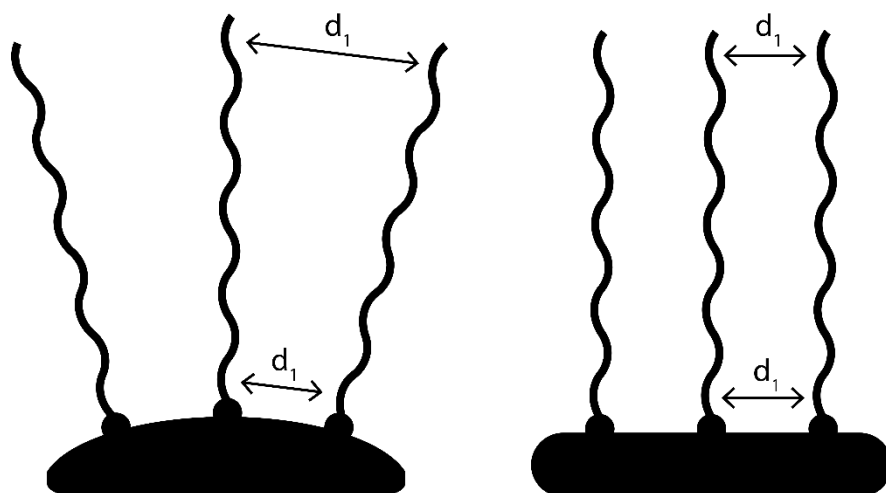
Figure 5.5: Effects of nanocrystal surface curvature on inter-ligand interactions: highly curved surfaces on small crystals increase the inter-ligand distance at increasing distances from the surface. Curvature increases the available cone angle for ligand binding.

Chapter 6: **Thermodynamics of phosphonate-carboxylate ligand exchange**

To further study the effects of head and tail groups on quantum dot surface reactions, we performed phosphonic acid ligand exchanges on the native nanocrystals as well (Figure 6.1). This reaction was chosen as a complement to the carboxylic acid exchanges because the tail groups could be similarly tuned in length but a different head group introduced a new component to the reaction driving force. Once again the tail groups were varying lengths of saturated alkyl chains, in this case with a range from 6-18 methyl units. The reactions were characterized by both calorimetry and quantitative NMR.
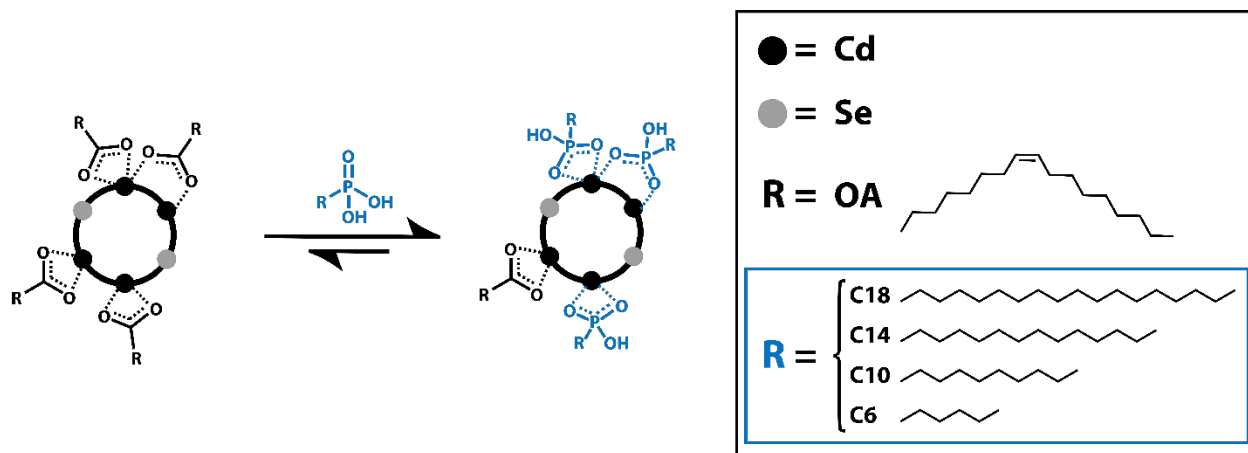
Figure 6.1: Ligand exchange from a carboxylate to a phosphonate binding group. Interaction effects are investigated using ligands with tails of different alkyl chain lengths, including hexyl-, decyl-, tetradecyl-, and octadecyl-phosphonic acids.

6.1 Surface coverage

Once again we determine ligand surface coverage by measuring bound and free oleate in the ligand exchange solution. In this new system, the native oleate ligand was strongly displaced along the

full course of the reaction, regardless of ligand tail length (Figure 6.2). We also see evidence of a breakdown in our assumption of one to one X-type exchange for phosphonic acid ligands. While there is some uncertainty in the measurement, native ligands appear to be displaced by a smaller number of phosphonate ligands as evidenced by values of $1-\theta$ above the one to one line in the plot (Figure 6.2C). It is possible that some of the phosphonic acid undergoes more than one deprotonation and oleate displacement during the initial phase of the reaction, as it does when forming Cd-phosphonate complexes, but the prevalence and degree to which the surface may reorganize later in the reaction is a matter for further research. This complete exchange of added phosphonic acid aliquots during even initial injections implies a strongly driven reaction and an equilibrium constant that is effectively infinite within the resolution of our measurements.
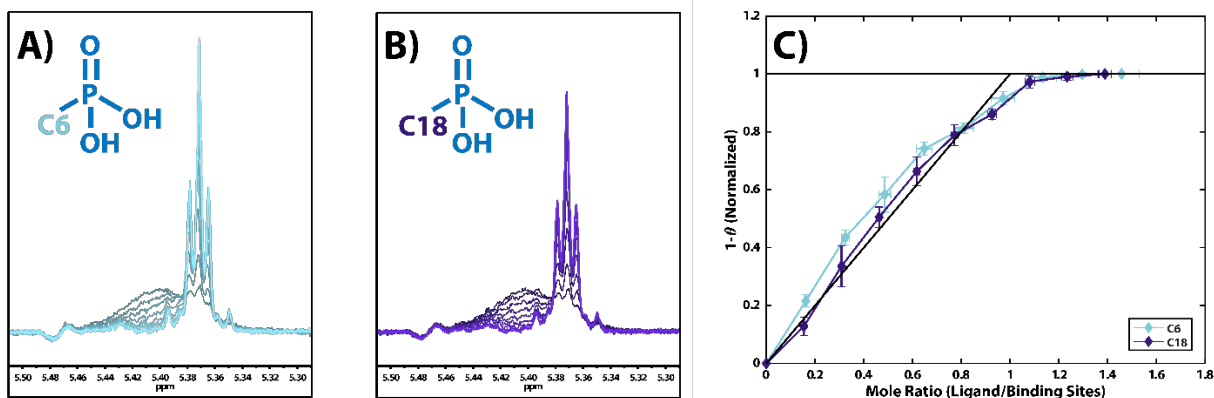
Figure 6.2: Quantitative NMR of phosphonic acid exchanges. A) Vinyl proton tracking of oleate displacement during exchange with hexylphosphonic acid, B) Vinyl proton tracking of oleate displacement during exchange with octadecylphosphonic acid, C) Normalized extent of ligand exchange as a function of the mole ratio of added surfactant to surface binding sites. Θ represents surface coverage of oleate ligand. Within error of the measurement, each injection of phosphonic acid binds fully.

6.2 Enthalpy of reaction

Phosphonic acid exchanges also show a significant ligand length dependence when characterized calorimetrically. Longer alkyl chains lead to a larger absolute exothermicity of the reaction, but an additional characteristic shape to the observed titration enthalpy is seen regardless of ligand length (Figure 6.4Figure 6.3B). Across multiple samples and concentrations, the ligand exchange reaction begins with an *endothermic* signal or enthalpy near zero, gradually becoming more and more exothermic until the nanocrystal surfaces begin to saturate with phosphonic acid ligand.
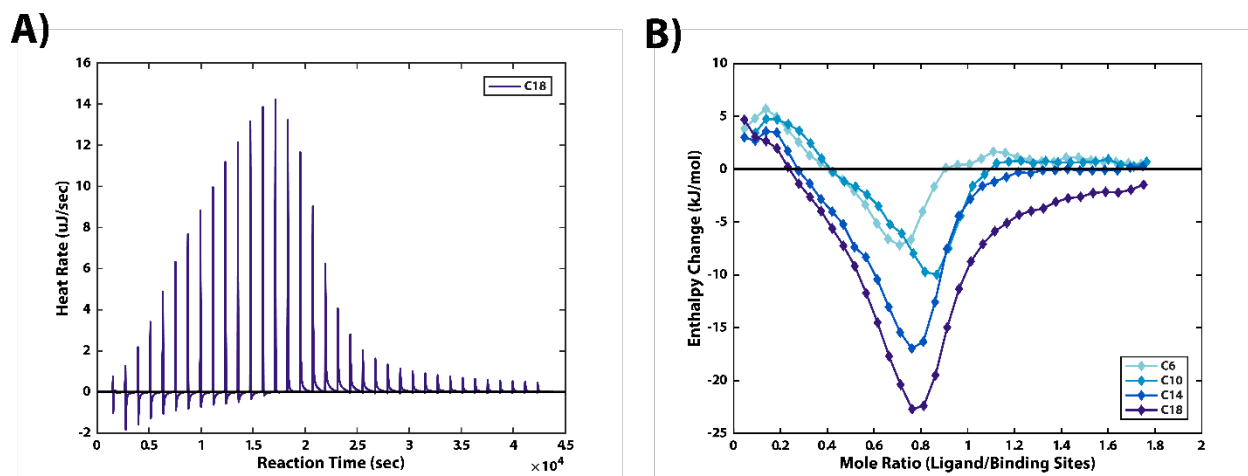
Figure 6.3: Isothermal titration calorimetry of phosphonic acid ligand exchanges. A) Raw heat rate signal measured during a representative ligand exchange with octadecylphosphonic acid, and B) enthalpy per mole ligand added, integrated for each ligand injection as a function of ligand mole ratio. Titrations with 4 different ligand tail groups show a strong dependence of reaction enthalpy on the alkyl chain length.

Under certain conditions, including addition of coordinating polar molecules or nanocrystal dilution in coordinating solvents, ligand-cation complexes may detach from the quantum dot surface and form a surface/solution equilibrium that can affect the characterization of ligand exchange[55]. During sample cleaning and storage such an equilibrium is formed and is measurable as a baseline free oleate vinyl peak in the quantitative NMR spectrum. These free complexes also undergo ligand exchange and contribute to the calorimetric signal, and phosphonic acid exchange on cation complexes proceeds in a 2-to-1 manner instead of the overall 1-to-1 seen on quantum dot surfaces. These exchanges can be accounted for given an accurate measurement of the initial free complex and an equivalent control exchange.

Given the strongly driven nature of the phosphonic acid exchange at all points in the titration, the initial endothermicity implies an entropically-driven process initiating the reaction, not the previously assumed greater binding affinity of the phosphonic acid head group. The eventual much more significant exothermic signal does indicate the binding affinity difference as an existing reaction component, but this is offset by other factors at the beginning of the exchange.

6.3 Proposed mechanisms

Phosphonic acid exchanges do not follow the trend observed with carboxylic acid ligands of an initially exothermic reaction, despite comparable tail groups. Overall, the enthalpy of reaction is much larger for phosphonic acid reactions and is not consistent with only Van der Waals forces as the source of reaction enthalpy. The initial stage of the reaction is strongly driven without a strong exothermic enthalpy change. This necessarily implies an entropically-driven reaction, and since the only factor that changed from the carboxylate reaction was the head group, any entropy change must be tied directly to the ligand binding group. Phosphonic acid binding moieties have increased steric bulk compared to carboxylic acids and their optimal binding geometry at the nanocrystal surface is determined by the functional group structure. While oleate ligands may not pack particularly well due to the rigidity imparted by a double bond, some level of inter-ligand

interaction is maintained, especially near the surface where ligands are packed more tightly. In this scenario, the exchange of a single carboxylate for a ligand with a phosphonate head group is likely to significantly disrupt the native ordering of the ligand shell and increase the overall entropy of the system (Figure 6.4C-2). The expected order of magnitude for these enthalpy and entropy changes just from packing interactions may be estimated using the enthalpy and entropy of fusion for oleic acid. If we assume full packing or 'frozen' ligand shell, disruption or 'melting' of the ligands requires an enthalpy increase of 39.6 kJ/mol while we see the entropy of the system increase by 138.4 J/mol*K (41.2 kJ/mol at 298 K)[123]. In this case, standard ligand melting would not fully account for a strongly driven reaction as the thermodynamic contributions balance each other out, but if packing is disrupted on a surface where ligands cannot reorient freely these contributions will be skewed. Given that the surface packing is limited by ligand binding density, these values are very rough estimates, but entropy changes of this magnitude should be sufficient to drive the initial ligand exchange reaction. Taking into account the expectation that Cd-phosphonate bonds are stronger than Cd-carboxylate bonds, the difference in the binding enthalpies should be balancing the Van der Waals disruption to some extent.

As the reaction progresses, it is expected that favorable inter-ligand interactions can begin to form between phosphonate ligands now present on the surface, once again decreasing the enthalpy of exchange. Some component of these interactions must come from interactions between and placement of the head groups themselves. Binding orientation may directly impact the effective density of ligand packing, as the alkyl chain length shows a much greater influence upon the enthalpy of reaction for phosphonates than for carboxylates. These favorable interactions, coupled with the favorable binding energy difference will first balance and then overwhelm the initial disruption of native interactions, leading to an increasingly exothermic reaction (Figure 6.4C-3,4). As the exchange reaction goes to completion, fewer native ligands are available for exchange and the calorimetric signal drops off accordingly (Figure 6.4C-5).
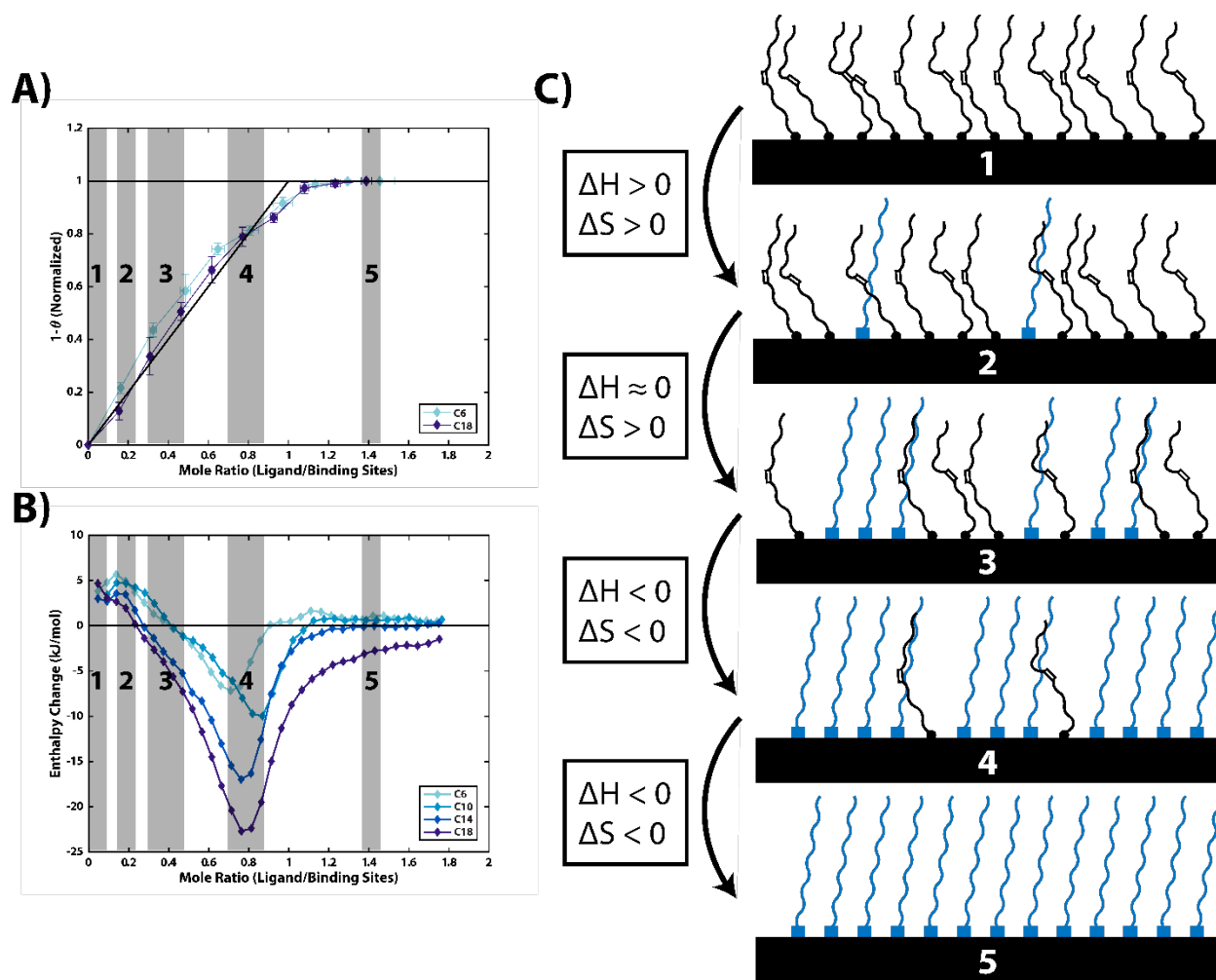
Figure 6.4: Contributing interactions in phosphonic acid exchanges. A) Ligand exchange surface coverage with phosphonic acids, marking surface snapshots, B) ligand exchange enthalpy per injection with phosphonic acids, marking surface snapshots, C) cartoon snapshots of native ligand shell (1), disruption of the native ligand shell by initial phosphonate exchange (2), disruption of native ligands with formation of phosphonate inter-ligand interactions (3), phosphonate packing disrupted by remaining native ligands (4), and full phosphonate ligand shell (5).

The entropic component of the reaction driving force is likely augmented in the phosphonic acid exchange by the ability of the phosphonic acid to displace more than one oleate ligand *via* two deprotonation events[124]. Although overall characterization of these ligand exchange reactions in past literature indicates a one to one exchange motif[93], the initial stages of the reaction show slightly greater oleate displacement than expected for complete exchange. Further work is needed to determine the significance of this mechanism and the degree to which the surface reorganizes upon continued exchange. Hexylphosphonic acid may also have a slightly lower pK_a than its longer chain counterparts, leading to a slightly higher amount of double deprotonation. Synthesis of an NMR labeled phosphonic acid is recommended for better understanding of the phenomenon.

Overall ligand surface density and surface curvature likely account for differences in signal and reaction progression between samples. Future work including a size series or progressive ligand stripping could improve our understanding of the system.

Chapter 7: Theoretical modeling and quantitative analysis of ligand exchange

Since characterizing quantum dot surface reactions *in situ* makes it very difficult to use direct observation techniques, understanding and analyzing the interplay between multiple thermodynamic factors is key to determining reaction mechanisms and surface structures. With a system of such apparent complexity, an intuitive mechanistic description is insufficient to define the process. We looked to adsorption isotherms, simulations of surface exchange, and numerical data fitting to fully capture the implications of all reaction parameters. Although each method had its limitations, inter-ligand interactions were shown to be consistent with the observed experimental results.

7.1 Surface coverage analysis: the adsorption isotherm

Adsorption isotherms are a well-studied way to analyze equilibria in surface-specific reactions[125]. The traditional surface adsorption experiment is done in the gas phase with a bare substrate and an adsorbing gas. The adsorbed surface coverage can then be determined as a function of the gas pressure in the experimental chamber, with the goal of determining the mechanism of molecular adsorption for the system. Isotherms are the models used to describe this data, and they are mathematically defined to include mechanistic assumptions about the reaction[126]. Fitting with an adsorption isotherm thus requires careful consideration of the likely interactions affecting adsorbed species. The better the fit of a particular isotherm, the more likely the associated mechanism is to be the correct interpretation.

The Langmuir isotherm is one of the simplest of all isotherms and provides a good basis for understanding these models in general[127]. It makes the assumption that the adsorbing molecules only fill the surface to a monolayer maximum, that they exhibit no intermolecular interactions, and that the binding affinity of the substrate does not change with amount of adsorbate bound. The isotherm then provides a relationship between the equilibrium constant K_{eq} and the adsorbate surface coverage θ as a function of adsorbate pressure as follows

$$\theta = \frac{K_{eq}P}{1 + K_{eq}P}$$

Langmuir isotherms are often the first pass in understanding surface coverage of an adsorbate[128], but there has been previous evidence that nanoscale ligand exchange reactions do not follow the reaction progression associated with this simple model[129]. In these cases we may consider other isotherms which take more complex interactions into account. These alternative models make their own assumptions that are only valid in specific conditions, and some are explicitly empirical. Table 7-1 details some of the most widely accepted adsorption isotherms and their uses[126].

Ligand exchange surface coverage may be fit to better understand the reaction equilibria, but adsorption models must be modified to accurately interpret the results. Exchange reactions introduce complications as the models are designed to characterize adsorption to a bare surface. In this case, it is fairly simple to derive these formulas using a modified equilibrium constant to account for all of the contributing concentrations. Ligand solvation modulates relative binding affinity, so all results are specific to the experimental solvent system. While in theory solution-phase concentrations may be substituted for gas-phase pressures in any standard adsorption

Table 7-1

Adsorption Isotherm	Functional Form (solution phase)	Assumptions & Notes	Suitable for analyzing nanocrystal surface reactions?
Langmuir	$$\theta = \frac{K_{eq}C}{1 + K_{eq}C}$$	• All surface sites are equivalent and independent of surface coverage • Monolayer max. adsorption	Yes
Freundlich	$$\theta = \alpha_f C^{C_f}$$	• Empirical fitting over small concentration ranges	No
Toth	$$\theta^{C_t} = \frac{\alpha_t C^{C_t}}{\frac{1}{K_{eq}} + C^{C_t}}$$	• Empirical fitting over small concentration ranges	No
Multi-site	$$\theta = \sum_i \frac{\chi_i K_{eq}^i C}{1 + K_{eq}^i C}$$	• Multiple non-interacting sites with different binding affinity • Monolayer max. adsorption	Yes
Fowler-Guggenheim	$$\ln K_{eq}C = \frac{\Delta H_{ad}^0 \alpha\theta}{k_B T} + \ln\left(\frac{\theta}{1-\theta}\right)$$	• Equivalent surface sites with a coverage-dependent interaction term • Monolayer max. adsorption	Yes
Temkin	$$\ln K_{eq}C = \frac{\Delta H_{ad}^0 \alpha\theta}{k_b T}$$	• Special case of Fowler-Guggenheim near 50% coverage • Monolayer max. adsorption	No
BET	$$\theta = \frac{c_B x_B}{(1 - x_B)(1 + (c_B - 1)x_B)}$$ $$x_B = C * K_m \qquad c_B = \frac{K_1}{K_m}$$	• Allows for multilayer adsorption • Reduces to a Langmuir isotherm when K_m is infinitesimally small	No

Notes: θ = surface coverage, K_{eq} = equilibrium constant, K_1 = equilibrium constant for first monolayer binding, K_m = equilibrium constant for multilayer binding, C = adsorbate concentration, α = fitting constant, C_f/C_t = fitting constant, k_B = Boltzmann constant, T = temperature, ΔH = inter-site interaction term

isotherms without problem, these concentrations are defined as the free adsorbate concentration at any given time. We are able to measure this value in our ligand exchanges with quantitative NMR, but the uncertainty is much higher than for the added ligand concentration.

Carboxylic acid exchanges are prime candidates for isotherm modeling of surface coverage because of the weakly driven nature of the reactions. The gradual change in surface coverage takes place over a larger range of added ligand concentration than that observed for strongly driven reactions, making the fits more robust. It can be shown that for an exchange reaction with equilibrium constant

$$K_{eq} = \frac{[QD-B][A]}{[QD-A][B]}$$

the relevant isotherm concentration term must be defined as

$$C = \frac{[B]}{[A]}$$

where all concentrations are the equilibrium values for a given injection (See appendix A-5 for further detail). Surface coverage of exchanged ligand is plotted as a function of C to find the value of K_{eq}, and this comparison shows some difference between short and long-chain ligands although the statistical significance of this difference is small. We looked closer at the isotherm models that have reasonable assumptions for nanocrystal surface binding. Fitting the data to a Langmuir isotherm, we are able to confirm a sub-unity equilibrium constant for both ligands but the initial steps of the reaction are not well accounted for (Figure 7.1A). A multi-site fitting reduces to the Langmuir model, where all individual equilibrium constants are equal, although the certainty of this fit is extremely low. To the best of our ability to interpret the results, this implies that multiple binding sites with different binding energies will not account for the inaccuracies in the Langmuir fit (Figure 7.1B). While there are likely some binding affinity differences site-to-site, on the ensemble level they are insignificant. Finally, we consider the Fowler-Guggenheim model, which assumes that there will be an average inter-ligand contribution to the energy of a surface that scales with the relative surface coverage of a given ligand (Figure 7.1C,D). The best fit given this model does not yield obviously better results, since the uncertainty in the data is large and any improvement in the fit may be the result of an increase in the number of fit degrees of freedom. Of note is the fact that the constants derived from this fit imply a decrease in favorable inter-ligand interactions with increased ligand length and a change in the binding energy of what ought to be equivalent head groups. Both of these observations call the validity of the model into question and the question of how binding and inter-ligand interactions affect ligand exchange reactions remains open.
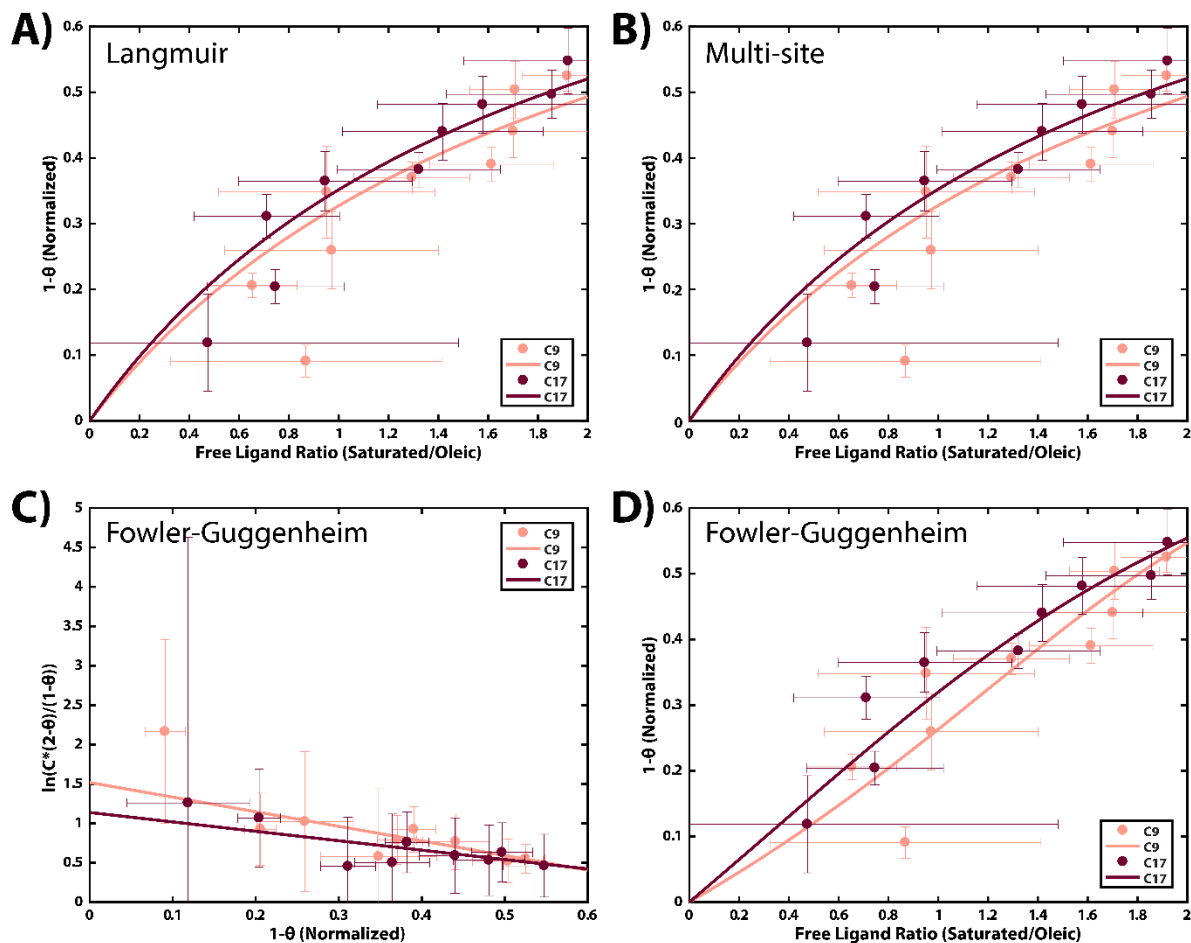
Figure 7.1: Isotherm fits of carboxylic acid ligand exchanges. A) modified Langmuir fits of C9 and C17 exchanges, B) Multi-site Langmuir fits are nearly identical to standard Langmuir fits, C) linearization of the Fowler-Guggenheim model enables fitting of surface coverage data, and D) fits to the Fowler-Guggenheim model are not obviously more representative than other models.

Meanwhile, phosphonic acid exchange reactions are much more complicated to analyze in this way precisely because they are so strongly driven. As the displacement of oleate ligands does not appear to be a perfect proxy for phosphonic acid binding, an additional degree of uncertainty must be added to any isotherm analysis. Numerical optimization of the isotherm may improve our ability to characterize the exchange, but it is expected to be minimally conclusive with so few data points available.

Table 7-2

Isotherms		Exchanged Ligand				
		Decanoic Acid (C9)			Stearic Acid (C17)	
Model	Parameter	Value	95% confidence		Value	95% confidence
Langmuir	K_{eq}	0.49	(0.39 , 0.58)		0.54	(0.46 , 0.63)
Multi-site (2 sites)	K_{eq}^1	0.49	(-4E5 , 4E5)		0.54	(-4E5 , 4E5)
	K_{eq}^2	0.49	(-4E5 , 4E5)		0.54	(-4E5 , 4E5)
Fowler-Guggenheim	$\dfrac{\Delta H_{ad}^0 \alpha}{kT}$	-1.9	(-3.1 , -0.6)		-1.2	(-2.4 , 0)
	$-\ln(K_{eq})$	1.5	(1.0 , 2.1)		1.1	(0.6 , 1.7)

7.2 Monte Carlo simulations

Further analysis is needed to determine the interacting driving forces in this system and take the enthalpy of reaction into account. To this end, simple surface and exchange modeling may be performed using a mean-field Monte Carlo simulation. In the same way that nearest neighbor interactions from a single spin can be accounted for in the overall energy and phase transition temperature of the standard magnetic Ising model[127], different kinds of nearest neighbor interactions can be modeled for ligands on a surface of finite size with periodic boundary conditions. Both native and incoming ligands are assigned a value for binding energy, and inter-ligand interaction energies are set for native-native, native-new, and new-new nearest neighbor configurations (Figure 7.2). The contributions of each kind of interaction are then weighted proportionally to their current prevalence in the system, and the energy of the surface is calculated accordingly. In order to determine the enthalpic effects of a ligand exchange in such a model, we then calculate the change in energy of the surface as the reaction progresses in response to the available density in solution of incoming ligand (Appendix A-6). The assumptions made in this model result in an effective simulation of the Fowler-Guggenheim isotherm in which both enthalpy change and surface coverage may be considered for a more complete picture.
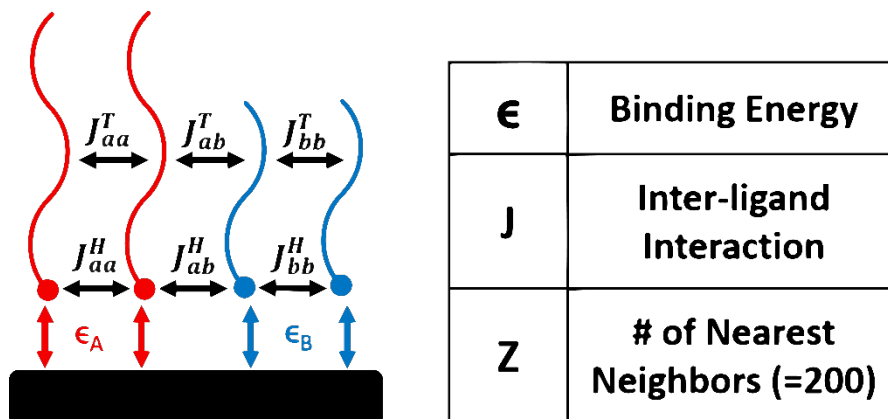
Figure 7.2: Interactions contributing to a simple surface model: binding energies (ϵ), inter-ligand interactions originating from both head and tail group interactions (J^H and J^T, respectively), and the number of overall inter-ligand interactions (Z)

The progress of the surface exchange can be defined and controlled by introducing a sliding scale of relative ligand chemical potentials. The chemical potential is then used to define a density of incoming ligands in solution, analogous to the pressures used in gas-phase adsorption isotherms. It is then additionally possible to determine the average surface state of the simulated nanoparticle at any given point in the reaction. Comparing the modeled results to our experimental observations, we see confirmation of the potential for these inter-ligand interactions to contribute to the overall enthalpy of reaction (Table 7-3). Making the assumption that a significant contribution to the inter-ligand interactions comes from head group interactions, either through direct interactions or modulation of the spacing and packing of the ligand chains, a significant difference in the energy of reaction profile between the two classes of ligand exchange. The qualitative profiles observed reproduce the experimental enthalpy per injection as well as can be expected from such a simplified model of surface interactions (Figure 7.3A,D).

Table 7-3

Head Group	Tail Length	$\Delta\varepsilon$ (kJ/mol)	$\Delta J*Z$ (kJ/mol)
Carboxylate	C9	0.20	-0.20
	C13	0.35	-0.35
	C17	0.5	-0.50
Phosphonate	C6	-1.50	5.60
	C10	-1.50	6.10
	C14	-1.50	6.75
	C18	-1.50	7.15

These results by themselves, however, are no more than indicative of the reaction mechanism. It is also possible to calculate a theoretical surface coverage corresponding to the optimized interaction parameters, and while the carboxylic acid exchanges are reproduced well there are unexpected features in the phosphonic acid exchange surface coverage (Figure 7.3B,E). There appears to be a predicted threshold phosphonic acid density needed to reach a strongly-driven reaction response. To understand this discrepancy, we must remember that a model of this kind oversimplifies the system significantly. A simple mean field approximation like the one used here wholly neglects organizational surface entropy, taking into account only the chemical potential of species in solution and the energetic contributions to the equilibrium (the modeled system is by default volume-invariant rather than isobaric, so the calculated values of a nanoparticle surface will result in a calculated internal energy of the system rather than an enthalpy. Given the other constraints on the system, these values should be meaningfully comparable.). As such, it is unsurprising that the calculated surface coverage as a function of ligand density in solution would be lower than expected values in the initial phases of exchange. The reaction in the phosphonic acid case begins as an entropically-driven process and without an entropy simulation component the modeled reaction lacks sufficient driving force.

Additionally, new ligand density in solution, although directly analogous to the standard parameters considered in adsorption isotherms, is not an easily-determined value in our colloid-based experimental system. As mentioned previously, solution-phase concentrations are calculated as added surfactant per volume and subsequent reaction changes this concentration value at equilibrium. In reactions with very small equilibrium constants and large ambient reagent concentrations, one can make the assumption that the difference is negligible and treat concentration added as the concentration in solution at equilibrium. In reactions that are somewhat more favorable, however, including ligand exchange protocols with equilibrium constant either above or approaching unity, calculated and equilibrium concentrations can be strikingly different. Careful NMR analysis can provide insight into these equilibria but the certainty of our analysis suffers as a result, as seen in our isotherm analysis (Figure 7.1).

Lastly, any uncertainty that exists regarding the one to one nature of these ligand exchanges may mean that the experimental observations diverge from the simplified model. If, for example, the phosphonic acid exchanges do in fact participate in partial double-deprotonation and displace native ligands with an unexpected stoichiometry, the overall equilibrium and the effect of inter-ligand interactions may be affected. The major risk with this uncertainty is that the optimization of interaction parameters may be incorrect. An NMR-tagged phosphonic acid ligand could aid in determining the extent of this effect, but once again resolution is a concern. At this point, we may be able to confirm the existence of some doubly-deprotonated phosphonate ligands, but the percentage of each binding type in a given injection is unlikely to be ascertained to any degree of confidence.
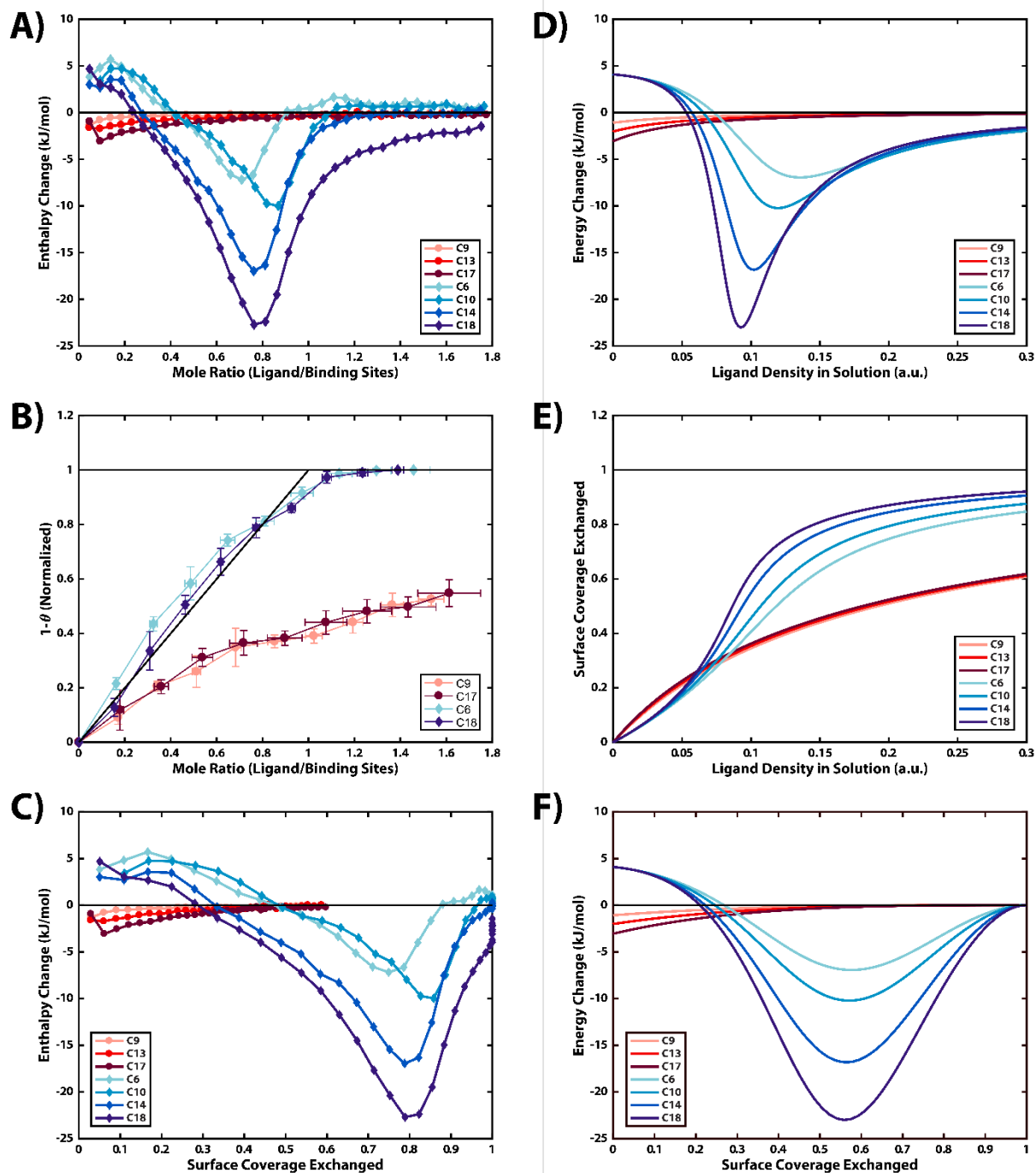
Figure 7.3: Experimental and modeled results for carboxylate and phosphonate exchanges: Experimental - A) enthalpy change (kJ/mol) per mole ligand added as function of ligand added, B) surface coverage of new ligand as a function of ligand added, C) enthalpy change (kJ/mol) per mole ligand added as function of surface coverage new ligand, as compared to modeled - D) energy change per injection (kJ/mol) per mole ligand added as function of ligand density in solution, B) surface coverage of new ligand as a function of ligand density in solution, C) energy change (kJ/mol) per mole ligand added as function of surface coverage new ligand.

Plotting enthalpy per injection as a function of exchanged surface coverage enables us to confirm our qualitative results despite some of the oversimplifications in the model. The overall reaction entropy and driving force no longer comes into play since we observe the enthalpy of exchange at well-defined surface coverages, and the definitions of ligand density and concentration added no longer matter as they cancel out. Using this approach we see qualitative agreement of the model and experiment once again, but with a bit more uncertainty in the enthalpy profile. This may be due to the uncertainty of phosphonic acid double binding and the effect it could have on inter-ligand interactions or it may be related to some other variation in the surface interactions over the course of the reaction. More study is needed to determine how these interactions might vary, but we are able to conclude that inter-ligand interactions as modeled are generally consistent with the experimental characterization of ligand exchange.

7.3 Numerical data fitting
We can return to a data-driven approach to understanding the surface mechanics by using the optimization of isotherms dependent on the enthalpy of reaction. This holds the potential to better account for entropic contributions and the overall process since we have higher resolution and the ability to characterize two thermodynamic parameters with the calorimetry technique. We must still make assumptions about the appropriate model to use, much as with surface coverage based isotherms, but the equilibrium constant is not defined as a function of binding and interaction enthalpies alone. We can then use the exchange enthalpy in conjunction with the equilibrium constant to elucidate the entropic contributions to the reaction. With further development, these models can be used to predict the surface coverage data from our NMR exchange experiments and further our understanding of surface reactions.

Chapter 8: Development of alternative surface architectures
Ensemble studies of quasi-spherical monodisperse quantum dots will always carry some mechanistic uncertainty and lack site/facet specificity. It has many times been proposed in theory, and indeed shown on bulk surfaces, that different crystal facets and kinds of sites present different functional group binding affinities. To address this, we envisioned other material architectures with greater control over the semiconductor surface structure. A number of synthetic modifications can be made to control the average coordination of surface atoms or select for specific facets.

8.1 Size effects
Based on our current results, we propose that nanocrystals with a smaller diameter may show a decreased effect from inter-ligand interactions, as their higher curvature will increase available space between ligand tail groups and individual facets will be less well-defined. This hypothesis provides an opportunity for future study, and we have done some preliminary examinations of this system. Oleate-based syntheses without additional stabilizing agents are less controllably affected by growth time than many CdSe quantum dot syntheses, so size tunability is achievable only through the modification of relative precursor concentrations, growth temperature, and other synthetic conditions. Given the significant variance in reaction parameters necessary to optimize for a particular nanocrystal size, great care must be taken to confirm that the different samples are equivalent in all other respects if the size dependence of ligand binding and interactions is to be studied further.
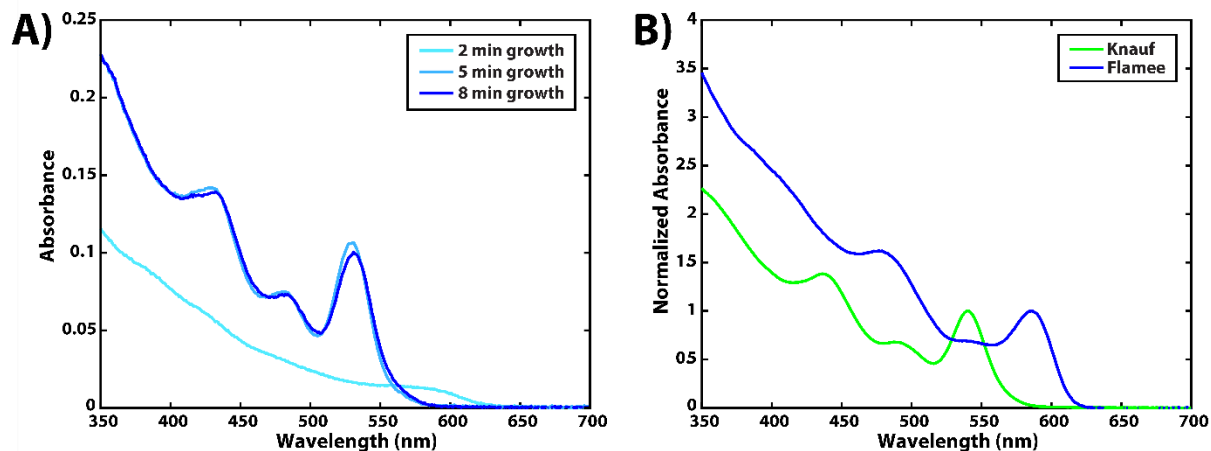
Figure 8.1: Control of amine-free CdSe synthesis using oleate precursors. A) Quantum dot size/optical properties after different growth times for the adapted synthetic conditions proposed by Flamee et. al.with low precursor loading. Continued growth leads to a larger linewidth but sees minimal overall effect on nanocrystal size. B) Optimized nanocrystal size/optical properties for quantum dots synthesized using conditions adapted from Knauf et. al. (green) and Flamee et. al. (blue, high precursor loading).

8.2 Controlled faceting

Small CdSe spheres do not present defined facets, making it difficult to determine preferential ligand binding. There has been theoretical work proposing ligand binding to only sites with specific termination, or at the very least a significant difference in binding affinity[130–134]. Ligand exchange studies of highly faceted nanoparticles with controlled surface termination could show these differences *in situ* and give insight into the contributions to the ensemble reaction we observe with spherical CdSe particles. Growth of large particles enables the synthesis of controlled morphologies and increases the definition of surface facets. The most commonly studied CdSe facets in the zinc blende crystal structure are the [100] and [111] facets, so selecting for this faceting may give insights to how ligand binding to them proceeds at the nanoscale.

There is some precedent in the literature for shape control and highly faceted CdSe syntheses[135–140], most of the work having been done with wurtzite particles. A study from Liu et. al. claims highly-faceted zinc blende nanocrystals can be synthesized using a heat up reaction and shape control derived from growth temperature[141]. We targeted [100]-terminated cubes and [111]-terminated tetrahedral for further surface studies. While, preliminary syntheses of these materials do in fact show a high degree of faceting, reproducible conditions leading to strong shape control have not been found. Variation in the growth temperature or reagent impurities between the original study and our reactions may account for some of this difference. We find that we are able to grow faceted particles with a mix of morphologies with the highest degree of success in selecting for tetrahedral crystals.
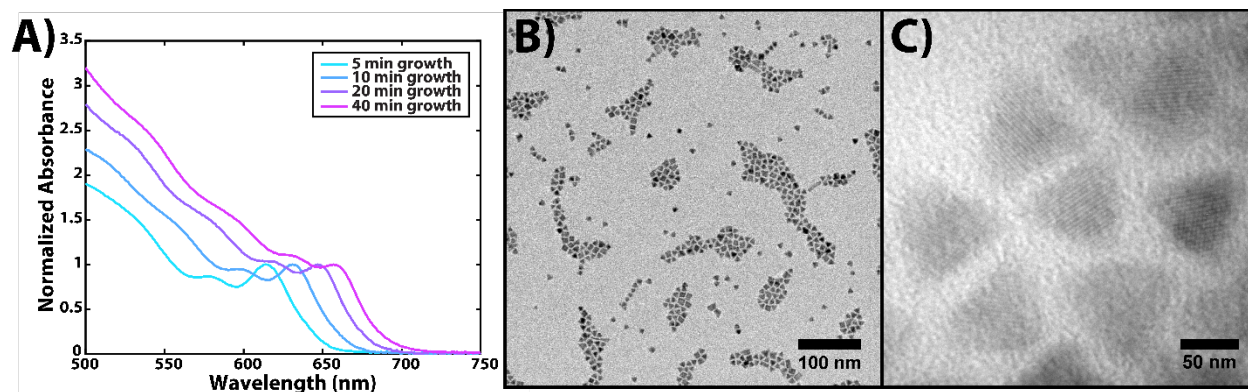
Figure 8.2: Synthesis of highly faceted CdSe nanocrystals. A) Quantum dot size dependence on growth time for a heat-up reaction, B) TEM image of roughly tetrahedral nanocrystals after 40 minutes of growth reaction, and C) high magnification TEM image shows degree of polydispersity and different potential projection axes for these particles.

8.3 CdSe nanoplatelets

Another nanoparticle morphology that could elucidate the effects of curvature and faceting in our current studies is a quasi-2D structure. CdSe nanoplatelet synthesis is the subject of a good deal of study[142–148], with questions remaining about the growth mechanism and synthesis optimization for monolayer level control of the platelet thickness in high demand. With their large facets and visible emission we expect that ligand exchange reactions should have similar effects on nanoplatelet properties as standard quantum dot exchanges, but that any inter-ligand interaction effects will be enhanced by the packing of ligands on a single facet.

Controlled nanoplatelets were synthesized using a method adapted from Ithurria et. al., and were determined to be 5.5 monolayers in thickness (Figure 8.3)[148]. Anisotropic nanoplatelet synthesis is a relatively unfavorable mechanism of growth post-nucleation, so yield is low and selective centrifugation is necessary to separate the platelets from the quantum dot by-products. An initial post-synthetic ligand exchange with oleic acid was attempted, as a mixture of saturated carboxylic acids is the requisite synthesis ligand. Preliminary results show the apparent difficulty of removing excess ligand without triggering nanoplatelet assembly or aggregation, but controlled addition of cadmium oleate complex during the cleaning process improves outcomes. Further optimization of the system will be needed if it is to be used for well-constrained surface characterization, as overall colloidal stability remains low and NMR characterization has been unable to confirm a significant amount of oleate binding on the sample at any stage in the purification process.
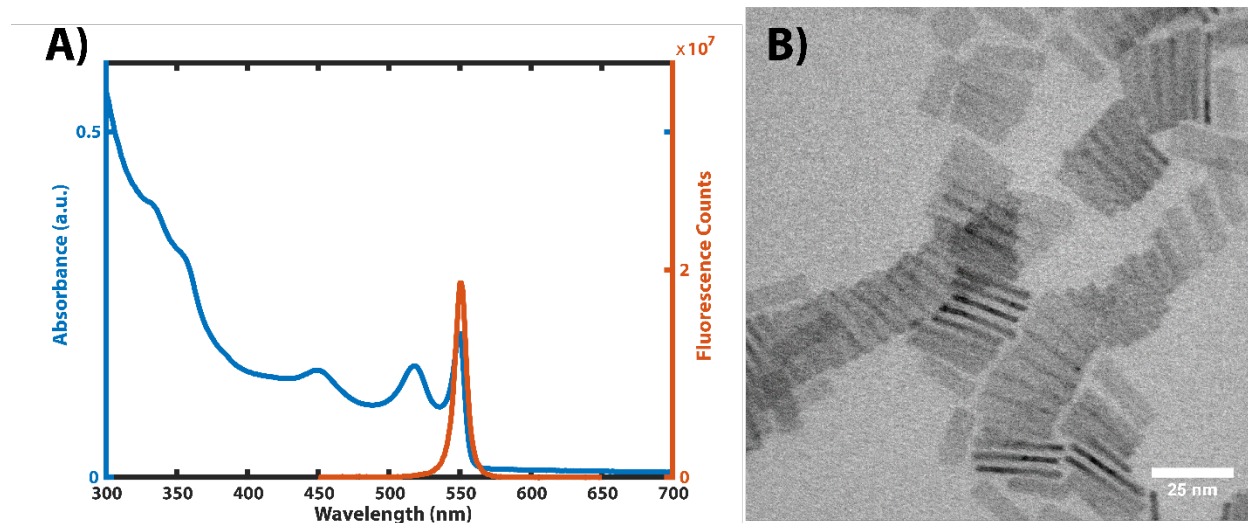
Figure 8.3: Characterization of optimized CdSe nanoplatelets. A) Absorbance and fluorescence spectra of CdSe nanoplatelets, B) TEM of nanoplatelet sample.

Chapter 9: Further indicators of surface structure

9.1 Colloidal stability and ligand exchange

As has been mentioned previously, the quantum dot ligand shell has a significant impact on solvent-particle interactions and colloidal stability. These effects are usually seen with ligand stripping or a transition from a ligand with a non-polar to a polar tail group, or vice versa, depending on the solvent system. In the special case of our CdSe ligand exchange reactions, we are working with exclusively ligands with a non-polar solvent facing moiety, but we still observe a strong shift in colloidal stability over the course of the reaction. Complete phosphonic acid exchange leads to a marked reduction in the stability of quantum dots in THF, despite the fact that wurtzite CdSe with native phosphonates of the same tail structure do not exhibit issues with colloidal stability. This suggests that the specific crystal structure and faceting in zinc blende CdSe quantum dots may yield more alkyl chain packing than their wurtzite counterparts, and thus reduce ligand-solvent interactions. Colloidal stability of nanocrystals has recently been shown to vary with solution temperature and tail branching of otherwise equivalent hydrophobic ligands, with more 'entropic' ligands and higher temperatures yielding more ligand/solvent interpenetration and better solubility[149,150]. This is consistent with our proposed increase in surface ordering upon phosphonate exchange. The previous results imply that at room temperature, simple ligands with unbranched, saturated alkyl chains lack sufficient packing entropy to stabilize high concentrations of particles with diameter greater than 2.5 nm. Given the relative difficulty of achieving full exchange with a carboxylic acid ligand, thus far we have been unable to determine whether the phosphonate binding group decreases ligand entropy beyond simple alkane packing. Further study of the stability effects of saturated-chain ligands on zinc blende CdSe could provide another qualitative measure of surface packing through an inverse relationship with solvent intercalation.

37

9.2 Nonlinear spectroscopy of nanocrystal surface structures

It also is desirable to characterize nanocrystal ligand binding and structure using a direct technique if possible, but most direct surface-sensitive measurements that are used on bulk interfaces are not suitable for the study of nano-structures. Often spatial resolution is inadequate and the technique is incompatible with a solvent environment, possibly even requiring a measurement of the substrate under high vacuum conditions. Sum frequency generation, however, which relies on the symmetry of the sample for its surface sensitivity, is capable of discerning the outer structure of a nanocrystal ligand shell even with spherical particles[151–154].

Sum frequency generation is a non-linear spectroscopy technique in which the allowed vibrational resonances are determined by the second order component of the molecular nonlinear susceptibility[155]. Upon exposure to high electromagnetic fields, the non-linear components of the field, and therefore the susceptibilities, must be taken into account when determining the instantaneous material polarization[156],

$$P = P^{(1)} + P^{(2)} + \cdots = \varepsilon_0(\chi^{(1)}E^{(1)} + \chi^{(2)}E^{(2)} + \cdots)$$

where P is the material polarization, ε0 is the vacuum permittivity, χ is the susceptibility, and E is the electromagnetic field, with superscripts denoting first, second, and higher order terms. Second order polarization is only observed in non-centrosymmetric media, which is the origin of the interface sensitivity of the generated signal. There are multiple components comprising the second order polarization in response to strong fields of two different frequencies, but phase matching enables the selection of the sum frequency as the only component with significant signal intensity. This sum frequency polarization is defined as

$$P_{SF}^{(2)} = \varepsilon_0\chi^{(2)}E_1E_2$$

and yields an emission with frequency

$$\omega_{SF} = \omega_1 + \omega_2$$

It is common to probe interfacial vibrational modes using visible/IR SFG, in which a fixed visible frequency laser is used as one excitation contribution and a second IR laser is scanned across the frequency range of interest such that the sum frequency signal is detected in the visible range. Characteristic signals of various functional groups can then be noted, and frequency shifts in the resonance can be analyzed to determine the interface environment, including the prevalence of gauche configurations and CH_3/CH_2 ratios at the surface of alkyl monolayers[157]. These factors are then used to determine the ordering and packing angle of surface species.

In the case of our ligand exchanged quantum dots, we were able to characterize the ligand environment of pure oleate, pure octadecylphosphonate, and 50/50 mixed ligand shells in low density quantum dot films (Figure 9.1). In measurements using an SSP polarization profile, a decrease in the CH_3/CH_2 ratio is observed going from the native ligand shell to an intermediate mixed shell, indicating a decrease in the ordering of alkyl chains at the interface (Figure 9.1A). Upon further exchange to a full phosphonate shell, an even more significant increase in the ratio is seen, supporting our model of increased ligand ordering for saturated chain ligand shells. Slight

differences in the signal observed using SPS polarization to probe horizontally-oriented modes imply an overall change in the packing angle of surface species as the ligand shell changes (Figure 9.1B). As these measurements were performed with nanocrystal films in air, the ligand packing results should not be viewed as a direct confirmation of the ordering hypothesis in the solution phase. It is possible to observe SFG from interfaces in a liquid cell, and some work has been done to characterize adsorbed nanocrystal films in this manner[158]. Similar measurements in organic solvents could be done to better determine the in situ structure of the quantum dot surface during controlled ligand exchange.
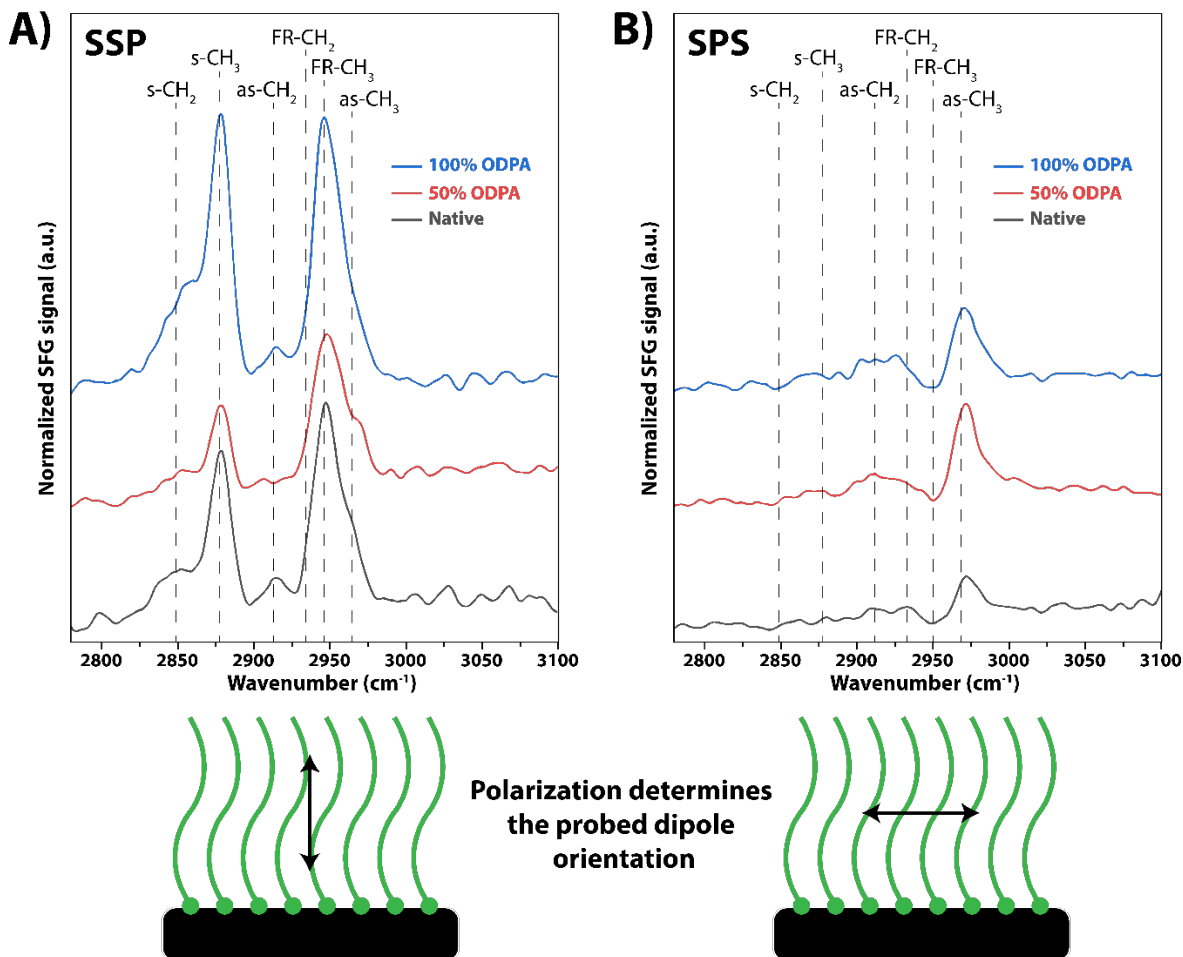
Figure 9.1: Sum frequency generation of ligand ordering in low-density quantum dot films. A) SSP polarization probing vertically-oriented IR modes and B) SPS polarization probing horizontally-oriented IR modes.

Chapter 10: Conclusion

In this work, we have taken a multi-faceted approach to characterizing quantum dot surface structure and dynamics in order to gain insight into the contributions of inter-ligand phenomena that have previously been difficult to take into account. Theoretical studies have postulated the importance of non-binding components to surface structure optimization, but NMR studies alone

do not have the resolution necessary to paint a complete picture of the interaction profile. We show that isothermal titration calorimetry enables measurement of ligand exchange thermodynamics with a much higher degree of certainty and given appropriate analysis can be used for complex characterization. Although previous use of ITC for nanomaterial characterization has focused on simple surface models, supporting experiments and observations provide constraints can support the determination of reasonable models for a full range of surface interactions.

Future research will expand on this model system to further explore the effects of faceting, morphology, and crystal structure on the individual binding and collective effects of nanocrystal ligands. A library of model ligands should be developed for controlled exchange and facile characterization *via* NMR and optical spectroscopy to provide more constrained measurement of surface reactions and enable generalization of our methods to a wide array of nanomaterials. We expect the basic principles of surface structure determination to remain constant across multiple material systems, but the implications of precursor and surface reactivity and of crystal structure mediated ligand density are likely significant. The eventual objective of such surface characterization should be the determination of design rules for functional ligands, focusing on synthesis and end-use applications.

References

(1)   Karakoti, A. S.; Sanghavi, S.; Nachimuthu, P.; Yang, P.; Thevuthasan, S. Probing the Size- and Environment-Induced Phase Transformation in CdSe Quantum Dots. *J. Phys. Chem. Lett.* **2011**, *2* (22), 2925–2929.

(2)   Kriegel, I.; Jiang, C.; Rodríguez-Fernández, J.; Schaller, R. D.; Talapin, D. V.; da Como, E.; Feldmann, J. Tuning the Excitonic and Plasmonic Properties of Copper Chalcogenide Nanocrystals. *J. Am. Chem. Soc.* **2012**, *134* (3), 1583–1590.

(3)   Jasieniak, J.; Califano, M.; Watkins, S. E. Size-Dependent Valence and Conduction Band-Edge Energies of Semiconductor Nanocrystals. *ACS Nano* **2011**, *5* (7), 5888–5902.

(4)   Larouche, S.; Tsai, Y.-J.; Tyler, T.; Jokerst, N. M.; Smith, D. R. Infrared Metamaterial Phase Holograms. *Nat. Mater.* **2012**, *11* (5), 450–454.

(5)   Boltasseva, A.; Shalaev, V. M. Fabrication of Optical Negative-Index Metamaterials: Recent Advances and Outlook. *Metamaterials* **2008**, *2* (1), 1–17.

(6)   El Mel, A.-A.; Molina-Luna, L.; Buffière, M.; Tessier, P.; Du, K.; Choi, C.-H.; Kleebe, H.-J.; Konstantinidis, S.; Bittencourt, C.; Snyders, R. Electron Beam Nanosculpting of Kirkendall Oxide Nanochannels. *ACS Nano* **2014**, *8* (2), 1854–1861.

(7)   Pan, D.; Fu, M.; Yu, X.; Wang, X.; Zhu, L.; Nie, S.; Wang, S.; Chen, Q.; Xiong, P.; von Molnár, S.; et al. Controlled Synthesis of Phase-Pure InAs Nanowires on Si(111) by Diminishing the Diameter to 10 Nm. *Nano Lett.* **2014**, *14* (3), 1214–1220.

(8)   Peng, Z. A.; Peng, X. Formation of High-Quality CdTe, CdSe, and CdS Nanocrystals Using CdO as Precursor. *J. Am. Chem. Soc.* **2001**, *123* (1), 183–184.

(9)   Krommenhoek, P. J.; Wang, J.; Hentz, N.; Johnston-Peck, A. C.; Kozek, K. A.; Kalyuzhny, G.; Tracy, J. B. Bulky Adamantanethiolate and Cyclohexanethiolate Ligands Favor Smaller Gold Nanoparticles with Altered Discrete Sizes. *ACS Nano* **2012**, *6* (6), 4903–4911.

(10)   Protesescu, L.; Yakunin, S.; Bodnarchuk, M. I.; Krieg, F.; Caputo, R.; Hendon, C. H.; Yang, R. X.; Walsh, A.; Kovalenko, M. V. Nanocrystals of Cesium Lead Halide Perovskites (CsPbX 3 , X = Cl, Br, and I): Novel Optoelectronic Materials Showing Bright Emission with Wide Color Gamut. *Nano Lett.* **2015**, *15* (6), 3692–3696.

(11)   Wu, W.; He, Q.; Jiang, C. Magnetic Iron Oxide Nanoparticles: Synthesis and Surface Functionalization Strategies. *Nanoscale Res. Lett.* **2008**, *3* (11), 397–415.

(12)   Zhang, J.; Liu, H.; Wang, Z.; Ming, N. Shape-Selective Synthesis of Gold Nanoparticles with Controlled Sizes, Shapes, and Plasmon Resonances. *Adv. Funct. Mater.* **2007**, *17* (16), 3295–3303.

(13)   Zhou, K.; Li, Y. Catalysis Based on Nanocrystals with Well-Defined Facets. *Angew. Chemie Int. Ed.* **2012**, *51* (3), 602–613.

(14)   Chen, O.; Zhao, J.; Chauhan, V. P.; Cui, J.; Wong, C.; Harris, D. K.; Wei, H.; Han, H.-S.; Fukumura, D.; Jain, R. K.; et al. Compact High-Quality CdSe–CdS Core–shell

Nanocrystals with Narrow Emission Linewidths and Suppressed Blinking. *Nat. Mater.* **2013**, *12* (5), 445–451.

(15)   Bronstein, N. D.; Yao, Y.; Xu, L.; O'Brien, E.; Powers, A. S.; Ferry, V. E.; Alivisatos, a. P.; Nuzzo, R. G. Quantum Dot Luminescent Concentrator Cavity Exhibiting 30-Fold Concentration. *ACS Photonics* **2015**, 150821134054007.

(16)   McDonald, S. A; Konstantatos, G.; Zhang, S.; Cyr, P. W.; Klem, E. J. D.; Levina, L.; Sargent, E. H. Solution-Processed PbS Quantum Dot Infrared Photodetectors and Photovoltaics. *Nat. Mater.* **2005**, *4* (2), 138–142.

(17)   Tang, J.; Kemp, K. W.; Hoogland, S.; Jeong, K. S.; Liu, H.; Levina, L.; Furukawa, M.; Wang, X.; Debnath, R.; Cha, D.; et al. Colloidal-Quantum-Dot Photovoltaics Using Atomic-Ligand Passivation. *Nat. Mater.* **2011**, *10* (10), 765–771.

(18)   Li, W.; Zhong, X. Capping Ligand-Induced Self-Assembly for Quantum Dot Sensitized Solar Cells. *J. Phys. Chem. Lett.* **2015**, *6* (5), 796–806.

(19)   Zrazhevskiy, P.; Sena, M.; Gao, X. Designing Multifunctional Quantum Dots for Bioimaging, Detection, and Drug Delivery. *Chem. Soc. Rev.* **2010**, *39* (11), 4326.

(20)   Scheele, M.; Hanifi, D.; Zherebetskyy, D.; Chourou, S. T.; Axnanda, S.; Rancatore, B. J.; Thorkelsson, K.; Xu, T.; Liu, Z.; Wang, L.-W.; et al. PbS Nanoparticles Capped with Tetrathiafulvalenetetracarboxylate: Utilizing Energy Level Alignment for Efficient Carrier Transport. *ACS Nano* **2014**, *8* (3), 2532–2540.

(21)   Luo, X.; Liu, P.; Truong, N. T. N.; Farva, U.; Park, C. Photoluminescence Blue-Shift of CdSe Nanoparticles Caused by Exchange of Surface Capping Layer. *J. Phys. Chem. C* **2011**, *115* (43), 20817–20823.

(22)   Antanovich, A.; Prudnikau, A.; Matsukovich, A.; Achtstein, A.; Artemyev, M. Self-Assembly of CdSe Nanoplatelets into Stacks of Controlled Size Induced by Ligand Exchange. *J. Phys. Chem. C* **2016**, *120* (10), 5764–5775.

(23)   Fafarman, A. T.; Koh, W.; Diroll, B. T.; Kim, D. K.; Ko, D.-K.; Oh, S. J.; Ye, X.; Doan-Nguyen, V.; Crump, M. R.; Reifsnyder, D. C.; et al. Thiocyanate-Capped Nanocrystal Colloids: Vibrational Reporter of Surface Chemistry and Solution-Based Route to Enhanced Coupling in Nanocrystal Solids. *J. Am. Chem. Soc.* **2011**, *133* (39), 15753–15761.

(24)   Lim, S. J.; Ma, L.; Schleife, A.; Smith, A. M. Quantum Dot Surface Engineering: Toward Inert Fluorophores with Compact Size and Bright, Stable Emission. *Coord. Chem. Rev.* **2016**, *320–321*, 216–237.

(25)   Zillner, E.; Fengler, S.; Niyamakom, P.; Rauscher, F.; Köhler, K.; Dittrich, T. Role of Ligand Exchange at CdSe Quantum Dot Layers for Charge Separation. *J. Phys. Chem. C* **2012**, *116* (31), 16747–16754.

(26)   Ye, X.; Jones, M. R.; Frechette, L. B.; Chen, Q.; Powers, A. S.; Ercius, P.; Dunn, G.; Rotskoff, G. M.; Nguyen, S. C.; Adiga, V. P.; et al. Single-Particle Mapping of Nonequilibrium Nanocrystal Transformations. *Science (80-.).* **2016**, *354* (6314).

(27)   Giansante, C.; Infante, I. Surface Traps in Colloidal Quantum Dots: A Combined Experimental and Theoretical Perspective. *J. Phys. Chem. Lett.* **2017**, *8* (20), 5209–5215.

(28)   O'Neil, M.; Marohn, J.; McLendon, G. Dynamics of Electron-Hole Pair Recombination in Semiconductor Clusters. *J. Phys. Chem.* **1990**, *94* (10), 4356–4363.

(29)   Hollingsworth, J. A. Heterostructuring Nanocrystal Quantum Dots Toward Intentional Suppression of Blinking and Auger Recombination. *Chem. Mater.* **2013**, *25* (8), 1318–1331.

(30)   Veamatahau, A.; Jiang, B.; Seifert, T.; Makuta, S.; Latham, K.; Kanehara, M.; Teranishi, T.; Tachibana, Y. Origin of Surface Trap States in CdS Quantum Dots: Relationship between Size Dependent Photoluminescence and Sulfur Vacancy Trap States. *Phys. Chem. Chem. Phys.* **2015**, *17* (4), 2850–2858.

(31)   Pu, C.; Qin, H.; Gao, Y.; Zhou, J.; Wang, P.; Peng, X. Synthetic Control of Exciton Behavior in Colloidal Quantum Dots. *J. Am. Chem. Soc.* **2017**, *139* (9), 3302–3311.

(32)   Sitt, A.; Hadar, I.; Banin, U. Band-Gap Engineering, Optoelectronic Properties and Applications of Colloidal Heterostructured Semiconductor Nanorods. *Nano Today* **2013**, *8* (5), 494–513.

(33)   Dabbousi, B. O.; Rodriguez-Viejo, J.; Mikulec, F. V; Heine, J. R.; Mattoussi, H.; Ober, R.; Jensen, K. F.; Bawendi, M. G. (CdSe)ZnS Core−Shell Quantum Dots: Synthesis and Characterization of a Size Series of Highly Luminescent Nanocrystallites. *J. Phys. Chem. B* **1997**, *101* (46), 9463–9475.

(34)   Ghosh Chaudhuri, R.; Paria, S. Core/Shell Nanoparticles: Classes, Properties, Synthesis Mechanisms, Characterization, and Applications. *Chem. Rev.* **2012**, *112* (4), 2373–2433.

(35)   Nasilowski, M.; Nienhaus, L.; Bertram, S. N.; Bawendi, M. G. Colloidal Atomic Layer Deposition Growth of PbS/CdS Core/Shell Quantum Dots. *Chem. Commun.* **2017**, *53* (5), 869–872.

(36)   Balan, A. D.; Eshet, H.; Olshansky, J. H.; Lee, Y. V; Rabani, E.; Alivisatos, A. P. Effect of Thermal Fluctuations on the Radiative Rate in Core/Shell Quantum Dots. *Nano Lett.* **2017**, *17* (3), 1629–1636.

(37)   Park, Y.-S.; Bae, W. K.; Padilha, L. A.; Pietryga, J. M.; Klimov, V. I. Effect of the Core/Shell Interface on Auger Recombination Evaluated by Single-Quantum-Dot Spectroscopy. *Nano Lett.* **2014**, *14* (2), 396–402.

(38)   Huang, Z.; Xu, Z.; Mahboub, M.; Li, X.; Taylor, J. W.; Harman, W. H.; Lian, T.; Tang, M. L. PbS/CdS Core-Shell Quantum Dots Suppress Charge Transfer and Enhance Triplet Transfer. *Angew. Chemie Int. Ed.* **2017**, *56* (52), 16583–16587.

(39)   Ding, T. X.; Olshansky, J. H.; Leone, S. R.; Alivisatos, A. P. Efficiency of Hole Transfer from Photoexcited Quantum Dots to Covalently Linked Molecular Species. *J. Am. Chem. Soc.* **2015**, *137* (5), 2021–2029.

(40)   Kim, S.; Fisher, B.; Eisler, H.-J.; Bawendi, M. Type-II Quantum Dots: CdTe/CdSe(Core/Shell) and CdSe/ZnTe(Core/Shell) Heterostructures. *J. Am. Chem. Soc.*

2003, *125* (38), 11466–11467.

(41) Kamat, P. V. Quantum Dot Solar Cells. Semiconductor Nanocrystals as Light Harvesters. *J. Phys. Chem. C* **2008**, *112* (48), 18737–18753.

(42) Rühle, S.; Shalom, M.; Zaban, A. Quantum-Dot-Sensitized Solar Cells. *ChemPhysChem* **2010**, *11* (11), 2290–2304.

(43) Zhang, X.; Zhang, Y.; Wu, H.; Yan, L.; Wang, Z.; Zhao, J.; Yu, W. W.; Rogach, A. L. PbSe Quantum Dot Films with Enhanced Electron Mobility Employed in Hybrid Polymer/Nanocrystal Solar Cells. *RSC Adv.* **2016**, *6* (21), 17029–17035.

(44) Norman, Z. M.; Anderson, N. C.; Owen, J. S. Electrical Transport and Grain Growth in Solution-Cast, Chloride-Terminated Cadmium Selenide Nanocrystal Thin Films. *ACS Nano* **2014**, *8* (7), 7513–7521.

(45) Anderson, N. C.; Owen, J. S. Soluble, Chloride-Terminated CdSe Nanocrystals: Ligand Exchange Monitored by 1 H and 31 P NMR Spectroscopy. *Chem. Mater.* **2013**, *25* (1), 69–76.

(46) Comparelli, R.; Zezza, F.; Striccoli, M.; Curri, M. L.; Tommasi, R.; Agostiano, A. Improved Optical Properties of CdS Quantum Dots by Ligand Exchange. *Mater. Sci. Eng. C* **2003**, *23* (6–8), 1083–1086.

(47) Hassinen, A.; Gomes, R.; De Nolf, K.; Zhao, Q.; Vantomme, A.; Martins, J. C.; Hens, Z. Surface Chemistry of CdTe Quantum Dots Synthesized in Mixtures of Phosphonic Acids and Amines: Formation of a Mixed Ligand Shell. *J. Phys. Chem. C* **2013**, *117* (27), 13936–13943.

(48) Bullen, C.; Mulvaney, P. The Effects of Chemisorption on the Luminescence of CdSe Quantum Dots. *Langmuir* **2006**, *22* (7), 3007–3013.

(49) Kundu, B.; Chakrabarti, S.; Pal, A. J. Redox Levels of Dithiols in II–VI Quantum Dots Vis-à-Vis Photoluminescence Quenching: Insight from Scanning Tunneling Spectroscopy. *Chem. Mater.* **2014**, *26* (19), 5506–5513.

(50) Munro, A. M.; Jen-La Plante, I.; Ng, M. S.; Ginger, D. S. Quantitative Study of the Effects of Surface Ligand Concentration on CdSe Nanocrystal Photoluminescence. *J. Phys. Chem. C* **2007**, *111* (17), 6220–6227.

(51) Zhou, J.; Zhu, M.; Meng, R.; Qin, H.; Peng, X. Ideal CdSe/CdS Core/Shell Nanocrystals Enabled by Entropic Ligands and Their Core Size-, Shell Thickness-, and Ligand-Dependent Photoluminescence Properties. *J. Am. Chem. Soc.* **2017**, *139* (46), 16556–16567.

(52) Olshansky, J. H.; Ding, T. X.; Lee, Y. V; Leone, S. R.; Alivisatos, A. P. Hole Transfer from Photoexcited Quantum Dots: The Relationship between Driving Force and Rate. *J. Am. Chem. Soc.* **2015**, *137* (49), 15567–15575.

(53) Liu, I.-S.; Lo, H.-H.; Chien, C.-T.; Lin, Y.-Y.; Chen, C.-W.; Chen, Y.-F.; Su, W.-F.; Liou, S.-C. Enhancing Photoluminescence Quenching and Photoelectric Properties of CdSe Quantum Dots with Hole Accepting Ligands. *J. Mater. Chem.* **2008**, *18* (6), 675.

(54) Jin, S.; Harris, R. D.; Lau, B.; Aruda, K. O.; Amin, V. A.; Weiss, E. A. Enhanced Rate of Radiative Decay in CdSe Quantum Dots upon Adsorption of an Exciton-Delocalizing Ligand. *Nano Lett.* **2014**, *14* (9), 5323–5328.

(55) Anderson, N. C.; Hendricks, M. P.; Choi, J. J.; Owen, J. S. Ligand Exchange and the Stoichiometry of Metal Chalcogenide Nanocrystals: Spectroscopic Observation of Facile Metal-Carboxylate Displacement and Binding. *J. Am. Chem. Soc.* **2013**, *135* (49), 18536–18548.

(56) Owen, J. The Coordination Chemistry of Nanocrystal Surfaces. *Science (80-.).* **2015**, *347* (6222), 615–616.

(57) De Roo, J.; Justo, Y.; De Keukeleere, K.; Van den Broeck, F.; Martins, J. C.; Van Driessche, I.; Hens, Z. Carboxylic-Acid-Passivated Metal Oxide Nanocrystals: Ligand Exchange Characteristics of a New Binding Motif. *Angew. Chemie Int. Ed.* **2015**, n/a-n/a.

(58) De Roo, J.; De Keukeleere, K.; Hens, Z.; Van Driessche, I.; Garcia-Rodriguez, R.; Hendricks, M. P.; Cossairt, B. M.; Liu, H. T.; Owen, J. S.; Tessier, M. D.; et al. From Ligands to Binding Motifs and beyond; the Enhanced Versatility of Nanocrystal Surfaces. *Dalt. Trans.* **2016**, *45* (34), 13277–13283.

(59) Jasieniak, J.; Bullen, C.; Van Embden, J.; Mulvaney, P. Phosphine-Free Synthesis of CdSe Nanocrystals. *J. Phys. Chem. B* **2005**, *109* (44), 20665–20668.

(60) Wang, F.; Buhro, W. E. Morphology Control of Cadmium Selenide Nanocrystals: Insights into the Roles of Di- n -Octylphosphine Oxide (DOPO) and Di- n -Octylphosphinic Acid (DOPA). *J. Am. Chem. Soc.* **2012**, *134* (11), 5369–5380.

(61) Zhong, X.; Feng, Y.; Zhang, Y. Facile and Reproducible Synthesis of Red-Emitting CdSe Nanocrystals in Amine with Long-Term Fixation of Particle Size and Size Distribution. *J. Phys. Chem. C* **2007**, *111* (2), 526–531.

(62) Qu, L.; Peng, Z. A.; Peng, X. Alternative Routes toward High Quality CdSe Nanocrystals. *Nano Lett.* **2001**, *1* (6), 333–337.

(63) Anikeeva, P. O.; Halpert, J. E.; Bawendi, M. G.; Bulović, V. Quantum Dot Light-Emitting Devices with Electroluminescence Tunable over the Entire Visible Spectrum. *Nano Lett.* **2009**, *9* (7), 2532–2536.

(64) Caruge, J. M.; Halpert, J. E.; Wood, V.; Bulović, V.; Bawendi, M. G. Colloidal Quantum-Dot Light-Emitting Diodes with Metal-Oxide Charge Transport Layers. *Nat. Photonics* **2008**, *2* (4), 247–250.

(65) Medintz, I. L.; Uyeda, H. T.; Goldman, E. R.; Mattoussi, H. Quantum Dot Bioconjugates for Imaging, Labelling and Sensing. *Nat. Mater.* **2005**, *4* (6), 435–446.

(66) Dai, M.-Q.; Yung, L.-Y. L. Ethylenediamine-Assisted Ligand Exchange and Phase Transfer of Oleophilic Quantum Dots: Stripping of Original Ligands and Preservation of Photoluminescence. *Chem. Mater.* **2013**, *25* (11), 2193–2201.

(67) Nakane, Y.; Tsukasaki, Y.; Sakata, T.; Yasuda, H.; Jin, T. Aqueous Synthesis of Glutathione-Coated PbS Quantum Dots with Tunable Emission for Non-Invasive

Fluorescence Imaging in the Second near-Infrared Biological Window (1000–1400 Nm). *Chem. Commun.* **2013**, *49* (69), 7584.

(68) Green, M. The Nature of Quantum Dot Capping Ligands. *J. Mater. Chem.* **2010**, *20* (28), 5797.

(69) Tomczak, N.; Liu, R.; Vancso, J. G. Polymer-Coated Quantum Dots. *Nanoscale* **2013**, *5* (24), 12018.

(70) Hassinen, A.; Moreels, I.; De Nolf, K.; Smet, P. F.; Martins, J. C.; Hens, Z. Short-Chain Alcohols Strip X-Type Ligands and Quench the Luminescence of PbSe and CdSe Quantum Dots, Acetonitrile Does Not. *J. Am. Chem. Soc.* **2012**, *134* (51), 20705–20712.

(71) Chen, P. E.; Anderson, N. C.; Norman, Z. M.; Owen, J. S. Tight Binding of Carboxylate, Phosphonate, and Carbamate Anions to Stoichiometric CdSe Nanocrystals. *J. Am. Chem. Soc.* **2017**, *139* (8), 3227–3236.

(72) Roberge, A.; Stein, J. L.; Shen, Y.; Cossairt, B. M.; Greytak, A. B. Purification and In Situ Ligand Exchange of Metal-Carboxylate-Treated Fluorescent InP Quantum Dots via Gel Permeation Chromatography. *J. Phys. Chem. Lett.* **2017**, *8* (17), 4055–4060.

(73) Joo, S.-Y.; Park, H.-S.; Kim, D.; Kim, B.-S.; Lee, C. G.; Kim, W.-B. An Investigation into the Effective Surface Passivation of Quantum Dots by a Photo-Assisted Chemical Method. *AIP Adv.* **2018**, *8* (1), 015017.

(74) Webber, D. H.; Brutchey, R. L. Ligand Exchange on Colloidal CdSe Nanocrystals Using Thermally Labile Tert-Butylthiol for Improved Photocurrent in Nanocrystal Films. *J. Am. Chem. Soc.* **2012**, *134* (2), 1085–1092.

(75) Fritzinger, B.; Moreels, I.; Lommens, P.; Koole, R.; Hens, Z.; Martins, J. C. In Situ Observation of Rapid Ligand Exchange in Colloidal Nanocrystal Suspensions Using Transfer NOE Nuclear Magnetic Resonance Spectroscopy. *J. Am. Chem. Soc.* **2009**, *131* (8), 3024–3032.

(76) Grandhi, G. K.; M., A.; Viswanatha, R. Understanding the Role of Surface Capping Ligands in Passivating the Quantum Dots Using Copper Dopants as Internal Sensor. *J. Phys. Chem. C* **2016**, *120* (35), 19785–19795.

(77) Cass, L. C.; Malicki, M.; Weiss, E. A. The Chemical Environments of Oleate Species within Samples of Oleate-Coated PbS Quantum Dots. *Anal. Chem.* **2013**, *85* (14), 6974–6979.

(78) Zeininger, L.; Portilla, L.; Halik, M.; Hirsch, A. Quantitative Determination and Comparison of the Surface Binding of Phosphonic Acid, Carboxylic Acid, and Catechol Ligands on TiO2 Nanoparticles. *Chem. - A Eur. J.* **2016**, *22* (38), 13506–13512.

(79) Fritzinger, B.; Capek, R. K.; Lambert, K.; Martins, J. C. J. C.; Hens, Z. Utilizing Self-Exchange to Address the Binding of Carboxylic Acid Ligands to CdSe Quantum Dots. *J. Am. Chem. Soc.* **2010**, *132* (29), 10195–10201.

(80) Koole, R.; Schapotschnikow, P.; de Mello Donegá, C.; Vlugt, T. J. H.; Meijerink, A. Time-Dependent Photoluminescence Spectroscopy as a Tool to Measure the Ligand

Exchange Kinetics on a Quantum Dot Surface. *ACS Nano* **2008**, *2* (8), 1703–1714.

(81)   Kroupa, D. M.; Anderson, N. C.; Castaneda, C. V.; Nozik, A. J.; Beard, M. C. In Situ Spectroscopic Characterization of a Solution-Phase X-Type Ligand Exchange at Colloidal Lead Sulphide Quantum Dot Surfaces. *Chem. Commun.* **2016**, *52* (96), 13893–13896.

(82)   Sachleben, J. R.; Colvin, V.; Emsley, L.; Wooten, E. W.; Alivisatos, A. P. Solution-State NMR Studies of the Surface Structure and Dynamics of Semiconductor Nanocrystals. *J. Phys. Chem. B* **1998**, *102* (50), 10117–10128.

(83)   Hassinen, A.; Moreels, I.; de Mello Donegá, C.; Martins, J. C.; Hens, Z. Nuclear Magnetic Resonance Spectroscopy Demonstrating Dynamic Stabilization of CdSe Quantum Dots by Alkylamines. *J. Phys. Chem. Lett.* **2010**, *1* (17), 2577–2581.

(84)   Marbella, L. E.; Millstone, J. E. NMR Techniques for Noble Metal Nanoparticles. *Chem. Mater.* **2015**, *27* (8), 2721–2739.

(85)   Zeng, B.; Palui, G.; Zhang, C.; Zhan, N.; Wang, W.; Ji, X.; Chen, B.; Mattoussi, H. Characterization of the Ligand Capping of Hydrophobic CdSe–ZnS Quantum Dots Using NMR Spectroscopy. *Chem. Mater.* **2018**, *30* (1), 225–238.

(86)   Hens, Z.; Martins, J. C. A Solution NMR Toolbox for Characterizing the Surface Chemistry of Colloidal Nanocrystals. *Chem. Mater.* **2013**, *25* (8), 1211–1221.

(87)   Bovey, F. A. *Nuclear Magnetic Resonance Spectroscopy*, 2nd ed.; Academic Press, Inc.: San Diego, CA, 1988.

(88)   Lambert, J. B.; Mazzola, E. P. *Nuclear Magnetic Resonance Spectroscopy: An Introduction to Principles, Applications, and Experimental Methods*; Pearson Education, Inc.: Upper Saddle River, NJ, 2004.

(89)   Nelson, J. H. *Nuclear Magnetic Resonance Spectroscopy*; Pearson Education, Inc.: Upper Saddle River, NJ, 2003.

(90)   Bakhmutov, V. I. *Practical NMR Relaxation for Chemists*; John Wiley & Sons, Ltd: Chichester, UK, 2004.

(91)   Polenova, T.; Gupta, R.; Goldbourt, A. Magic Angle Spinning NMR Spectroscopy: A Versatile Technique for Structural and Dynamic Analysis of Solid-Phase Systems. *Anal. Chem.* **2015**, *87* (11), 5458–5469.

(92)   Traficante, D. D. Relaxation. Can T2 Be Longer than T1? *Concepts Magn. Reson.* **1991**, *3* (3), 171–177.

(93)   Gomes, R.; Hassinen, A.; Szczygiel, A.; Zhao, Q.; Vantomme, A.; Martins, J. C.; Hens, Z. Binding of Phosphonic Acids to CdSe Quantum Dots: A Solution NMR Study. *J. Phys. Chem. Lett.* **2011**, *2* (3), 145–152.

(94)   Jen, J. Chemical Exchange and NMR-T2 Relaxation. *Adv. Mol. Relax. Process.* **1974**, *6* (2), 171–183.

(95)   Bjelić, S.; Jelesarov, I. A Survey of the Year 2007 Literature on Applications of Isothermal Titration Calorimetry. *J. Mol. Recognit.* **2008**, *21* (5), 289–312.

(96) Kardos, J.; Yamamoto, K.; Hasegawa, K.; Naiki, H.; Goto, Y. Direct Measurement of the Thermodynamic Parameters of Amyloid Formation by Isothermal Titration Calorimetry. *J. Biol. Chem.* **2004**, *279* (53), 55308–55314.

(97) Freire, E.; Mayorga, O. L.; Straume, M. Isothermal Titration Calorimetry. *Anal. Chem.* **1990**, *62* (18), 950A–959A.

(98) Duff, M. R.; Grubbs, J.; Howell, E. E. Isothermal Titration Calorimetry for Measuring Macromolecule-Ligand Affinity. *J. Vis. Exp.* **2011**, No. 55, 5–8.

(99) Vander Meulen, K. A.; Butcher, S. E. Characterization of the Kinetic and Thermodynamic Landscape of RNA Folding Using a Novel Application of Isothermal Titration Calorimetry. *Nucleic Acids Res.* **2012**, *40* (5), 2140–2151.

(100) Dumas, P.; Ennifar, E.; Da Veiga, C.; Bec, G.; Palau, W.; Di Primo, C.; Piñeiro, A.; Sabin, J.; Muñoz, E.; Rial, J. Extending ITC to Kinetics with KinITC. *Methods Enzymol.* **2016**, *567*, 157–180.

(101) Di Trani, J. M.; Moitessier, N.; Mittermaier, A. K. Measuring Rapid Time-Scale Reaction Kinetics Using Isothermal Titration Calorimetry. *Anal. Chem.* **2017**, *89* (13), 7022–7030.

(102) Shen, Y.; Tan, R.; Gee, M. Y.; Greytak, A. B. Quantum Yield Regeneration: Influence of Neutral Ligand Binding on Photophysical Properties in Colloidal Core/Shell Quantum Dots. *ACS Nano* **2015**, *9* (3), 3345–3359.

(103) Gourishankar, A.; Shukla, S.; Ganesh, K. N.; Sastry, M. Isothermal Titration Calorimetry Studies on the Binding of DNA Bases and PNA Base Monomers to Gold Nanoparticles. *J. Am. Chem. Soc.* **2004**, *126* (41), 13186–13187.

(104) Lin, W.; Walter, J.; Burger, A.; Maid, H.; Hirsch, A.; Peukert, W.; Segets, D. A General Approach To Study the Thermodynamics of Ligand Adsorption to Colloidal Surfaces Demonstrated by Means of Catechols Binding to Zinc Oxide Quantum Dots. *Chem. Mater.* **2015**, *27* (1), 358–369.

(105) Yang, B.; Liu, R.; Hao, X.; Wu, Y.; Du, J. Effect of CdTe Quantum Dots Size on the Conformational Changes of Human Serum Albumin: Results of Spectroscopy and Isothermal Titration Calorimetry. *Biol. Trace Elem. Res.* **2013**, *155* (1), 150–158.

(106) Demarse, N. A.; Quinn, C. F.; Eggett, D. L.; Russell, D. J.; Hansen, L. D. Calibration of Nanowatt Isothermal Titration Calorimeters with Overflow Reaction Vessels. *Anal. Biochem.* **2011**, *417* (2), 247–255.

(107) Brown, A. Analysis of Cooperativity by Isothermal Titration Calorimetry. *Int. J. Mol. Sci.* **2009**, *10* (8), 3457–3477.

(108) Flamee, S.; Cirillo, M.; Abe, S.; De Nolf, K.; Gomes, R.; Aubert, T.; Hens, Z. Fast, High Yield, and High Solid Loading Synthesis of Metal Selenide Nanocrystals - Supporting Information. *Chem. Mater.* **2013**, *25* (12), 2476–2483.

(109) Susumu, K.; Oh, E.; Delehanty, J. B.; Blanco-Canosa, J. B.; Johnson, B. J.; Jain, V.; Hervey, W. J.; Algar, W. R.; Boeneman, K.; Dawson, P. E.; et al. Multifunctional Compact Zwitterionic Ligands for Preparing Robust Biocompatible Semiconductor

Quantum Dots and Gold Nanoparticles. *J. Am. Chem. Soc.* **2011**, *133* (24), 9480–9496.

(110) Park, Y.; Advincula, R. C. Hybrid Semiconductor Nanoparticles: π-Conjugated Ligands and Nanostructured Films. *Chem. Mater.* **2011**, *23* (19), 4273–4294.

(111) Chaikin, Y.; Bendikov, T. A.; Cohen, H.; Vaskevich, A.; Rubinstein, I. Phosphonate-Stabilized Silver Nanoparticles: One-Step Synthesis and Monolayer Assembly. *J. Mater. Chem. C* **2013**, *1* (22), 3573–3583.

(112) Sellers, D. G.; Button, A. A.; Nasca, J. N.; Wolfe, G. E.; Chauhan, S.; Watson, D. F. Excited-State Charge Transfer within Covalently Linked Quantum Dot Heterostructures. *J. Phys. Chem. C* **2015**, *119* (49), 27737–27748.

(113) Dubois, F.; Mahler, B.; Dubertret, B.; Doris, E.; Mioskowski, C. A Versatile Strategy for Quantum Dot Ligand Exchange. *J. Am. Chem. Soc.* **2007**, *129* (3), 482–483.

(114) Hassan, Y.; Janes, T.; Pensack, R. D.; Rafiq, S.; Brodersen, P. M.; Winnik, M. A.; Song, D.; Scholes, G. D. Direct Synthesis of CdSe Nanocrystals with Electroactive Ligands. *Chem. Mater.* **2016**, *28* (14), 4953–4961.

(115) Erdogan, A.; Karakaya, C.; Gonce, M. K.; Buyukcelebi, S.; Yenel, E.; Kara, K.; Ozcivan, A. N.; Can, M.; Kus, M.; Demic, S. Surface Modification of CdSeS Nanocrystals for Polymer Hybrid Solar Cells. *RSC Adv.* **2016**, *6* (33), 27627–27631.

(116) Knauf, R. R.; Lennox, J. C.; Dempsey, J. L. Quantifying Ligand Exchange Reactions at CdSe Nanocrystal Surfaces. *Chem. Mater.* **2016**, *28* (13), 4762–4770.

(117) Pearson, R. G. Hard and Soft Acids and Bases. *J. Am. Chem. Soc.* **1963**, *85* (22), 3533–3539.

(118) Parr, R. G.; Pearson, R. G. Absolute Hardness: Companion Parameter to Absolute Electronegativity. *J. Am. Chem. Soc.* **1983**, *105* (26), 7512–7516.

(119) Kanicky, J. R.; Shah, D. O. Effect of Degree, Type, and Position of Unsaturation on the PKa of Long-Chain Fatty Acids. *J. Colloid Interface Sci.* **2002**, *256* (1), 201–207.

(120) Ulman, A. Formation and Structure of Self-Assembled Monolayers. *Chem. Rev.* **1996**, *96* (4), 1533–1554.

(121) Jones, R. L.; Pearsall, N. C.; Batteas, J. D. Disorder in Alkylsilane Monolayers Assembled on Surfaces with Nanoscopic Curvature. *J. Phys. Chem. C* **2009**, *113* (11), 4507–4514.

(122) Feichtenschlager, B.; Lomoschitz, C. J.; Kickelbick, G. Tuning the Self-Assembled Monolayer Formation on Nanoparticle Surfaces with Different Curvatures: Investigations on Spherical Silica Particles and Plane-Crystal-Shaped Zirconia Particles. *J. Colloid Interface Sci.* **2011**, *360* (1), 15–25.

(123) Sato, K.; Yoshimoto, N.; Suzuki, M.; Kobayashi, M.; Kaneko, F. Structure and Transformation in Polymorphism of Petroselinic Acid (Cis-.Omega.-12-Octadecenoic Acid). *J. Phys. Chem.* **1990**, *94* (7), 3180–3185.

(124) Liu, H.; Owen, J. S.; Alivisatos, A. P. Mechanistic Study of Precursor Evolution in Colloidal Group II−VI Semiconductor Nanocrystal Synthesis. *J. Am. Chem. Soc.* **2007**,

129 (2), 305–312.

(125) Foo, K. Y.; Hameed, B. H. Insights into the Modeling of Adsorption Isotherm Systems. *Chem. Eng. J.* **2010**, *156* (1), 2–10.

(126) Masel, R. I. *Principles of Adsorption and Reaction on Solid Surfaces*; John Wiley & Sons, Inc.: New York, NY, 1996.

(127) Myers, D. *Surfaces, Interfaces, and Colloids: Principles and Applications*, 2nd ed.; John Wiley & Sons, Inc.: New York, NY, 1999.

(128) Morris-Cohen, A. J.; Vasilenko, V.; Amin, V. A.; Reuter, M. G.; Weiss, E. A. Model for Adsorption of Ligands to Colloidal Quantum Dots with Concentration-Dependent Surface Structure. *ACS Nano* **2012**, *6* (1), 557–565.

(129) MOREELS, I.; MARTINS, J.; HENS, Z. Solution NMR Techniques for Investigating Colloidal Nanocrystal Ligands: A Case Study on Trioctylphosphine Oxide at InP Quantum Dots. *Sensors Actuators B Chem.* **2007**, *126* (1), 283–288.

(130) Rempel, J. Y.; Trout, B. L.; Bawendi, M. G.; Jensen, K. F. Density Functional Theory Study of Ligand Binding on CdSe (0001), (000$\bar{1}$), and (11$\bar{2}$0) Single Crystal Relaxed and Reconstructed Surfaces: Implications for Nanocrystalline Growth. *J. Phys. Chem. B* **2006**, *110* (36), 18007–18016.

(131) Manna, L.; Wang, L. W.; Cingolani, R.; Alivisatos, A. P. First-Principles Modeling of Unpassivated and Surfactant-Passivated Bulk Facets of Wurtzite CdSe: A Model System for Studying the Anisotropic Growth of CdSe Nanocrystals. *J. Phys. Chem. B* **2005**, *109* (13), 6183–6192.

(132) Schapotschnikow, P.; Hommersom, B.; Vlugt, T. J. H. Adsorption and Binding of Ligands to CdSe Nanocrystals. *J. Phys. Chem. C* **2009**, *113* (29), 12690–12698.

(133) Margraf, J. T.; Ruland, A.; Sgobba, V.; Guldi, D. M.; Clark, T. Theoretical and Experimental Insights into the Surface Chemistry of Semiconductor Quantum Dots. *Langmuir* **2013**, *29* (49), 15450–15456.

(134) Puzder, A.; Williamson, A. J.; Zaitseva, N.; Galli, G.; Manna, L.; Alivisatos, A. P. The Effect of Organic Ligand Binding on the Growth of CdSe Nanoparticles Probed by Ab Initio Calculations. *Nano Lett.* **2004**, *4* (12), 2361–2365.

(135) Ghosh, S.; Gaspari, R.; Bertoni, G.; Spadaro, M. C.; Prato, M.; Turner, S.; Cavalli, A.; Manna, L.; Brescia, R. Pyramid-Shaped Wurtzite CdSe Nanocrystals with Inverted Polarity. *ACS Nano* **2015**, No. 8, 150723173715008.

(136) Peng, X.; Manna, L.; Yang, W.; Wickham, J.; Scher, E.; Kadavanich, A.; Alivisatos, A. Shape Control of CdSe Nanocrystals. *Nature* **2000**, *404* (6773), 59–61.

(137) Li, Z.; Peng, X. Size/Shape-Controlled Synthesis of Colloidal CdSe Quantum Disks: Ligand and Temperature Effects. *J. Am. Chem. Soc.* **2011**, *133* (17), 6578–6586.

(138) Rice, K. P.; Saunders, A. E.; Stoykovich, M. P. Seed-Mediated Growth of Shape-Controlled Wurtzite CdSe Nanocrystals: Platelets, Cubes, and Rods. *J. Am. Chem. Soc.*

2013, *135* (17), 6669–6676.

(139) Peng, X. Mechanisms for the Shape-Control and Shape-Evolution of Colloidal Semiconductor Nanocrystals. *Adv. Mater.* **2003**, *15* (5), 459–463.

(140) Kan, S.; Mokari, T.; Rothenberg, E.; Banin, U. Synthesis and Size-Dependent Properties of Zinc-Blende Semiconductor Quantum Rods. *Nat. Mater.* **2003**, *2* (3), 155–158.

(141) Liu, L.; Zhuang, Z.; Xie, T.; Wang, Y.; Li, J.; Peng, Q.; Li, Y. Shape Control of CdSe Nanocrystals with Zinc Blende Structure. *J. Am. Chem. Soc.* **2009**, *131* (45), 16423–16429.

(142) Polovitsyn, A.; Dang, Z.; Movilla, J. L.; Martín-García, B.; Khan, A. H.; Bertrand, G. H. V.; Brescia, R.; Moreels, I. Synthesis of Air-Stable CdSe/ZnS Core–Shell Nanoplatelets with Tunable Emission Wavelength. *Chem. Mater.* **2017**, *29* (13), 5671–5680.

(143) Jana, S.; Phan, T. N. T.; Bouet, C.; Tessier, M. D.; Davidson, P.; Dubertret, B.; Abécassis, B. Stacking and Colloidal Stability of CdSe Nanoplatelets. *Langmuir* **2015**, *31* (38), 10532–10539.

(144) Tessier, M. D.; Mahler, B.; Nadal, B.; Heuclin, H.; Pedetti, S.; Dubertret, B. Spectroscopy of Colloidal Semiconductor Core/Shell Nanoplatelets with High Quantum Yield. *Nano Lett.* **2013**, *13* (7), 3321–3328.

(145) Ithurria, S.; Tessier, M. D.; Mahler, B.; Lobo, R. P. S. M.; Dubertret, B.; Efros, A. L.; S M Lobo, R. P.; Dubertret, B.; Efros, A. L.; Lobo, R. P. S. M.; et al. Colloidal Nanoplatelets with Two-Dimensional Electronic Structure. *Nat. Mater.* **2011**, *10* (12), 936–941.

(146) Bouet, C.; Mahler, B.; Nadal, B.; Abecassis, B.; Tessier, M. D.; Ithurria, S.; Xu, X.; Dubertret, B. Two-Dimensional Growth of CdSe Nanocrystals, from Nanoplatelets to Nanosheets. *Chem. Mater.* **2013**, *25* (4), 639–645.

(147) Riedinger, A.; Ott, F. D.; Mule, A.; Mazzotti, S.; Knüsel, P. N.; Kress, S. J. P.; Prins, F.; Erwin, S. C.; Norris, D. J. An Intrinsic Growth Instability in Isotropic Materials Leads to Quasi-Two-Dimensional Nanoplatelets. *Nat. Mater.* **2017**.

(148) Ithurria, S.; Dubertret, B. Quasi 2D Colloidal CdSe Platelets with Thicknesses Controlled at the Atomic Level. *J. Am. Chem. Soc.* **2008**, *130* (49), 16504–16505.

(149) Yang, Y.; Qin, H.; Peng, X. Intramolecular Entropy and Size-Dependent Solution Properties of Nanocrystal–Ligands Complexes. *Nano Lett.* **2016**, *16* (4), 2127–2132.

(150) Yang, Y.; Qin, H.; Jiang, M.; Lin, L.; Fu, T.; Dai, X.; Zhang, Z.; Niu, Y.; Cao, H.; Jin, Y.; et al. Entropic Ligands for Nanocrystals: From Unexpected Solution Properties to Outstanding Processability. *Nano Lett.* **2016**, *16* (4), 2133–2138.

(151) Frederick, M. T.; Achtyl, J. L.; Knowles, K. E.; Weiss, E. A.; Geiger, F. M. Surface-Amplified Ligand Disorder in CdSe Quantum Dots Determined by Electron and Coherent Vibrational Spectroscopies. *J. Am. Chem. Soc.* **2011**, *133* (19), 7476–7481.

(152) Weeraman, C.; Yatawara, A. K.; Bordenyuk, A. N.; Benderskii, A. V. Effect of Nanoscale Geometry on Molecular Conformation: Vibrational Sum-Frequency Generation of

Alkanethiols on Gold Nanoparticles. *J. Am. Chem. Soc.* **2006**, *128* (44), 14244–14245.

(153) Dellwig, T.; Rupprechter, G.; Unterhalt, H.; Freund, H.-J. Bridging the Pressure and Materials Gaps: High Pressure Sum Frequency Generation Study on Supported Pd Nanoparticles. *Phys. Rev. Lett.* **2000**, *85* (4), 776–779.

(154) Aliaga, C.; Park, J. Y.; Yamada, Y.; Lee, H. S.; Tsung, C.-K.; Yang, P.; Somorjai, G. A. Sum Frequency Generation and Catalytic Reaction Studies of the Removal of Organic Capping Agents from Pt Nanoparticles by UV−Ozone Treatment. *J. Phys. Chem. C* **2009**, *113* (15), 6150–6155.

(155) Boyd, R. W. *Nonlinear Optics*, 3rd ed.; Academic Press, Inc.: Orlando, FL, 2008.

(156) Lambert, A. G.; Davies, P. B.; Neivandt, D. J. Implementing the Theory of Sum Frequency Generation Vibrational Spectroscopy: A Tutorial Review. *Appl. Spectrosc. Rev.* **2005**, *40* (2), 103–145.

(157) Bain, C. D. Sum-Frequency Vibrational Spectroscopy of the Solid/Liquid Interface. *J. Chem. Soc. Faraday Trans.* **1995**, *91* (9), 1281–1296.

(158) Lu, Z.; Karakoti, A.; Velarde, L.; Wang, W.; Yang, P.; Thevuthasan, S.; Wang, H. Dissociative Binding of Carboxylic Acid Ligand on Nanoceria Surface in Aqueous Solution: A Joint In Situ Spectroscopic Characterization and First-Principles Study. *J. Phys. Chem. C* **2013**, *117* (46), 24329–24338.

(159) Čapek, R. K.; Moreels, I.; Lambert, K.; De Muynck, D.; Zhao, Q.; Van Tomme, A.; Vanhaecke, F.; Hens, Z. Optical Properties of Zincblende Cadmium Selenide Quantum Dots. *J. Phys. Chem. C* **2010**, *114* (14), 6371–6376.

Appendices

A-1 CdSe Syntheses

Flamee et. al. – Oleate-capped adaptation

CdO (8 mmol) and oleic acid (24 mmol) were added to ODE (10 mL) in a 50 mL three-neck flask with a condenser and degassed while stirring under vacuum for an hour at 100 °C. The CdO mixture was then heated to 270 °C to form a clear cadmium oleate complex *in situ*. Selenium powder (4 mmol) was mixed with 2 mL ODE under inert atmosphere and the heterogeneous slurry was kept stirring. The selenium slurry was injected into the cadmium oleate solution and the reaction set temperature was decreased to 260 °C. The nanocrystals were grown for 5 minutes and the flask was cooled quickly with a stream of acetone and nitrogen, resulting in a nanocrystal solution with a red color and orange luminescence. 10 mL of toluene was added to the flask and the resulting solution was transferred to centrifuge tubes. Acetone/methyl acetate were added until the solution became turbid and the particles were spun down at 9000 rcf to form a pellet, followed by re-dispersion in toluene. This purification procedure was repeated twice more and the resulting solution was stored in toluene under inert atmosphere.

Size selective precipitation of purified particles was accomplished by addition of methyl acetate and acetone to the quantum dot solution dropwise until the very first signs of flocculation were observed, notably a transient opacity and light color near the droplet addition that disappears with solution mixing and a slight increase in solution cloudiness/light scattering. The solution was then spun at 5000 rcf and the pellet dispersed in toluene. This procedure was repeated 4 additional times. Optical characterization of both the initial supernatant and final pellet reveals the removal of the small nanocrystals from the stock solution.

Knauf et. al. – Adapted for mild anti-solvent purification

CdO (2.33 mmol) was added to a 50 mL three neck flask with a condenser along with 2 mL oleic acid and 20 mL ODE. This mixture was degassed at room temperature while stirring for 1 hour, then heated to 280 °C under argon to form a clear Cd-oleate complex *in situ*. The cadmium precursor solution was then cooled to 120 °C. The flow of argon was increased and one neck of the flask was opened to allow the addition of selenium powder (1.27 mmol) directly to the flask. After the neck of the flask was sealed, the mixture was heated to 240 °C and allowed to grow for 2 minutes at this temperature. The reaction was promptly removed from the heating mantle and cooled by the addition of 40 mL toluene (added quickly but in a controlled manner to prevent bumping). The resulting solution was divided between 4 50 mL centrifuge tubes and 5 mL acetone were added for every 7.5 mL reaction solution (about 10 mL per centrifuge tube, the solution should remain colloidally stable). The solutions were allowed to rest for 5-10 minutes, then spun at 8000 rcf for 5 minutes. The resulting supernatant was then distributed between 6 50 mL centrifuge tubes and acetone was added up to 35 mL solution. The turbid solution was spun at 8000 rcf for 5 minutes and the pellet was re-dissolved in toluene. This procedure was repeated twice more, although only between 5-10 mL acetone was necessary for subsequent purification

steps as the solution was more concentrated. If the solution becomes gelatinous, 1 mL oleic acid may be added to break up any polymers formed by excess Cd-oleate precursor that has yet to be removed and 1 additional repeat of the cleaning procedure may be added. The resulting nanocrystal solution was stored in toluene under inert atmosphere.

Liu et. al. – Adapted tetrahedral synthesis

Selenium powder (1 mmol) and 15 mL ODE were stirred in a 50 mL three neck flask with a condenser. This mixture was degassed under vacuum at room temperature for 1 hour, then heated under argon flow to 280 °C to dissolve the Se and this temperature was maintained for 30 minutes. While the selenium solution was heating, $Cd(Ac)_2 \cdot 2H_2O$ (1.16 mmol) and 5 mL oleic acid were degassed under vacuum for 15 minutes at room temperature. The cadmium mixture was then heated to 120 °C to form a clear complex and immediately injected into the selenium solution. The nanocrystal growth temperature was then set to 260 °C and the reaction was continued for 40 minutes. The reaction was promptly cooled and purified by the addition of isopropanol to obtain a turbid solution and subsequent centrifugation at 8000 rpm. The pellet was re-dispersed in toluene and the purification was repeated twice more. The final result was stored in toluene under inert atmosphere.

Ithurria et. al. – 553 nm emission nanoplatelets, adapted to add oleate ligands post-synthetically

$Cd(myristate)_2$ (0.3 mmol) was added to 15 mL ODE in a three neck flask with a condenser and degassed at 100 °C for 1 hour with stirring. This mixture was then heated to 240 °C under argon to melt/dissolve the cadmium complex. A heterogeneous slurry of selenium powder in ODE (0.15 M) was made under inert atmosphere and kept stirring to maintain dispersion. Once the cadmium precursor reached temperature, 1 mL of the selenium dispersion was quickly injected (using a 16G needle). The argon flow was immediately increased and one neck of the flask was opened. 10 seconds after the Se injection, $Cd(acetate)_2 \cdot 2H_2O$ (0.3 mmol) that had been ground to a powder was added. Care must be taken to add this powder quickly or it will melt and stick to the spatula and neck of flask, leading to irreproducible plates of varying thickness. One solution to this problem was a 2-spatula approach: 1 spatula holding the compound and 1 spatula to scrape the compound into the reaction. The nanocrystals were allowed to grow for 10 minutes at 240 °C, and then the reaction was removed from heat and cooled quickly using a spray of acetone and nitrogen gas. Once the flask temperature had cooled to 75 °C, 0.5 mL oleic acid was injected to the solution and the product was allowed to cool to room temperature.

The nanocrystal solution was divided between 2 50 mL centrifuge tubes and an initial purification step was taken to separate the nanoplatelets from the quantum dots that form as a side product of the synthesis. To this end hexanes were added up to a total solution volume of 15 mL in each tube followed by 5 mL ethanol and the solutions were spun at 5000 rpm for 10 minutes. The resulting supernatant contained near exclusively quantum dots and was discarded. The nanoplatelet pellet was then re-suspended in hexanes and ethanol was added until the solution became turbid.

Centrifugation was performed with the same conditions as above. The resulting pellet was suspended in hexanes and in order to prevent excessive nanoplatelet stacking and loss of colloidal stability, 1 mL dilute Cd-oleate solution was added to this suspension, with an approximate stoichiometric concentration determined by an estimate of nanoplatelet size and concentration. This purification procedure was then repeated 4 more times.

A-2 Synthesis of stoichiometric Cadmium Oleate/Myristate

Adapted from Riedinger et. al.[147]

$Cd(NO_3)_2 \cdot 4H_2O$ (15 mmol) and [oleic/myristic] acid (30 mmol) were dissolved in 650 mL methanol in a 1 L flask. NaOH (45 mmol) was likewise dissolved in 50 mL methanol and this solution was added to the cadmium solution dropwise over the course of 2 hours with brisk stirring. The Cd-[oleate/myristate] complex precipitated as a fluffy white solid and this product was vacuum filtered and rinsed 3 times with methanol. The product was then covered and dried over the vacuum overnight before storage at -20 °C.

A-3 NMR parameters

Deuterated THF was stored in an inert atmosphere and used as the ligand exchange solvent. Measurements were done using a Bruker 700 MHz magnet with a cryo-probe at a set temperature of 298 K. The 90° pulse calibration was checked for each sample and after each reaction step. For quantitative H^1 NMR, a 30° pulse was used and 64 scans were averaged using a D1 delay time of 32 seconds.

A-4 Ligand Exchange concentrations

Quantum dot stock solution concentrations were determined using the size-dependent extinction coefficient formulae developed by Capek et. al.[159]

$$E_g = 1.74 + \frac{1}{0.89 - 0.36d + 0.22d^2}$$

$$\varepsilon_{340nm} = 19300d^3$$

where d is the effective nanocrystal diameter. Quantum dot solutions for ligand exchange reactions were optimized to enable NMR and ITC characterization of equivalent reactions. 9 µM nanocrystal solutions showed bound ligand concentrations of 1.3 mM. All ligand solutions were made in 10 mM concentrations. A 50% concentration decrease in both titrant and analyte solutions shows minimal effects on the enthalpy of ligand exchange as observed by isothermal titration calorimetry.

A-5 Modified isotherm derivation

The standard Langmuir isotherm is designed to model the adsorption of a single species to a bare substrate, and it can be modified to include competitive adsorption. These isotherms have physical meaning and may be directly derived from the definitions of surface coverage and the reaction equilibrium constant.

Single species adsorption: $\theta = \dfrac{K_{eq}C}{1+K_{eq}C}$

Competitive adsorption: $\theta = \dfrac{K_{eq}C}{1+K_{eq}C}$

Ligand exchange reactions, however, involve a new species displacing molecules already chemisorbed or bound to the surface. It is possible to show that this exchange is isomorphic to the adsorption case. Both ligand species will have surface and solution contributions and the total surface sites can be defined by the sum of both bound species.

$$K_{eq} = \frac{[QD-B][A]}{[QD-A][B]} \qquad \theta = \frac{[QD-B]}{[QD-A]+[QD-B]}$$

$$\frac{[QD-B]}{[QD-A]+[QD-B]} = \frac{\frac{[QD-B][A]}{[QD-A][B]}*C}{\left(1+\frac{[QD-B][A]}{[QD-A][B]}*C\right)}$$

$$\frac{[QD-A]+[QD-B]}{[QD-B]} = \frac{\left(1+\frac{[QD-B][A]}{[QD-A][B]}*C\right)}{\frac{[QD-B][A]}{[QD-A][B]}*C}$$

$$\frac{[QD-A]}{[QD-B]}+1 = \frac{1}{\frac{[QD-B][A]}{[QD-A][B]}*C}+1$$

$$\frac{[QD-A]}{[QD-B]}*C = \frac{[QD-A][B]}{[QD-B][A]}$$

$$C = \frac{[B]}{[A]}$$

The concentration factor derived from this isomorphism can then be incorporated into the ligand exchange expressions for other models based on the Langmuir isotherm.

A-6 Mean Field Theory

In the development of a model to adequately reproduce ordering and packing effects on a nanocrystal surface, it is necessary to define the effects as a sum of contributions from individual exchange events. To this end we define a model quantum dot surface over which to average. A reasonable surface to represent our standard CdSe quantum dot is a 10x10 square lattice with periodic boundary conditions where each lattice site represents a ligand binding site (Figure 10.1). All binding sites are assumed to have a ligand bound at all times and inter-ligand interactions are defined on the basis of horizontal and vertical nearest neighbors on the lattice. In order to avoid double-counting inter-ligand interactions, each ligand is defined to have an interaction with the ligand below it and the one directly to its right in the lattice, and it can be shown that the total number of inter-ligand interactions on the surface is equal to twice the number of ligands bound. The total energy of the simulated surface at any given time is defined by the binding energies of all bound ligands, ε_A and ε_B (which may vary depending on the binding group of the chosen ligand), as well as the sum of inter-ligand interactions. These inter-ligand interactions, which we propose to be determined by both head and tail group properties, are captured by individually defined coupling terms J_{AA}, J_{AB}, and J_{BB} for A-A, A-B, and B-B nearest neighbors, respectively. This instantaneous system energy can be represented mathematically as follows:

$$E = \sum_i [-\varepsilon_B n_i - \varepsilon_A (1 - n_i)]$$
$$+ \sum_{ij} [-J_{BB} n_i n_j - J_{AA} (1 - n_i)(1 - n_j) - J_{AB}(1 - n_i)n_j - J_{AB} n_i (1 - n_j)]$$

The occupancy of a given site i is defined as n_i, with ligand A assigned a value of $n = 0$ and ligand B assigned a value of $n = 1$. This relation may be simplified to find two inter-related parameters that tune the model energy as a function of the surface occupancy and number of nearest neighbors (Z).

$$E = -\Delta\varepsilon \sum_i n_i - \Delta J \sum_{ij} n_i n_j$$

$$\Delta\varepsilon = \varepsilon_B - \varepsilon_A - ZJ_{AA} + ZJ_{AB}$$

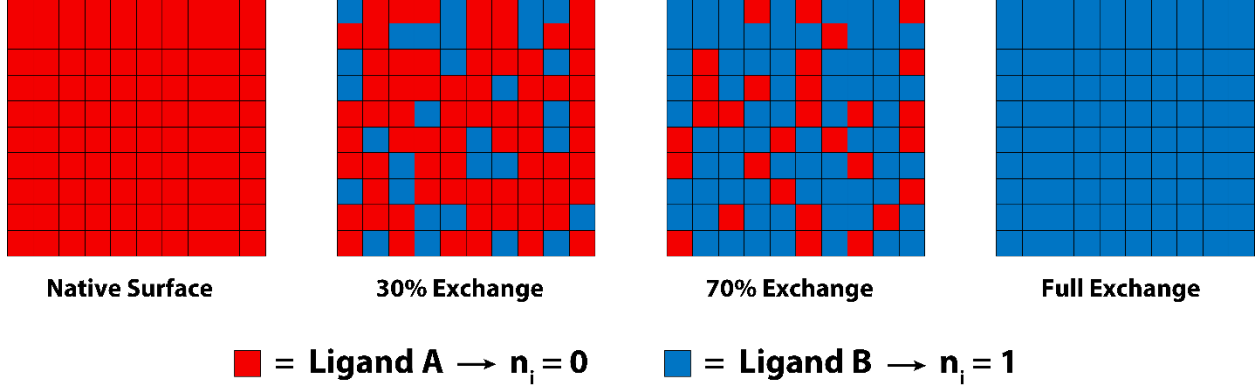$$\Delta J = J_{AA} + J_{BB} - 2J_{AB}$$

Figure A.1: Modeling the nanocrystal surface as a lattice gas. A quantum dot surface approximated as a 10x10 square lattice with periodic boundary conditions and seen at different points during an exchange reaction.

Having defined the parameters contributing to the energetic state of the surface, we can simulate a ligand exchange using a Metropolis Monte Carlo algorithm to determine whether attempted exchange events are successful.

$$P_{exch} \; \alpha \; \begin{cases} 1, & \Delta E_{exch} \leq 0 \\ exp(-\beta \Delta E_{exch}), & \Delta E_{exch} \geq 0 \end{cases}$$

The exchange attempts may be weighted by the availability of free ligand A and ligand B in the system, or more explicitly, chemical potentials for each ligand (μ_A and μ_B) can be accounted for in the simulation.

$$\Delta E_{exch} \xrightarrow{becomes} \Delta E_{exch} - \Delta \mu * \Delta \left(\sum_i n_i \right)$$

$$\text{where} \quad \Delta \mu = \mu_B - \mu_A$$

This simple model, however, neglects the assumption that each ligand exchange must by necessity change the overall surface structure of the nanocrystal ligand shell given such a small system. Accounting only for direct nearest neighbor interactions in exchange probability and equilibration of the model surface, an exchange is much more energetically favorable adjacent to ligands which form favorable inter-ligand interactions. This leads to ligand island formation and does not accurately represent the physical effects of exchange in the system (Figure 10.2).

Mean field theory offers the capability of making a simple approximation to account for collective ordering effects during simulated ligand exchange reactions. Using this model, we assume that the equilibrium state of the system at a given chemical potential of ligand can be approximated by starting with a reference system whose state is a function of an overall potential optimized for a self-consistent field. The partition function of the system of interest can be defined in terms of the reference partition function.

$$\Xi = \sum_{n_i} e^{\beta \Delta \mu \sum_i n_i - \beta E} \geq \Xi_{ref} e^{\langle \beta [(\Delta \mu - \bar{\mu}) \sum_i n_i - E] \rangle_{ref}}$$
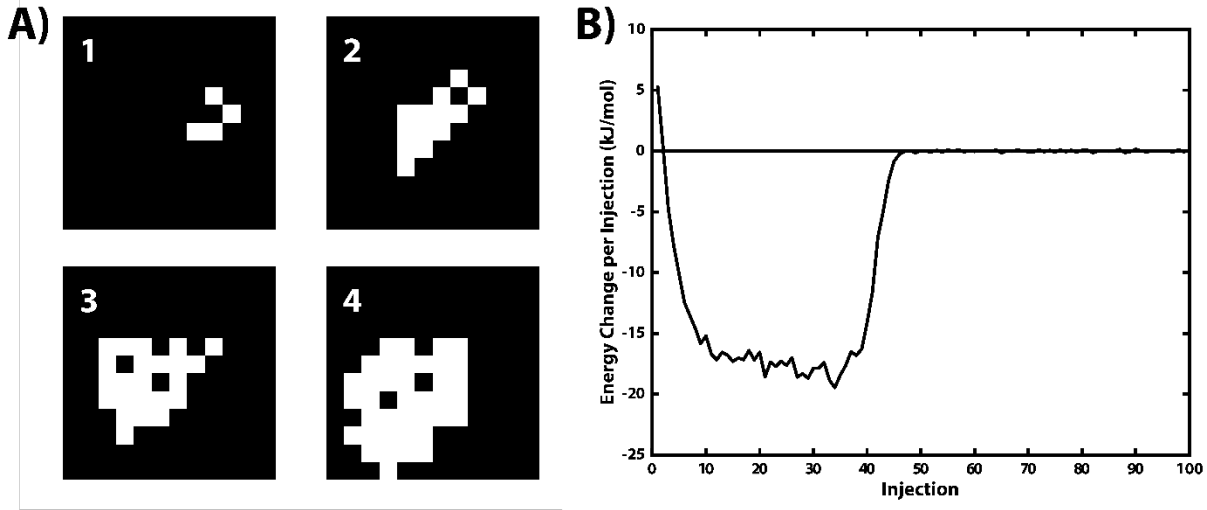
Figure A.2: Nearest neighbors modeling without collective effects. A) Snapshots of ligand island formation in an exchange model that does not use a mean field approximation and B) the change in the energy of the surface as these exchange events occur. Selective exchange near an exchanged island leads to near immediate maximization of exchange energy and the resulting plateau in the modeled energy per injection.

Maximizing the value of the approximate partition function gives a relation for the optimized potential.

$$\bar{\mu} = \Delta\mu + \Delta\varepsilon + \Delta J Z \bar{n}$$

The equilibrium surface coverage $\bar{n}$ is defined as the expectation value of a site's occupancy in the reference system, and is subject to a self-consistent condition.

$$\bar{n} = \frac{e^{\beta\bar{\mu}}}{1 + e^{\beta\bar{\mu}}} = \frac{e^{\beta(\Delta\mu + \Delta\varepsilon + \Delta J Z \bar{n})}}{1 + e^{\beta(\Delta\mu + \Delta\varepsilon + \Delta J Z \bar{n})}}$$

This definition leads to the equilibrium equality:

$$\Delta\mu + \Delta\varepsilon = -\frac{\Delta J Z}{2}$$

The energy per site of the surface in the mean field approximation is therefore

$$\frac{E_{MF}}{N} = -\Delta\varepsilon\bar{n} - \frac{\Delta J Z \bar{n}^2}{2}$$

Now that we have determined the mean field equilibrium energy of the nanocrystal surface, we must determine how that energy and surface coverage varies as a function of free ligand chemical potential. To do this we use our previously defined effective chemical potential for the system ($\Delta\mu$), which for the sake of clarity will be referred to as μ_{eff} from here on. The effective chemical potential is used to define an effective free ligand density which we can vary over the course of a reaction:

59

$$\rho_{eff} V_{system} = e^{\beta\left(\mu_{eff} - \mu_{eff}^0\right)}$$

and from this it can be shown that

$$\frac{\delta}{\delta\rho_{eff}} = \frac{1}{\beta\rho_{eff}} * \frac{\delta}{\delta\mu_{eff}}$$

Thus the derivative of the average energy per surface site with respect to ρ_{eff} is found to be

$$\frac{\delta}{\delta\rho_{eff}}\left(\frac{E_{MF}}{N}\right) = \frac{1}{\beta\rho_{eff}} * \frac{\delta\bar{n}}{\delta\mu_{eff}}(-\Delta\varepsilon - \Delta JZ\bar{n})$$

$$= -(\Delta\varepsilon + \Delta JZ\bar{n})\frac{1}{\rho_{eff}} * \frac{\bar{n}(1-\bar{n})}{1 - \beta\Delta JZ\bar{n}(1-\bar{n})}$$

The iterative Monte Carlo model can then be set up with

$$\rho_{eff} = c * e^{\beta\mu_{eff}}$$

$$\text{where } c = \frac{1}{V_{system} * e^{\beta\mu_{eff}^0}}$$

and both $\frac{\delta}{\delta\rho_{eff}}\left(\frac{E_{MF}}{N}\right)$ and $\bar{n}$ can be determined as a function of ρ_{eff}.

A-7 Numerical ITC fitting

Fitting of thermodynamic reaction data acquired *via* isothermal titration calorimetry is at its core an equivalent analysis method to the standard adsorption isotherm fit to surface coverage. Unlike quantitative NMR characterization, there is no direct measurement of substrate or ligand concentrations and both must be adjusted for dilution after each injection. As the effective cell volume in the calorimeter is limited, and the enthalpy of any reaction occurring in the overflow chamber will not be sensed, the total enthalpy of reaction measured comes from a total amount of substrate that decreases slightly with each injection. Once these concentration values have been determined a number of adsorption models can be reformulated for titration calorimetry analysis.

We will consider three main categories of model, which depend on the following variables:

θ = fraction of surface sites bound by ligand B
K_{eq} = equilibrium constant of reaction
n = number of binding sites per quantum dot
$[QD]_{tot}$ = total quantum dot concentration in sample cell
$[QD - A]$ = concentration of native quantum dots in sample cell
$[QD - B_x]$ = concentration of quantum dots with x number of bound B ligands
$[B]_{tot}$ = total concentration of ligand B in sample cell (bound and free)

60

$[B]_{soln}$ = concentration of free ligand B in sample cell

V_0 = effective volume of the sample cell

dV_i = volume of injection i

For the simplest Langmuir adsorption model, the form of the isotherm and the relationship between bound, free, and total ligand can be used to solve for a hypothetical surface coverage θ as a function of equilibrium constant and mole ratio of added ligand to binding sites.

$$K_{eq} = \frac{\theta}{(1-\theta)[B]_{soln}}$$

$$[B]_{tot} = [B]_{soln} + n\theta[QD]_{tot}$$

$$\theta = \frac{1}{2}\left[1 + \frac{[B]_{tot}}{n[QD]_{tot}} + \frac{1}{nK_{eq}[QD]_{tot}} - \sqrt{\left(1 + \frac{[B]_{tot}}{n[QD]_{tot}} + \frac{1}{nK_{eq}[QD]_{tot}}\right)^2 - \frac{4[B]_{tot}}{n[QD]_{tot}}} \right]$$

When we adjust the isotherm to allow for exchange, we find that the surface coverage takes on a significantly different functional form.

$$K_{eq} = \frac{\theta[A]_{soln}}{(1-\theta)[B]_{soln}}$$

$$[A]_{soln} = n\theta[QD]_{tot}$$

$$\theta = \frac{1}{2(1-K_{eq})n[QD]_{tot}}\left[-K_{eq}(n[QD]_{tot} + [B]_{tot}) \right.$$
$$\left. + \sqrt{[-K_{eq}(n[QD]_{tot} + [B]_{tot})]^2 - 4n[QD]_{tot}(1-K_{eq}) - K_{eq}[B]_{tot}} \right]$$

Both of the above models assume negligible inter-ligand interactions, but a sequential binding model can be optimized to account for such interactions and cooperative binding. A full sequential model assigns n equilibrium constants and n enthalpies of exchange as each subsequent exchange on the same particle will be modulated by the surface coverage already present. For nanocrystal surface reactions this model can be easily over-parametrized as the number of binding sites per particle is larger than the number of data points to fit. It is possible therefore to impose constraints on sequential equilibria by defining a functional form for surface interactions and a bisection method may be used to solve for the many theoretical contributions to the surface coverage.

The heat content of the solution at any given time is defined as

$$Q = n\theta[QD]_{tot}\Delta H V_0$$

with slight modifications needed to account for the complexities of a sequential model. The data to fit, however, are in the form of $\Delta Q(i)$, given as follows:

$$\Delta Q(i) = Q(i) + \frac{dV_i}{V_0}\left[\frac{Q(i) + Q(i-1)}{2}\right] - Q(i-1)$$

Fit optimization is then performed as a function of n, K_{eq}, and ΔH, and θ may be calculated once again from optimized parameters for comparison with NMR surface coverage measurements.

A-8 SFG Sample preparation

Ligand exchange reactions were performed according to previous procedures, using previous surface coverage measurements to determine the appropriate stoichiometry to achieve desired surface coverages. Samples with 0, 50, and 100% phosphonic acid exchange were targeted. Quantum dot solutions in hexane were made at a concentration of 200 nM and deposited in sub-monolayer films on quartz substrates. Spin-coating was performed at 2000 rpm with 50 μL of particle solution. Films were characterized by transmission electron microscopy and an average of 514 particles per square micron density was observed (Figure 10.3). Particle distribution was consistent across the full area of the substrate. Spin coating was determined to be the optimal film formation technique as Langmuir-Blodgett films created full monolayers of particles with small inter-particle distance, potentially influencing inter-particle ligand interactions and contributing to a higher degree of film absorption and photoluminescence in the wavelength range of interest for SFG.
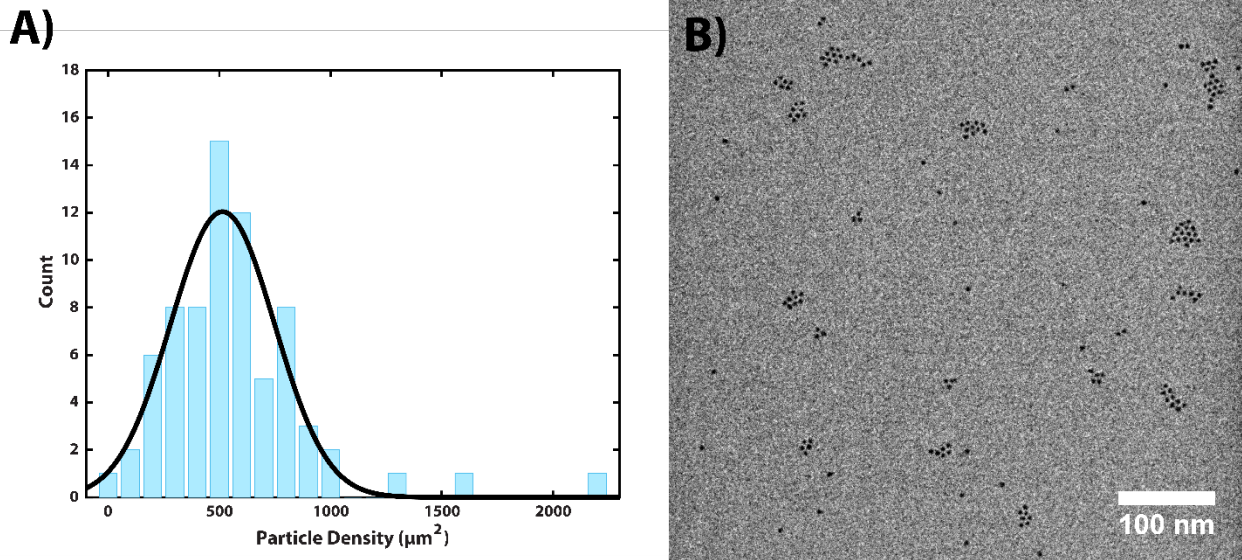

Figure A.3: SFG dilute film characterization. A) Distribution of particle densities after spin-coating, and B) representative TEM image of CdSe film

A-9 Analogous metal-ligand complex interactions

We observed that ligand exchanges with phosphonic acids also showed chain-length dependent exothermic signal with a single cadmium ion as the coordination center, and that the enthalpy of reaction for non-branched alkylphosphonic acids could be divided into two distinct stages (Figure 10.4). Stage 1 enthalpy is most affected by chain lengths of 8 carbon units or less, and may be related to changes in electron delocalization and binding energy of head groups modulated by the tail group. The chain length effects in the second half of the reaction are more pronounced for tail lengths of 8 carbon units or more. This may imply formation of Cd-phosphonate micelles or coordination polymers known to be stable at moderate to high concentrations in organic solvents of low to moderate polarity. It is of further note that in molecular cadmium complexes, carboxylate to phosphonate ligand exchange proceeds with 2:1 stoichiometry, as phosphonic acid undergoes two deprotonation events without the steric binding constraints of a packed surface monolayer. These reactions therefore reach completion when the phosphonic acid/oleate mole ratio is just over 0.5.
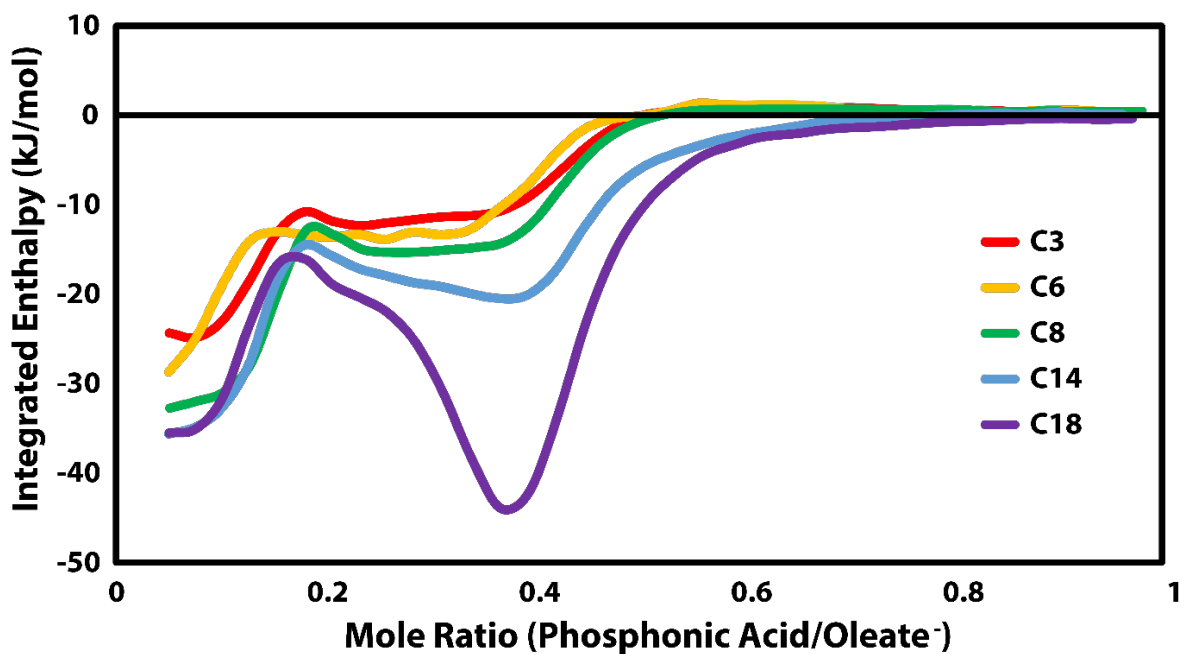

Figure A.4: Phosphonic acid ligand exchanges with cadmium complexes. Representative calorimetry titrations with tail groups ranging from 3-18 carbon units in length.

The observed collective effects in the metal-ligand complex exchanges place limits on our ability to estimate the change in head group binding enthalpy in these cases, but they do provide a characteristic signature for de-convoluting metal complex and quantum dot exchanges in equilibrium solutions containing free complexes. As both exchanges are strongly driven, we can make a first order approximation that each exchange will proceed equivalently in proportion to the concentration of each kind of binding site in solution. Assuming no preferential exchange for one site over another, the reaction of cadmium complexes still goes to completion at 50% of the concentration needed for quantum dot exchange, as each binding event displaces two carboxylate

ligands (Figure 10.5A). This affects the observed enthalpy during early ligand injections and shifts the overall amount of phosphonic acid needed to fully exchange the quantum dot ligand shell to higher mole ratios of ligand/nanocrystal binding sites (Figure 10.5B). Subtraction of concentration-scaled Cd-complex reaction enthalpy recovers the expected trend in reaction enthalpy.
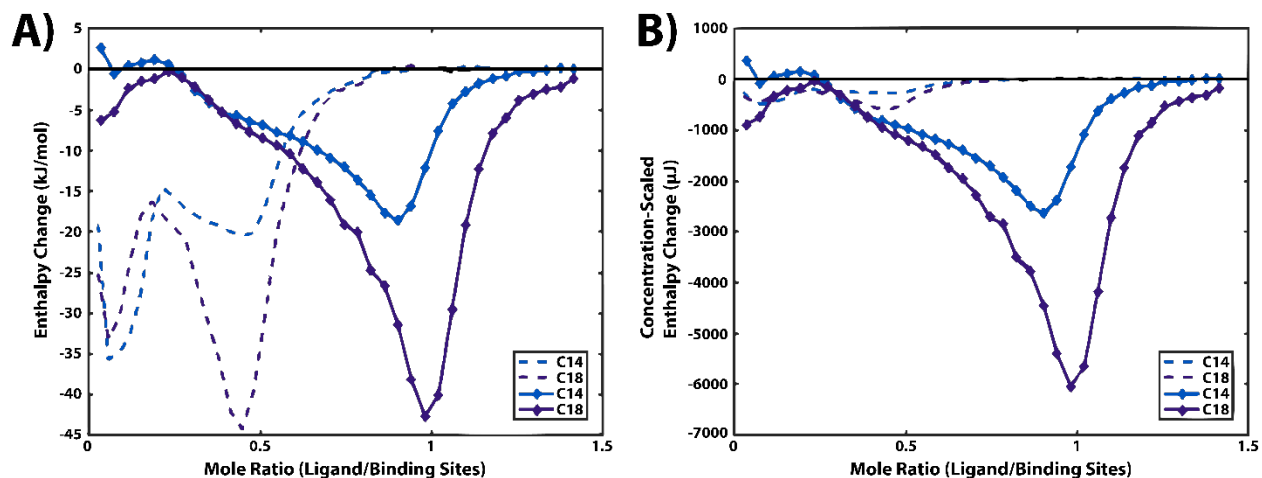

Figure A.5: Comparison of ligand exchange with Cd complexes and CdSe quantum dots. A) Molar enthalpy of reaction of ligand exchange with both analytes. Collective effects of a similar scale are observed for both substrates in the latter half of the reaction for long chain alkylphosphonates. B) Overall enthalpy of reaction for both substrates weighted by concentration in dilute equilibrium exchange solutions.